Measuring seismic station timing errors from ambient noise

by
Karina Løviknes

Master of Science Thesis in
Geoscience

Department of Earth Science
University of Bergen

May 2018

Abstract

Cross correlations of ambient seismic noise recorded at two stations can be used to estimate the Green's function between these two stations. Since seismic stations are continuously recoding seismic noise, the Green's function can be used to monitor the stability of a network of stations. The Green's function is the impulse response of the structure, and changes occurring in the structure will therefore affect the shape of the Green's function. However, variations in the Green's function can also be caused by changes in noise distribution and instrumental errors. In this thesis, techniques, similar to those used for monitoring velocity changes in the structure, are applied on ambient seismic noise to find instrumental timing errors. There are several steps between seismic noise and the Green's function, and the processing procedure is therefore divided into four main parts: preparing the data, preprocessing, cross correlation and stacking, and measuring the timing errors. A detailed description of the different parts is given and the limitations of the method are examined. The method is applied to noise recorded on stations from the temporary Norwegian network NEONOR2, that was located in northern Norway.

Acknowledgements

This thesis was written at the Department of Earth Science at the University of Bergen. First of all, I would like to thank my supervisor Professor Lars Ottemöller, for all the help and guidance with this thesis. I would also like to thank Henk Keers and my co-supervisor Stéphane Rondenay for suggestions and advice, and PhD candidate Alexandra Gassner, at Helmholtz Centre Potsdam for sharing her experience with cross correlating ambient seismic noise.

Finally I could like to thank my fellow students for making these last five years so fun, and my family and Andreas for your love and support.

Contents

Chapter 1

Introduction

The impulse response, the Green's function, can be estimated from cross correlating ambient seismic noise and further used to deduce the Earth structure. This was first suggested by Aki (1957) who proposed that microseismic noise could be used to find the dispersive properties of the subsurface. The theory was primarily applied in helioseismology (Duvall et al., 1993) and ultrasonic (Lobkis et al., 2001), before Shapiro and Campillo (2004) successfully reconstructed the Green's function from cross correlated seismic noise. Noise correlation studies have since been used to find the velocity structure of the Earth and monitor velocity changes in the subsoil.

Accurate timing is crucial for all methods using seismic data to find information about the Earth. However, inaccuracies caused by instrumental errors are not always simple to detect. In this thesis I will therefore investigate using the estimated Green's function to detect instrumental timing errors in seismic data. The objective is to develop an automatic process of measuring time errors using the Green's function and examine the limitations of the method.

In contrast to shifts caused by a change in velocity structure or noise distribution, instrumental timing errors will usually not affect negative and positive time lag of the noise correlation in the same way, but rather shift the entire noise correlation asymmetrically. This means that changes in the Green's function caused by instrumental errors can be distinguished from natural changes. Instrumental timing errors are usually caused by problems with the GPS receiver or digitizer, which can result in clock drift or sudden jumps in the data. When caused by disconnection from the GPS receiver or digitizer, the origin time of the error can be found in logs, if exists, and be corrected by resynchronising. However, logs do not always exist and immediate resynchronising with the GPS is not always possible during deployment, for example remote stations or Ocean Bottom Sensors. An automatic process would therefore be beneficial.

I calculate the Green's function from ambient seismic noise following the pre-processing steps of Bensen et al. (2007) and measure time delays in the recorded data following Sens-Schönfelder (2008). The method is then applied to seismic noise recorded on seismic stations from the NEONOR2 temporary network (Michálek et al., 2018).

Before describing the method, I give a brief background on the theory behind estimating the Green's function from ambient seismic noise and the different applications. In addition, I introduce the data set, the NEONOR2 network, used. I describe the method in four main parts separating the different steps going from raw data to the estimated Green's function and measured time delays. In the result chapter I show that the cross correlations are estimated Green's functions and that some of the stations have timing errors. I also show the effect different processing variables have on the results and finally discuss the uncertainties and limitations of the method.

Chapter 2

Background

2.1 The Green's function from a diffuse wavefield

In seismology the Green's function is defined as the Impulse response of a structure Stein and Wysession (2003). Traditionally the Green's function is found from ballistic sources like explosions and earthquakes. However, an estimate of the Greens' function can also be obtained from cross correlating diffuse wavefields.

2.1.1 Diffuse wavefields, equipartion

Since a diffuse wavefield is a superposition of plane waves of all direction and phases, it contains information about all the possible paths of the wavefield. When cross correlating diffuse wavefields recorded at two receivers, the common path between them, the Green's function, can thus be estimated (Shapiro and Campillo, 2004). The estimated Greens function describes the direct wave propagation between these receivers, as if one of the receivers were the source and the other the receiver.(Snieder, 2004).

There are several different theoretical approaches to explain how the Green's function can be estimated from a diffuse field. Lobkis et al. (2001) was one of the first to demonstrate, both theoretically and through experiments, that the Green's function can be estimated from cross correlating diffuse fields. The following simple proof is based on the principle of equipartition, assuming a closed and absorption free medium.

Equipartition is defined as equal distribution of energy in a system with various degrees of freedom (Oxford English Dictionary, 2018). A diffuse field ϕ at frequency ω, satisfies the principle of equipartition as it is composed of waves with random

amplitudes and phases (Weaver and Lobkis, 2004):

$$\phi(x,t) = \sum_n a_n u_n(x) \exp(i\omega t) \tag{2.1}$$

where x is position, t is time, a_n are complex modal amplitudes and u_n are normal modes. Modal amplitudes of diffuse fields are uncorrelated random variables:

$$\langle a_n, a_n \rangle = 0 \quad \langle a_n, a_m \rangle = 0 \quad \langle a_n, a_n * \rangle = \delta_{nm} F(\omega) \tag{2.2}$$

where $F(\omega)$ is the spectral energy density. Following the properties of equation 2.2, averaging of modal amplitudes will make cross terms disappear. Cross correlation of two diffuse wavefields $\phi(x,t)$ and $\phi(y,t)$ at location x and y, will therefore become:

$$C(x,y,L) = \int_{-\inf}^{+\inf} \phi(y,t)\phi(y,t+L)dt = \sum_n F(\omega) u_n(x) u_n(y) \exp(-i\omega_n L) \tag{2.3}$$

Where L is the lag time shift and u_n are normal modes. Equation 2.3 differs from the time derivative of the Green's function only by the amplitude factor $F(\omega)$:

$$G_{xy}(\tau) = \sum u_n(x) u_n(y) \frac{\sin(\omega_n \tau)}{\omega_n} \tag{2.4}$$

Further proof applicable to open systems with heterogeneities or scatterings is given by Snieder (2004), Weaver and Lobkis (2004) and Wapenaar (2004). In addition, other theoretical approaches explaining the link between the Green's function and the cross-correlation function, are given. Among these are Roux et al. (2005b) for a homogeneous medium with attenuation, and Sánchez-Sesma and Campillo (2006) considering the Canonical Elastic Problem.

It is commonly agreed that equipartition is a necessary condition for extracting the exact Green's function, however an estimate of the Green's function can still be obtained when scattering makes up for the source distribution and averaging makes up for the equipartition. This is illustrated in fig.2.1 where the cross correlation is calculated from averaging several circularly distributed sources.

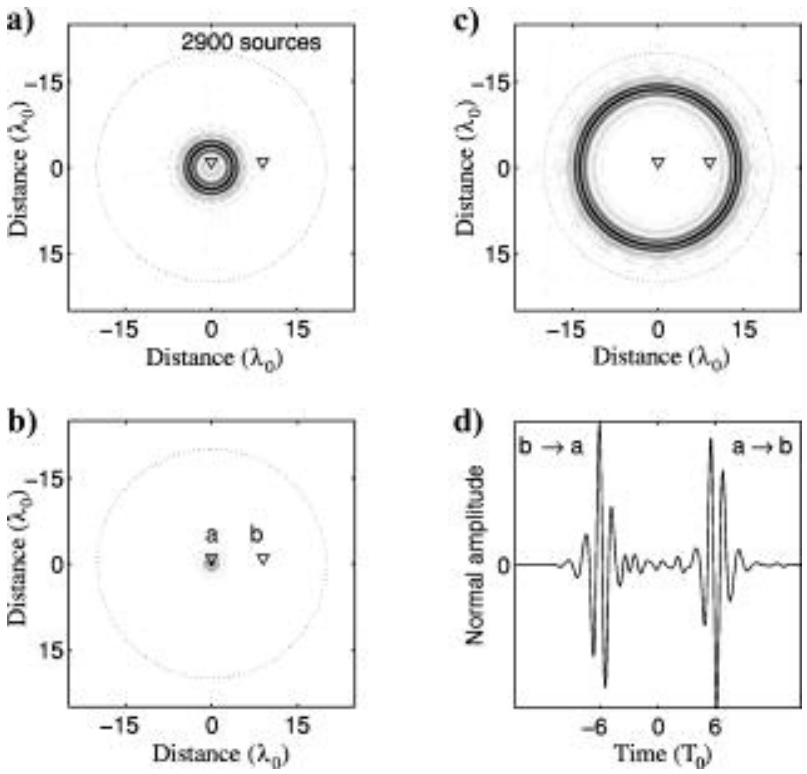

Figure 2.1: Map of the correlations averaged over 2900 circularly distributed sources. In (a), (b), and (c), the unit length is the wavelength $\lambda 0$. Maps are presented for (a) correlation times $\tau = -3T0$, (b), $\tau = 0$, and (c) $\tau = +10T0$, where $T0$ is the central period of oscillation. Figure 1(d) shows a typical correlation function for two points separated by six wavelengths. Negative τ corresponds to the wavefront propagating from b to a. (Larose et al., 2006)

2.1.2 Diffuse wavefields, Time reversal

A physical interpretation of a diffuse field, is given by Derode et al. (2003a), Derode et al. (2003b) and Larose et al. (2004) based on time-reversal symmetry. Considering two receivers A and B and a source S, see figure 2.2. With $\epsilon(t)$ as the excitation function in S, the wave fields ϕ_A and ϕ_B received in A and B, is expressed as:

$$\phi_A = \epsilon(t) * h_{AS} \qquad \phi_B = \epsilon(t) * h_{BS}, \tag{2.5}$$

where $h_{AS}(t)$ is the wave field received in A when a Dirac $\delta(t)$ is sent by S, and so on. The cross correlation C_{AB} of the field received in A and B then becomes:

$$C_{AB}(t) = \int \phi_A(\theta)\phi(t+\theta)d\theta = h_{AS} * h_{BS} * f(t) \tag{2.6}$$

where $f(t) = \epsilon(t) * \epsilon(-t)$. For a solid medium the propagation between the source and receivers is reciprocal, meaning that $h_{AC}(t) = h_{CA}(-t)$, see figure 2.3.

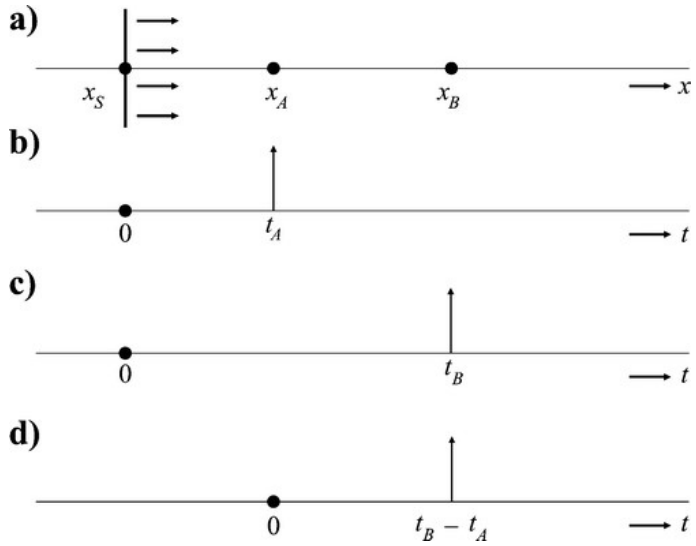

Figure 2.2: (a) A source S emits a plane wave travelling in positive x direction. (b) The response received in A. (c) The response received in B. Cross correlation of the responses at A and B, this is the same as if the source were emitted from A and received in B. (Wapenaar et al., 2010)

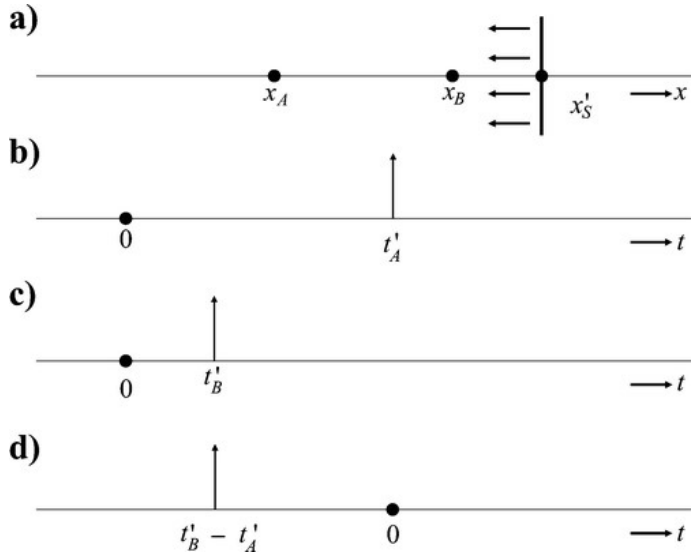

Figure 2.3: Same as figure 1.2, but with the emitted wave travelling in opposite direction. The cross correlation in (d) is the time reversed Green's function (Wapenaar et al., 2010)

The direct Green's function between the receivers h_{AB} can be found when using

several sources surrounding A and B. If these sources form a so-called "time reversal device" where the sources are continuously distributed around the receivers, there would be no loss of information. A pulse sent from A would therefore propagate everywhere, be scattered multiple times and recorded at every point in the time-reversal device, including B where $h_{AB}(t)$ is received, without any information loss. After the time-reversal, the field goes backwards in time and the field received in A then becomes $h_{AB}(-t)$, which is the time reversed version of the direct Green's function. Here $t > 0$ represents the causal part of the cross correlation and $t < 0$ represents the acausal part.

In reality a perfectly even distribution of sources is not possible, neither is an infinity long time series. However, Derode et al. (2003b) argues that when using a high number of sources, or scatterers, working as sources, and summing the correlations over the source position, source averaging, a good estimate of the Green's function can still be found:

$$\sum_C h_{AC}(t) * h_{CB}(t) = h_{AB}(t) + h_{AB}(-t) \tag{2.7}$$

This has been tested both numerically (Derode et al., 2003b) and experimentally (Derode et al., 2003a; Larose et al., 2004), and is in good agreement with the mathematical approach mentioned above.

2.2 Ambient seismic noise

Seismic noise comes from a high variety of sources. High frequency noise mainly comes from human activities, while low frequency noise like ambient seismic noise, mainly comes from oceanic microseisms and atmospheric disturbances (Gutenberg (1958), Friedrich et al. (1998)). The exact origin of ambient seismic noise is still discussed, and several studies have used noise correlations to investigate the sources.

At periods shorter than 20 s there are two significant peaks, named the primary (10-20 s) and secondary (5-10) microseisms. Stehly et al. (2006) used different seismic networks located around the world to determine the source of these peaks. The primary peak varies with seasons and is likely to be caused by infragravity waves, that is, long period ocean waves causing pressure to the sea bottom. This is also the main source for long-period noise above 20 s, "the hum" (Rhie and Romanowicz, 2004). The secondary microseisms, on the other hand, are more stable through the year and are thought to be caused by standing waves resulting from the reflection of waves at the coast (Landés et al., 2010; Kedar et al., 2008; Longuet-Higgins, 1950). A smaller, but interesting, peak at 26 s is also observed on noise records from

Northern American, European and African stations, Shapiro et al. (2006) located the origin of this peak to the Gulf of Guinea.

Although ambient seismic noise is not random and can be both directional and seasonal, scattering of seismic waves from heterogeneities within the earth and averaging over time makes the ambient seismic noise approximately diffuse and it is therefore possible to reconstruct the Greens function using ambient seismic noise. This was first proved by Shapiro and Campillo (2004) when the Green's function was estimated from ambient seismic noise recorded on stations in California. It has also been shown theoretically by Roux et al. (2005b).

Since the sources of ambient seismic noise are mostly shallow, surface waves are especially emergent in the noise correlations. However, because of the scatterers, body waves are also expected to exist in the noise correlations (Roux et al., 2005a).

2.3 Applications

Since surface waves and body waves can be found in cross correlations of ambient seismic noise, methods traditionally used by earthquake studies, can be used on noise correlation. Among these are studies on tomography and temporal changes in velocity. The Greens function estimated from noise correlations can also be used to detect timing errors in seismological equipment, which is the main objective of this thesis.

2.3.1 Tomography

Surface wave tomography

Surface wave tomography uses the dispersive properties of surface waves to image the velocity structure of the crust and lithosphere (Stein and Wysession, 2003). Surface waves propagate within the crust and upper mantle with velocities that depend on both frequency and depth. Surface waves dispersion is therefore a good indicator of the structure of the Earth.

Traditional tomographic studies use inversion to find travel times from seismic waves emitted by earthquakes and recorded at seismic stations. The tomographic path configuration therefore depends on the location and geometry of the event and station. This means that tomography studies are limited to seismic active areas and, because of attenuation, high quality dispersion measurements are difficult to obtain at periods below 15 s (Yang et al., 2007). Ambient seismic noise, on the other hand, is widely distributed. Tomographic imaging using ambient seismic noise thus has the advantage of higher resolution when recorded on dense seismic arrays, and possible imaging at short periods.

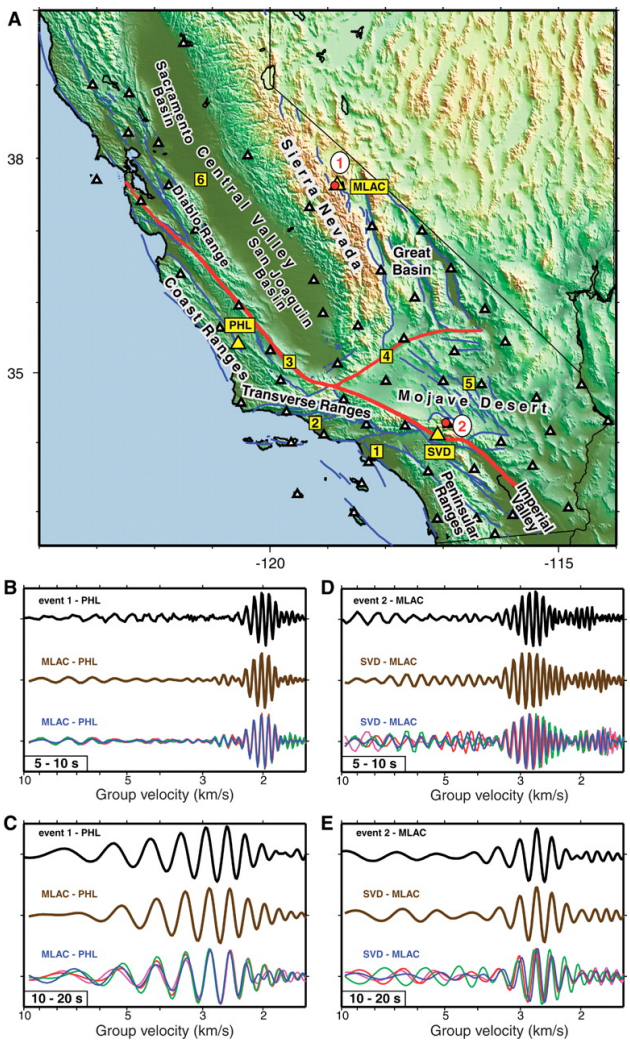

Figure 2.4: Waveforms found from cross-correlations of ambient seismic noise and compared with Rayleigh waves from earthquakes. (A) Map of California showing the locations of the stations(triangles) used in the study. (B) Comparison of waves propagating between stations MLAC and PHL (yellow triangles in (A)), bandpass filtered at periods 5-10 s. The upper trace (black) is the signal caused by earthquake 1 near MLAC observed at PHL, and normalized to the spectrum of the cross-correlated ambient noise; the middle trace (gold) is the cross-correlation from one year of ambient seismic noise recorded at stations MLAC and PHL; and the lower traces are cross-correlations from 4 separate months of noise observed at the two stations in 2004 (magenta, January; red, April; green, July; blue, October). (C) same as (B), except bandpassed at periods 10-20 s. (D) same as (B), but between stations SVD and MLAC, where earthquake 2 occurred near SVD, observed at MLAC. (E) same as (D), except bandpassed at periods 10-20 s. (Shapiro et al., 2005)

The first tomography maps extracted from cross correlating ambient seismic noise

were made by Shapiro et al. (2005) (figure 2.4)and Sabra et al. (2005b) using station pairs in California. The group velocity maps obtained showed strong correlations with the known geology of the area.

Similar studies have since been conducted all over the world, both on regional and local scale. Among these are Yang et al. (2007) and Verbeke et al. (2012) for Europe, Kang and Shin (2006) for Korea, Moschetti et al. (2007) for Northen America, Yao et al. (2008) for Tibet and Zheng et al. (2008) for China. Surface wave tomography based on noise correlations has also been done for Norway by Köhler et al. (2011) as a part of the MAGNUS project (Weidle et al., 2010; Maupin et al., 2013)).

Rayleigh waves are most easily extracted from the Green's function, and most studies therefore estimates Rayleigh group and phase velocities. However, some studies also include maps of Love wave velocity.

Most studies compute the noise correlations between station pairs, but when dealing with large dense network it is also possible to use interpolation to create high resolution velocity maps. In this case, each station is treated as a virtual source. One example is Ritzwoller et al. (2011) where the eikonal equation was used (Figure 2.5).

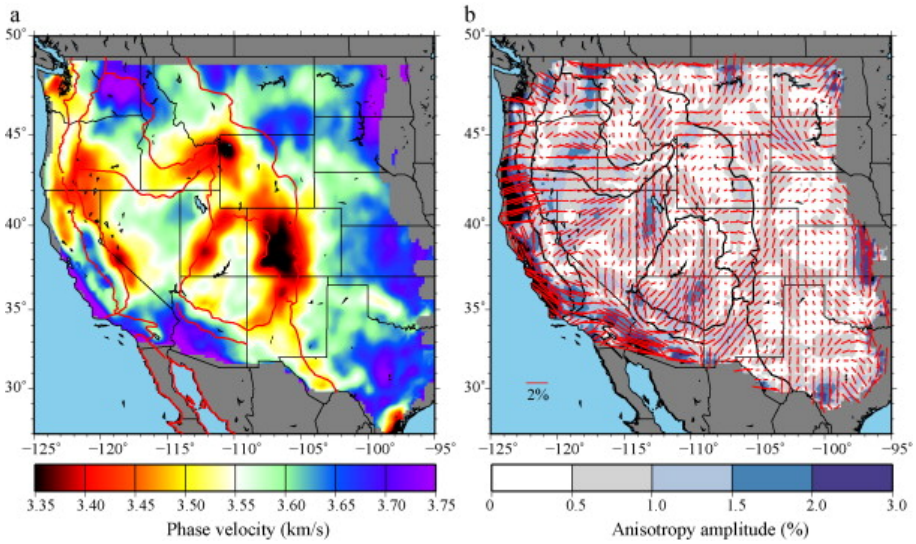

Figure 2.5: (a) Isotropic phase speed map of the 24 s Rayleigh wave. The map is calculated from ambient seismic noise by averaging all local phase speed measurements at each point on the map; (b) Amplitudes and fast directions of the 2ψ component of the 24 s Rayleigh wave phase velocities. (Ritzwoller et al., 2011)

Body wave tomography

Body wave tomography is used to image the deep structures of the Earth. Although surface waves dominate the cross correlations of ambient seismic noise, body waves are also present in the estimated Green's function. This was first proven by Roux et al. (2005a) using a small dense network in California. The velocity of the P-wave arrivals found in the noise correlations, were comparable to P-wave velocities found using ballistic sources. Several other body wave phases have since been identified in noise correlations. Among these are reflections from the Moho (Tibuleac and von Seggern, 2012; Zhan et al., 2010; Poli et al., 2012b), the transition zone (Poli et al., 2012a) and the core (Lin et al., 2013; Nishida, 2013; Boué et al., 2013).

Body wave arrivals found in noise correlations have also been used to map the origins of microseismic noise (Gerstoft et al., 2008; Landés et al., 2010)).

2.3.2 Velocity changes

Cross correlations of ambient seismic noise can also be used to detect velocity changes in the subsurface. Changes in the velocity structure can be monitored by repeating the cross correlation operation of noise recorded by two stations on different dates. Velocity changes can also be measured directly from the coda waves present in the late part of the noise correlations.

Several observations of velocity changes have been made. Wegler and Sens-Schönfelder (2007) and Wegler et al. (2009) observed a drop in seismic velocity after the 2004 M_w6.6 Mid-Niigata earthquake in Japan. Similar observations have since been made by Brenguier et al. (2008a) for earthquakes in California, by Froment et al. (2013) and Chen et al. (2010) for an earthquake in China and by Rivet et al. (2011) for an event in Mexico.

Seasonal velocity variations have been observed by Sens-Schönfelder and Wegler (2006), among others, where noise correlations were used to monitor temporal changes in the velocity structure of the Merapi volcano in Indonesia, and by Meier et al. (2010) for the Los Angeles basin. Velocity changes prior to landslides (Mainsant et al., 2012) and volcanic eruptions (Brenguier et al., 2008b) have also been observed (see figure 2.6).

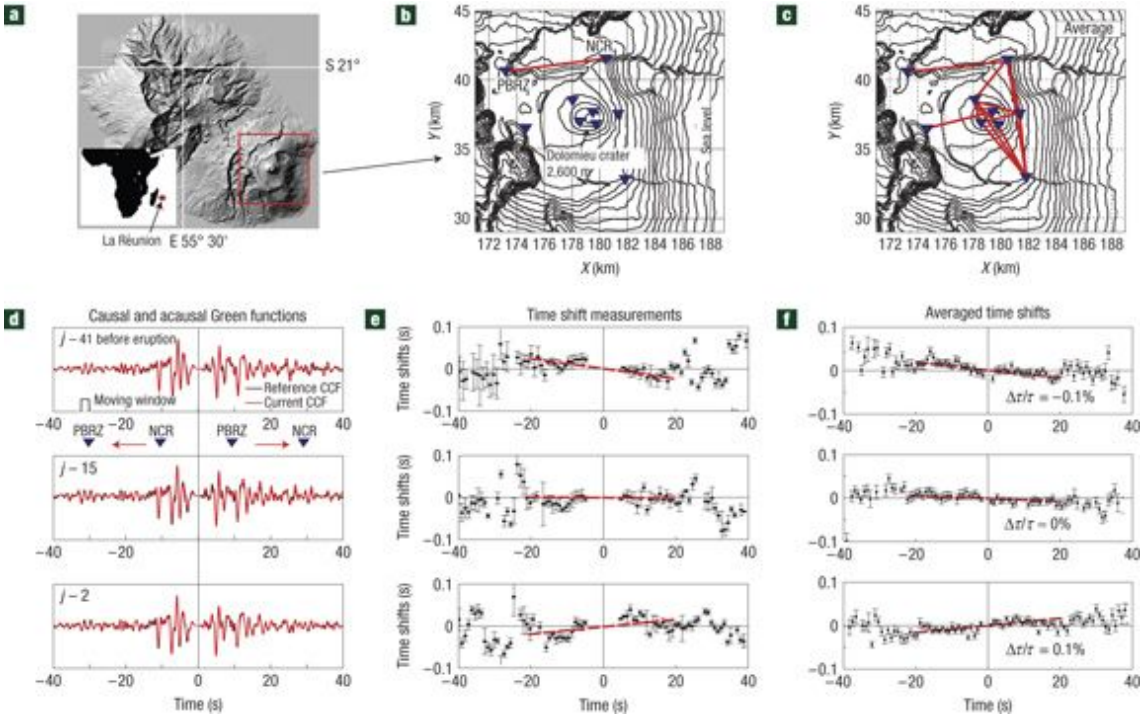

Figure 2.6: Time shifts measured prior to a volcanic eruption. (a) The Piton de la Fournaise volcano on La Réunion. (b), Topography map with seismic receivers. (c) Topography map with the direct path between all the seismic receivers. (d) Cross correlations from the receiver pair linked in (b), filtered between 0.1-0.9 Hz. The reference traces are shown in black, and the current traces in red. (e) Time shifts and time shift errors measured between the reference and current traces shown in (d). (f) Averaged time shifts measured using all the receiver pairs in (c). (Brenguier et al., 2008b)

Velocity monitoring using cross correlations of ambient seismic noise, depends on stable measurements and evenly distributed noise sources. Hadziioannou et al. (2009) have shown that the Green's function does not have to be perfectly reconstructed to observe velocity changes in the medium, as long as the background noise structure is stable. Hadziioannou et al. (2011) further argues that although a change in the directivity of the noise field would alter the estimated Green's function, this type of fluctuation can be identified and corrected for, and therefore does not need to directly affect the velocity change measurement.

2.3.3 Instrumental errors

The estimation of the Green's function from cross correlations of ambient seismic noise are dependent on stable measurements. Instrumental errors can therefore cause trouble. Stehly et al. (2007) have shown that the principle of time symmetry can be used to identify instrumental errors in noise correlations. While a physical change

in the medium would alter the travel time measured in both positive and negative cross-correlation time, and a change in spatial distribution of noise sources should affect the different time lags independently, a timing error caused by the clock in one of the stations would result in a time shift on the entire cross correlation. The different time shifts can therefore be identified when comparing noise correlations from different dates. The time delay is then measured from the arrival times of surface waves in the noise correlations. This has successively been done by Stehly et al. (2007), Sens-Schönfelder (2008) and Gouédard et al. (2014).

2.3.4 Exploration

Cross correlating seismic noise is also an emerging field in seismic exploration and is often called passive seismic interferometry. Wapenaar et al. (2010) define seismic interferometry as the process of generating new seismic responses from virtual sources by cross correlating seismic observations at different receiver locations. Controlled source interferometry, where active sources are used, is also included in the definition.

Noise correlations in exploration can both be used to find surface-wave or body-wave responses, for studies on tomography or temporal changes as described above, and to image the subsurface using reflection responses.

Bussat and Kugler (2011) showed that ambient noise surface-wave tomography can be done offshore at reservoir scale and suggested several industrial application areas for ambient seismic noise studies, including monitoring and anisotropy estimations. Similar studies have been conducted using dense ocean bottom seismogram networks in the North Sea (Mordret et al., 2013).

Larose et al. (2006) demonstrated that small details can be imaged from noise correlation, by mapping scatterers using distant sources in a laboratory experiment. Draganov et al. (2007) created seismic gathers from noise correlations which showed some of the same events found in an active seismic survey of the same area. Similar results were found by Draganov et al. (2009) when cross correlating 1 hour of data recorded along 8 lines in the Sirte basin in Libya, see figure 2.7

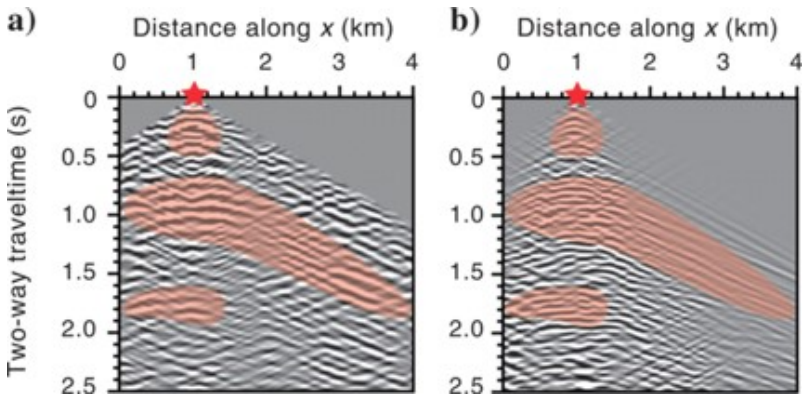

Figure 2.7: (a) Common-shot gather from the noise correlations. (b) Common-shot gather from an active source survey at the same location. The red stars indicate the positions of the virtual and real sources. The similar events are coloured in transparent red. Events prior to the direct-wave arrival are muted. (Draganov et al., 2009)

2.4 The data set

The NEONOR2 project was located in the Nordland region (figure 2.8), which is one of the most seismically active parts in Norway. The objective of the project was to use the seismic observations from the temporary network to create a geodynamic model of the area. In addition, information from InSAR images, geodetic monitoring and in situ stress measurements were used. The seismic observations are described in a report by Michálek et al. (2018).

The NEONOR2 temporary network consisted of 27 stations. The stations were mostly installed between August 2013 and March 2014 and were deployed until May 2016. The instrumentation used were either Nanometrics digitizers (Taurus) with Trillium 120PA sensors, or Earth Data digitizers (EDR-210) with STS 2.5 or CMG-3ESP sensors. The stations recorded continuously with 100 Hz sampling frequency on three channels (ZNE). An overview of stations with installation date, location and instrument type can be found in figure 2.9 and 2.10.

Data recorded by the NEONOR2 stations are available both at UiB and NORSAR, but are also stored at the GFZ (Geo Forschungs Zentrum) seismological data repository in Potsdam as part of a larger ScanArray deployment (Thybo et al., 2012).

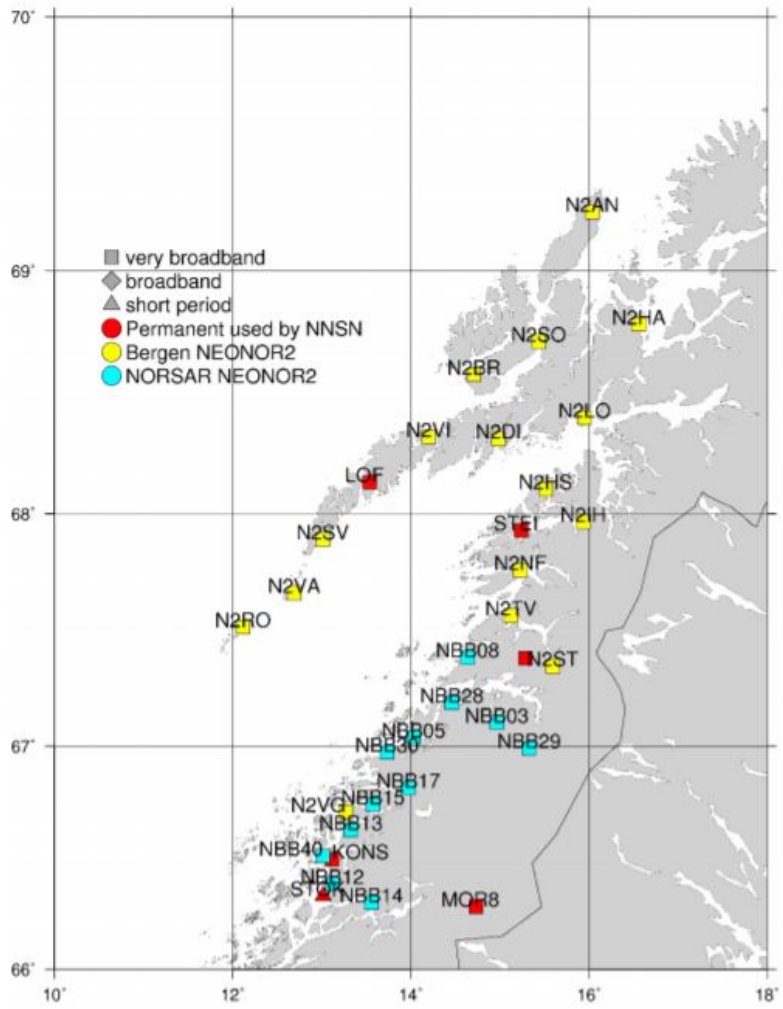

Figure 2.8: Map of the seismic stations in the NEONOR2 project area (Michálek et al., 2018)

#	Station code	Location	Institution	Locality description	Lat	Long	Alt	Seismometer	Digitizer	Telemetry	Date of installation
1	N2AN	Skarsteinsdalen, Vesterålen	UIB	Quiet area, on floor of building in old military facility	69,2371	16,0353	61	Trillium 120PA	Taurus	ICE	19.08.2013
2	N2BR	Breivik, Vesterålen	UIB	Basement of private house	68,5788	14,7075	10	Trillium 120PA	Taurus	none	21.08.2013
3	N2DI	Digermulen	UIB	Basement of private house, thought to be on bedrock	68,3134	14,9863	9	STS2.5	EDR-210	none	22.11.2013
4	N2HA	Harstad, Vesterålen	UIB	In storage area of Hålogaland Kraft; expected to be noisy	68,7839	16,5611	14	Trillium 120PA	Taurus	ICE	20.11.2013
5	N2HS	Hamsund, Hamarøy	UIB	Birthplace of Knut Hamsun, Nordlandsmuseet, Hamsunstiftelsen	68,1033	15,5136	15	STS2.5	EDR-210	GSM	23.10.2013
6	N2IH	Innhavet, Hamarøy	UIB	Garage at private house	67,9662	15,9367	28	STS2.5	EDR-210	ICE	23.10.2013
7	N2LO	Lødingen, Vesterålen	UIB	In quiet storage area of Hålogaland Kraft	68,4004	15,9533	10	Trillium 120PA	Taurus	GSM	19.08.2013
8	N2NF	Nordfold, Steigen	UIB	Small house behind church, near shore	67,7610	15,2277	3	STS2.5	EDR-210	ICE	24.10.2013
9	N2RO	Røst Kommunehus	UIB	Basement of building (said to partly rest on rock). Røst "main" street rather close, but not much traffic, even in rush hours	67,5173	12,1158	4	STS2.5	EDR-210	ICE	01.11.2013
10	N2SO	Sortland, Vesterålen	UIB	In underground vault	68,7139	15,4380	1	Trillium 120PA	Taurus	ICE	23.08.2013
11	N2ST	Straumen, Sørfold	UIB	Garage/basement at elderly home	67,3487	15,5959	11	STS2.5	EDR-210	ICE	22.10.2013
12	N2SV	Sørvågen, Moskenes Kommune	UIB	Installed in garage	67,8914	13,0098	21	STS2.5	EDR-210	ICE	21.11.2013
13	N2TV	Tårnvik, Salten	UIB	Basement of private house (built on sand, moraine)	67,5675	15,1252	5	STS2.5	EDR-210	ICE	25.10.2013
14	N2VA	Værøy Kommunehus	UIB	Basement of building (said to partly rest on rock). Værøy "main" street rather close	67,6639	12,6935	5	STS2.5	EDR-210	ICE	29.10.2013

Figure 2.9: List 1/2 of the NEONOR2 stations (Michálek et al., 2018)

#	Station code	Location	Institution	Locality description	Lat	Long	Alt	Seismometer	Digitizer	Telemetry	Date of installation
15	N2VG	Vågaholmen	UIB	Ground floor, smooth concrete floor on rock (said). End of road, no traffic, one house and garage nearby (used rarely)	66,7090	13,2690	8	Trillium Compact 120	Taurus	GSM	27.04.2015
16	N2VI	Vinje, Gimsøy	UIB	Basement of private house, thought to be on bedrock	68,3212	14,1976	9	STS2.5	EDR-210	ICE	21.11.2013
17	NBB03	Karbøl	NORSAR	Rarely used barn	67,1031	14,9681	187	CMG-3ESPC	EDR-210	GSM	13.03.2014
18	NBB05	Inndyr	NORSAR	Rarely used workshop in the town	67,0368	14,0306	13	CMG-3ESPC	EDR-210	GSM	12.03.2014
19	NBB08	Skaug Oppverkstsenter	NORSAR	Basement of a school	67,3871	14,6364	12	CMG-3ESPC	EDR-210	ICE	11.03.2014
20	NBB12	Aldersund Church	NORSAR	Basement of church	66,3870	13,1199	20	STS2.5	EDR-210	ICE	01.10.2013
21	NBB13	Garage	NORSAR	Garage on rocksite	66,6275	13,3272	27	STS2.5	EDR-210	ICE	03.10.2013
22	NBB14	Nordeng Farm	NORSAR	Under stairs in disused storage of a barn	66,3030	13,5586	35	STS2.5	EDR-210		02.10.2013
23	NBB15	Halsa Church	NORSAR	Storage room of cemetary workshop	66,7435	13,5776	50	STS2.5	EDR-210	GSM	04.10.2013
24	NBB17	Glomfjord Bårehus	NORSAR	Separate storage room in a morgue of Glomfjord Kirke	66,8161	13,9581	153	STS2.5	EDR-210	ICE	04.10.2013
25	NBB28	Valnes	NORSAR	Used to be a ground water take-out place. Almost on the rock, uphill, remote site.	67,1909	14,4622	45	CMG-3ESPC	EDR-210	ICE	12.03.2014
26	NBB29	Røkland skole	NORSAR	A chamber in a bomb-room of a school.	66,9919	15,3292	35	CMG-3ESPC	EDR-210	GSM	13.03.2014
27	NBB30	Finnes	NORSAR	Basement of a private house. On concrete which is coupled with bedrock.	66,9732	13,7354	20	CMG-3ESPC	EDR-210	GSM	14.03.2014

Figure 2.10: List 2/2 of the NEONOR2 stations (Michálek et al., 2018)

Chapter 3

Method

The objective of this thesis is to create a tool that estimates the Green's function from ambient seismic noise and use the Green's function to measure instrumental timing errors in seismic data. There are several processing steps between seismic noise and the Green's function, and I divide the processing into four main steps: preparing the data, pre-processing, cross correlation and stacking, and finally, measuring the timing errors.

All the processing has been performed using both MATLAB and SAC (Seismic Analysis Code). MATLAB has been the main tool, while SAC has mostly been used for quality check. The functions in MATLAB, have mostly been my own, but some inbuilt functions have also been used. The SAC functions were mostly inbuilt.

The stations used are mostly from the temporary NEONOR2 network (Michálek et al., 2018) operating from October 2013 until May 2016. In addition, there are some examples using the American stations ANMO and CCM from the IU network.

To check the sensitivity of the different aspects of the method, I run the process multiple times using different variables. The variables I test are the bandpass filters applied during pre-processing, the order and combinations of different types of normalizations, time windows for cross correlation, the stack length of the reference trace and the applied time delays. I also model a synthetic surface wave to compare with the found Green's function and investigate the directivity of the noise sources.

The processing procedure was developed using data recorded on the American stations ANMO and CCM in 2014, and on NBB30 and NBB28 from the NEONOR2 network, between the 1st of November 2014 to the 29th of June 2015. The examples in this chapter are therefore from these stations. I used these stations as test data, because ANMO and CCM from the IU network, are much used examples in similar studies (Shapiro and Campillo, 2004; Bensen et al., 2007), and because data

recorded on NBB30 and NBB28 was continuous and had no gaps in this period. (figures 3.1 and 3.2).

3.1 Preparing the data

The seismic data was retrieved as day-long miniseed files with sampling rate 100 Hz from the GFZ database and EIDA server (European Integrated Data Archive), using Arclinkfetch in a Linux shell script. Each file was converted to SAC-format and downsampled to 10 Hz in SAC. A preliminary quality check was then performed, where gaps were padded with zeroes and bad data removed.

Data from each station was retrieved for the entire period the station was operational. See figure 3.1 and 3.2 for an overview.

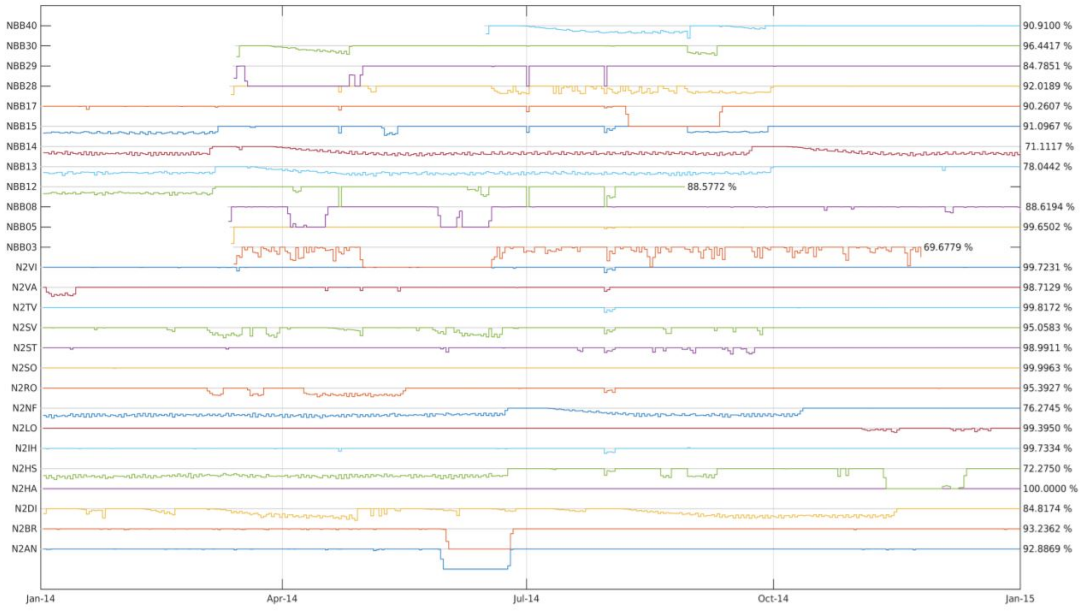

Figure 3.1: Data completeness Z-channels between Jan 1 - Dec 31, 2014. Total completeness in percentage is indicated on the right side (Michálek et al., 2018).

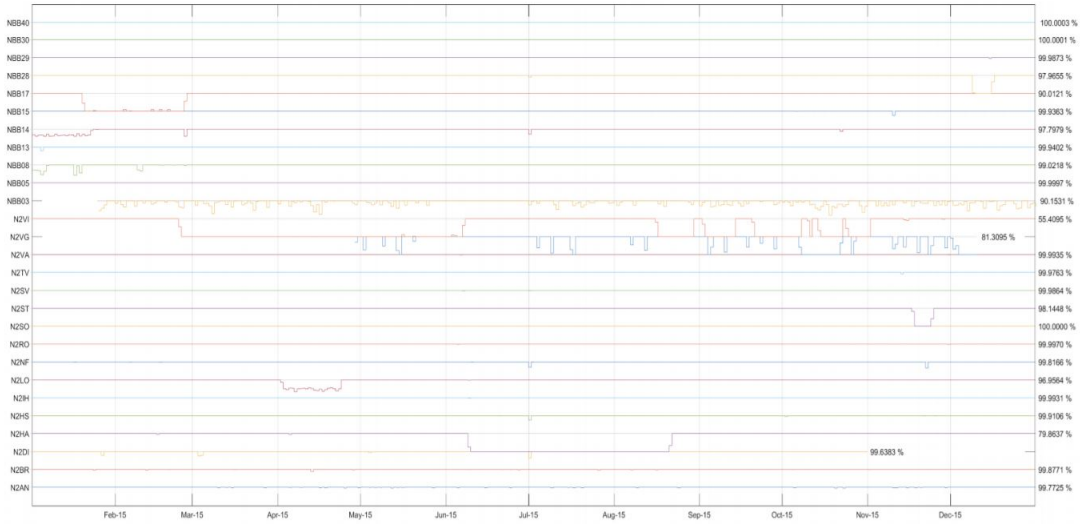

Figure 3.2: Data completeness Z-channels between Jan 1 - Dec 31, 2015. Total completeness in percentage is indicated on the right side (Michálek et al., 2018).

3.2 Preprocessing

The pre-processing steps were developed mainly following Bensen et al. (2007), which is a much-used processing procedure in noise correlation studies.

Each step in the pre-processing is done on shorter time windows. For most of the examples given here, the processing is done on day-long traces before cross correlation and stacking. However, both the processing and cross correlation is also performed on shorter time windows, this is discussed in the Cross correlation and stacking section.

3.2.1 Removal of mean and trend

The first step is to remove the mean and trend (figure 3.3). This is done using the inbuilt MATLAB function *detrend*, where the least-squares fit of a straight line is computed and subtracted from the data. The result of the operation can be seen in figure 3.3, where the mean and trend is removed from data recorded on station ANMO on the 4th of January 2004. The top plot shows that the signal is aligned around -3000, while the corrected bottom plot is centred around zero.

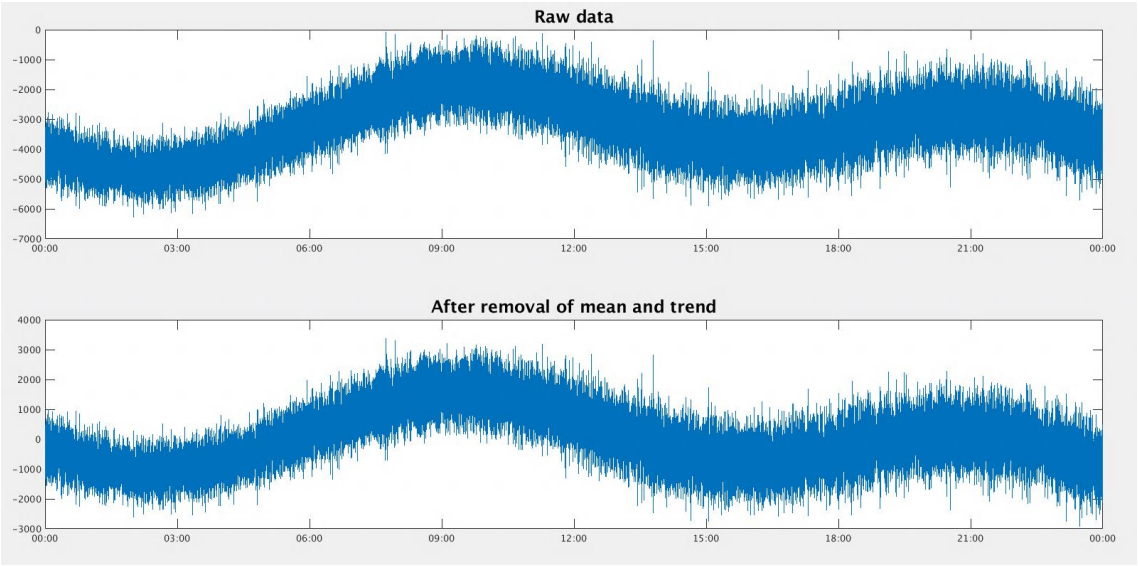

Figure 3.3: (a) Raw signal recorded on ANMO on January 4th 2004. (b) The signal in a. after mean and trend are removed.

3.2.2 Taper

The data is tapered to improve the stability of the processing steps by ensuring that the ends of the time series decay smoothly to zero (Havskov and Ottemoller, 2010). I apply a cosine taper $z(t)$ where 5 % of each end are multiplied with the cosine function:

$$z(t) = \begin{cases} \frac{1}{2}(1 - \cos(\theta(t))) & \text{first 5 \%} \\ \frac{1}{2}(1 + \cos(\theta(t))) & \text{last 5 \%} \end{cases}$$

Where $[0 \leq \theta(t) \leq \pi]$ see figure 3.4. This was done in MATLAB using my own function.

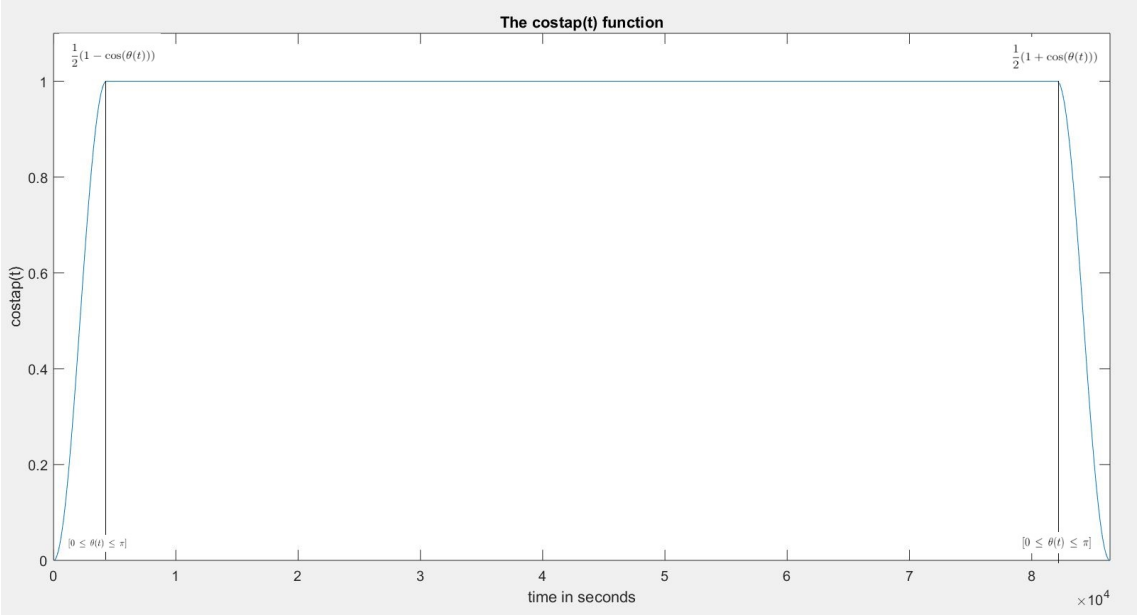

Figure 3.4: The cosine taper with the cosine function and θ indicated.

3.2.3 Filter

I used MATLAB's digital filter design function *designfilt* to design 4th order zero-phase Butterworth filters (figure 3.6 and 3.7), and *filtfilt* to implement the filters on to the data. The *filtfilt*-function filters the input data in both directions, and therefore does not alter the phase of the signal.

The seismic traces were bandpass filtered before and after the removal of instrument response. I apply the bandpass filter twice to avoid low frequency artefacts caused by the instrument response deconvolution. The signal and the amplitude spectrum after the different processing operations can be seen in figure 3.5. Note the high peak at very low frequency in the amplitude spectrum after the instrument response is removed (see arrow in figure 3.5(d)).

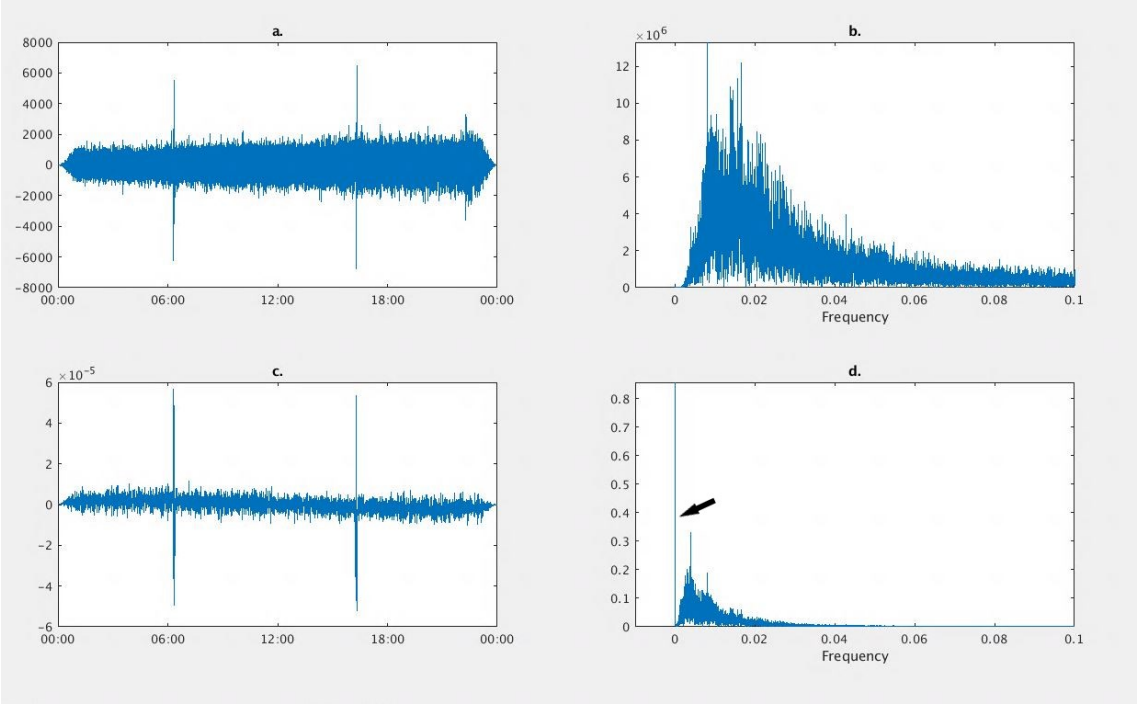

Figure 3.5: The signal (a) and amplitude spectrum (b) of data recorded on the station NBB30 on June 29th 2015. The mean and trend are removed, a taper is applied, and the signal is filtered between [0.005-1.5] Hz. (c) Same as a, but after the instrument response deconvolution. (d) Amplitude spectrum of c. Note that the amplitude scale is significantly different for b. and d.

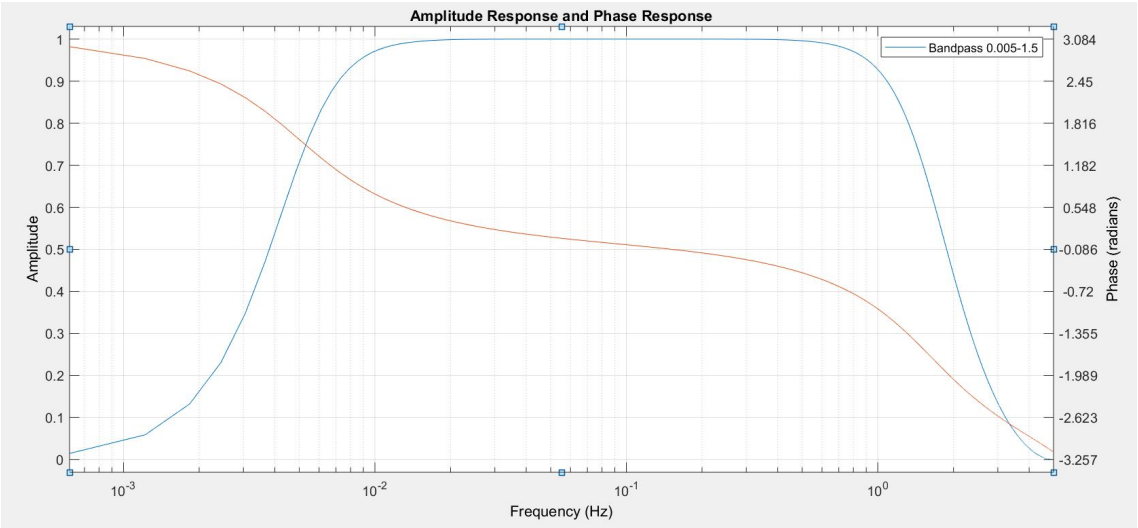

Figure 3.6: The amplitude (blue) and phase (red) response of the bandpass filter, [0.005-1.5] Hz, applied during the pre-processing process.

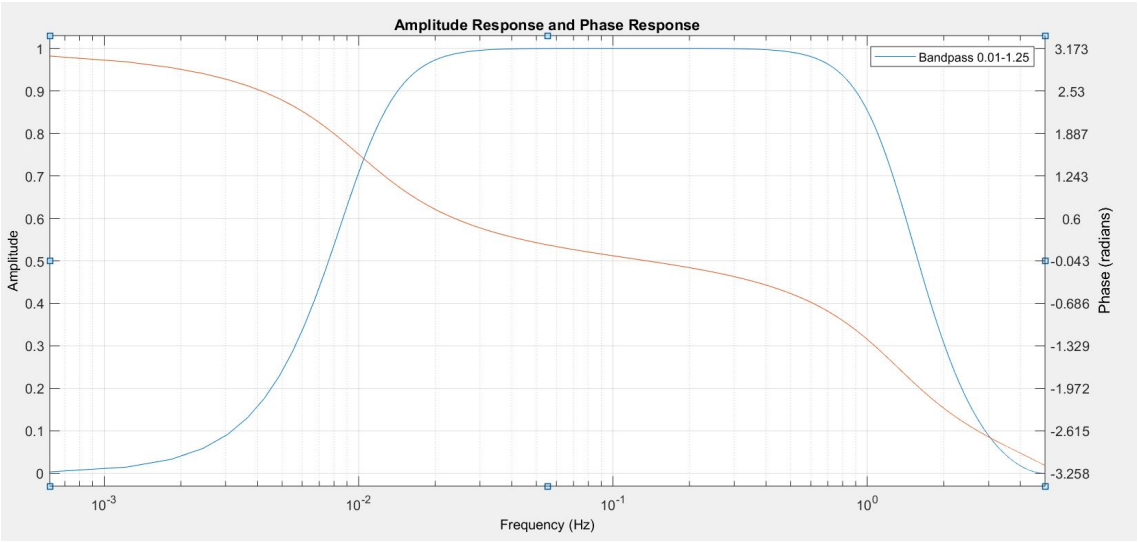

Figure 3.7: The amplitude (blue) and phase (red) response of the bandpass filter, [0.01-1.25] Hz, applied during the pre-processing process.

Frequency bands

The frequency bands I use to bandpass filter the signal depends on the area, the distance between the stations and which frequencies I want to investigate. I used two different bandpass filters on the daily traces prior to cross correlation. I used both a broad frequency band, [0.005-1.5] Hz (figure 3.6) and a more narrow band, [[0.01-1.25] Hz (figure 3.7), to test what effect different bandpass filters in the pre-processing have on the final results. I chose these frequency bands because noise above 1 Hz usually is caused by human activities (Demuth et al., 2016) and to avoid low frequency artefacts caused by the instrument response deconvolution, as mentioned above. Also, both frequency bands give more or less stable cross correlations throughout the test period (figure 3.8).

The two different bandpass filters give more or less the same waveforms, but different amplitude spectrum (figure 3.8 and 3.9).

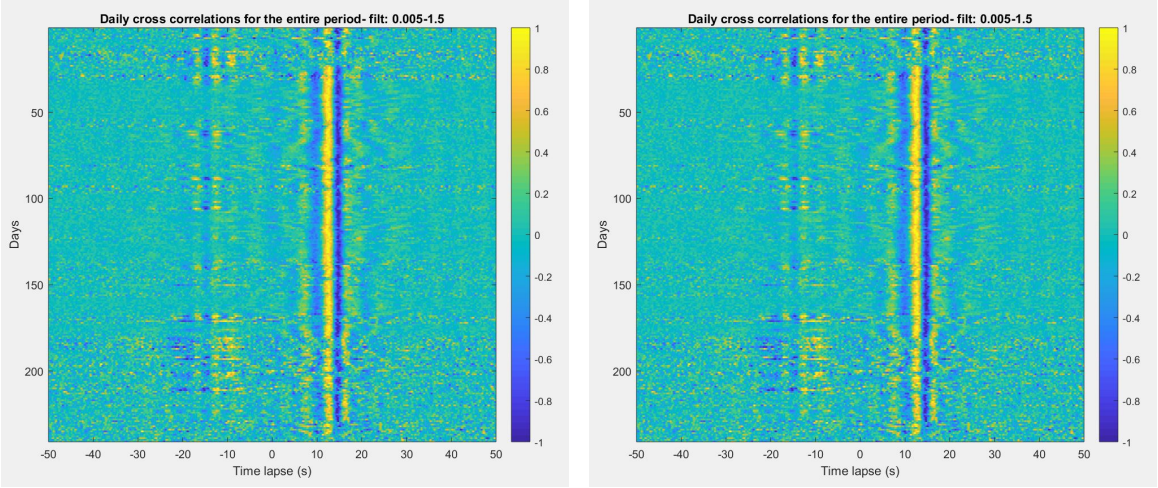

(a) **(b)**

Figure 3.8: The daily cross correlations plotted as a function of days and time lapse. The colour-bar to the right shows the amplitude scale. (a) Daily Cross correlations that are bandpass filtered with [0.01-1.25] Hz during the pre-processing. (b) Daily Cross correlations that are bandpass filtered with [0.005-1.5] HZ.

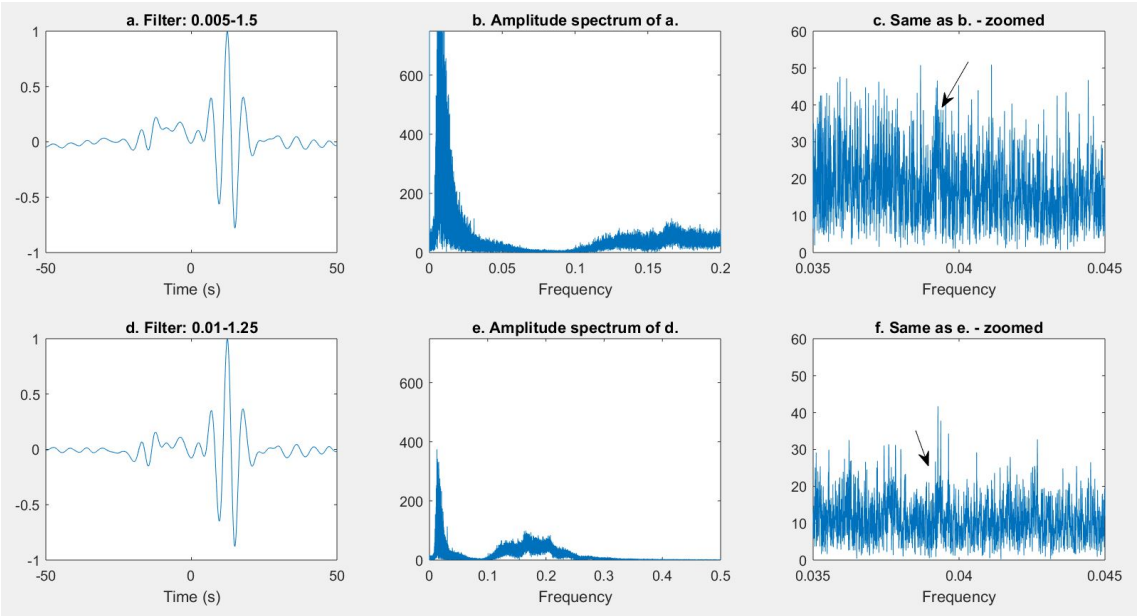

Figure 3.9: (a) Stacked cross correlation of data recorded on NBB30-NBB28 where the data has been bandpass filtered between [0.005-1.5] Hz during the pre-processing process. (b) Amplitude spectrum of a., (c) zoomed version of b. (d) Same as a., but filtered between [0.01-1.25] Hz, (e) Amplitude spectrum of d.,

The final stacked data were further filtered with narrow bandpass filters to enhance the different frequency components of the signal. Figure 3.10 and 3.11 show that surface waves between 1-20 s period are estimated from cross correlated noise recorded at NEONOR2 stations.

The signal-to noise ratio (SNR) was calculated for the causal and acausal part of the filtered signals and are indicated on each of end of the signals in figure 3.11. The SNR is calculated as the ratio between the RMS value of 30 s around the maximum peak, and the RMS value of 30 s noise at the signal edges:

$$SNR = \frac{Signal_{rms}}{Noise_{rms}} \tag{3.1}$$

The narrow bandpass filters were applied to both the cross correlations of the onebit normalized signal (figure 3.10) and the cross correlation of the normalized and spectral whitened signal (figure 3.11). Although the cross correlation of the onebit normalized signal and cross correlation of the spectral whitened signal show the same frequencies, the amplitudes vary greatly. The main part of the signal, at 5 s period, has approximately the same amplitude. However, the spectral whitened signal has much higher amplitudes at high frequencies (figure 3.11, top signal), compared to the onebit normalized signal where the low frequency amplitudes are higher (figure 3.10, bottom signal). This is consistent with the high amplitude peak found in the amplitude spectrum of the onebit normalized noise correlation (figure 3.9b. and d.). The dispersive properties of the noise correlations are discussed in the result chapter.

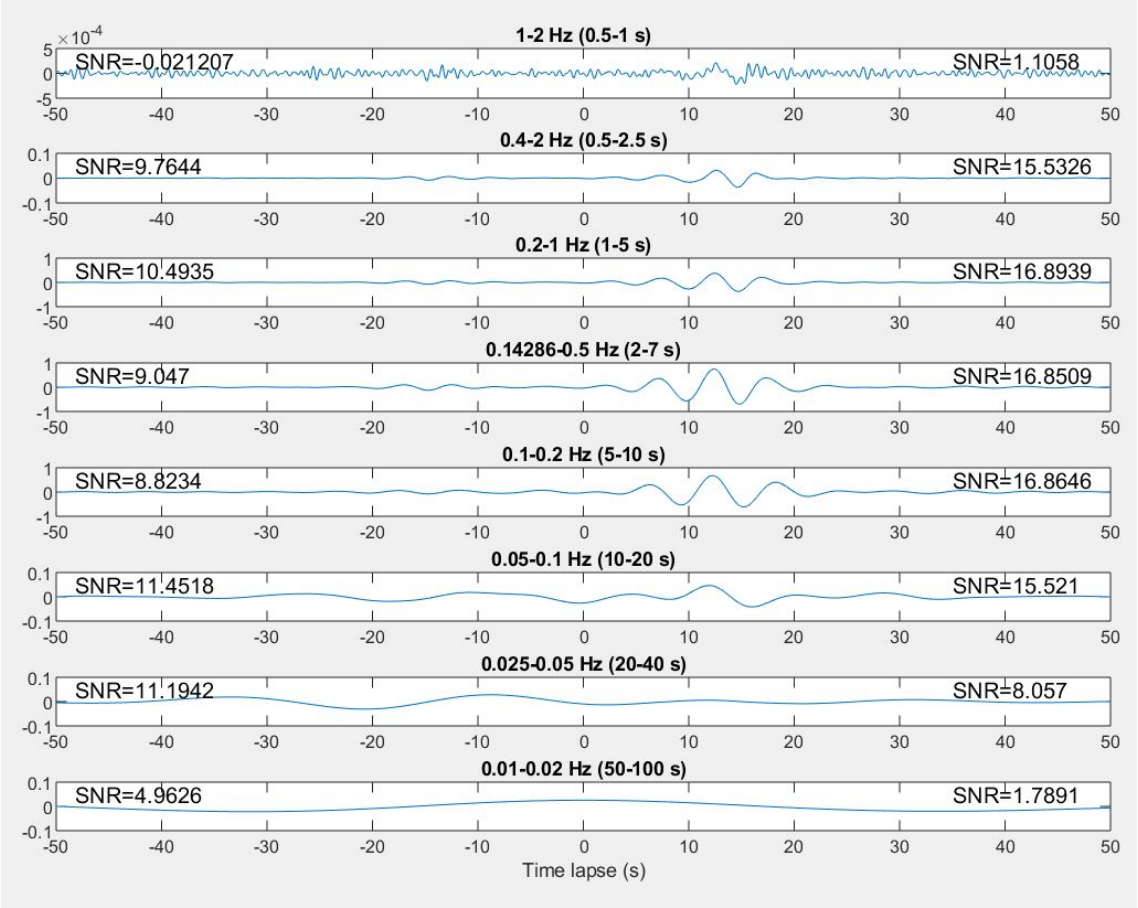

Figure 3.10: Cross correlation of onebit normalized noise recorded between November 1th 2014 to June 29th 2015 on stations NBB30 and NBB28, filtered in different frequency bands. The SNR of the causal and acausal part of the signal is indicated at each end.

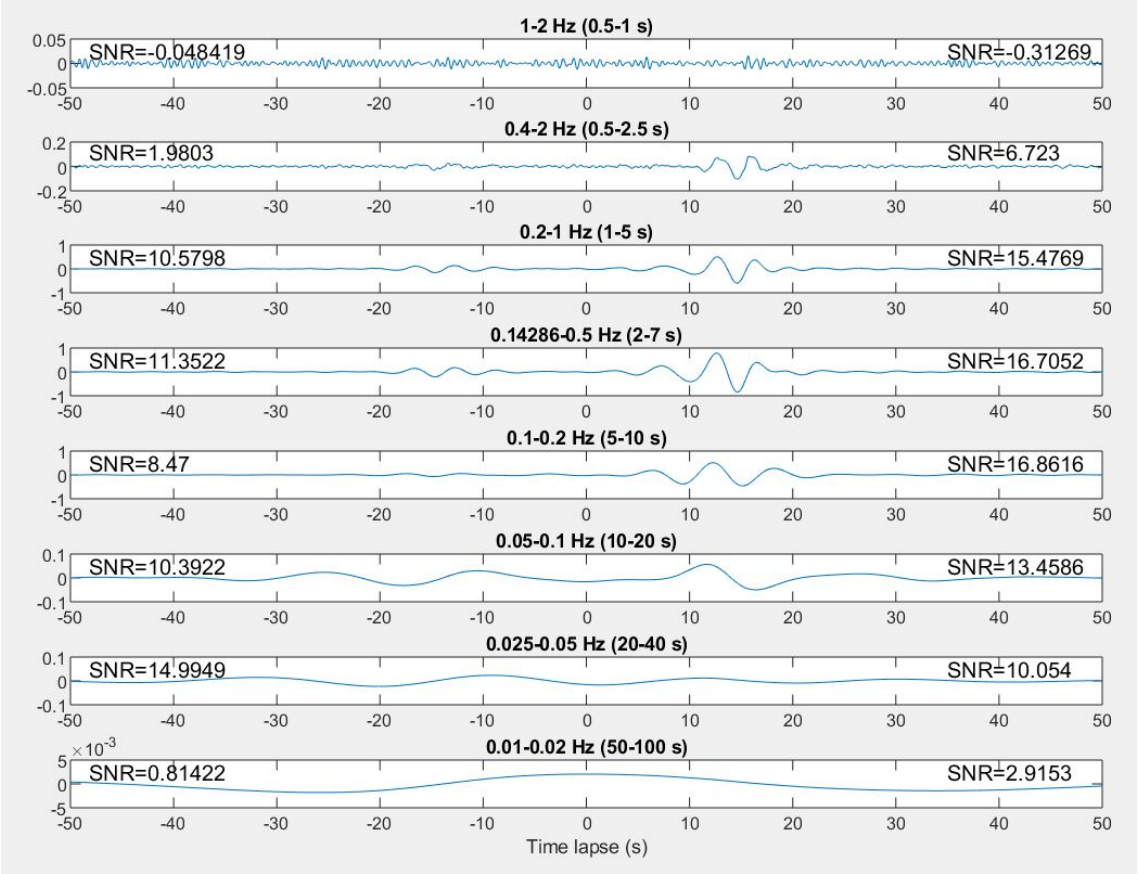

Figure 3.11: Cross correlation of onebit normalized and spectral whitened noise recorded between November 1th 2014 to June 29th 2015 on stations NBB30 and NBB28, filtered in different frequency bands. The SNR of the causal and acausal part of the signal is indicated at each end.

Microseismic peaks

The amplitude spectrum of the cross correlated signal show several microseismic peaks (figures 3.12 and 3.16). The primary and secondary peaks, mentioned in the Background chapter, are situated around 10-20 s (0.05-0.1 Hz) and 5-10 s (0.1-0.2 Hz), respectively (Stehly et al., 2006). When zooming in, a peak at 26 s (0.038 Hz) also appears (figure 3.12(b)). The microseism at 26 s is visible at stations in Northern America, Europe and Africa (Shapiro et al., 2006), but is more clear on the American stations ANMO and CCM than the NEONOR2 stations (figure 3.16(b)). In addition, there is a high amplitude peak at low frequency, around 50-100 s period (0.02-0.01 Hz). This peak is most likely caused by the Earth "hum" Rhie and Romanowicz (2004). This low frequency peak appears in the amplitude spectrum of all the NEONOR2 stations, but is especially dominant for station pair combinations of NBB30, NBB28 and NBB29, where the primary microseismic peak completely

drowns in the high low frequency peak (figures 3.13 3.12(a)). These stations all have 60 s seismometers (figure 2.10), with relatively high low frequency noise, see power spectrum in figure 3.14. The high amplitude peaks at low frequencies observed in the amplitude spectrum of stations pairs involving these stations, is therefore most likely caused by a combination of the Earth "hum" and low frequency instrumental noise from the stations. In the signal, the low frequencies are visible in the cross correlation of the onebit normalized signal at longer times (figure 3.15). Data from these stations should ideally be filtered at higher frequencies, but as can be seen in figure 3.15, the long period noise does not have significant effect on the Green's function.

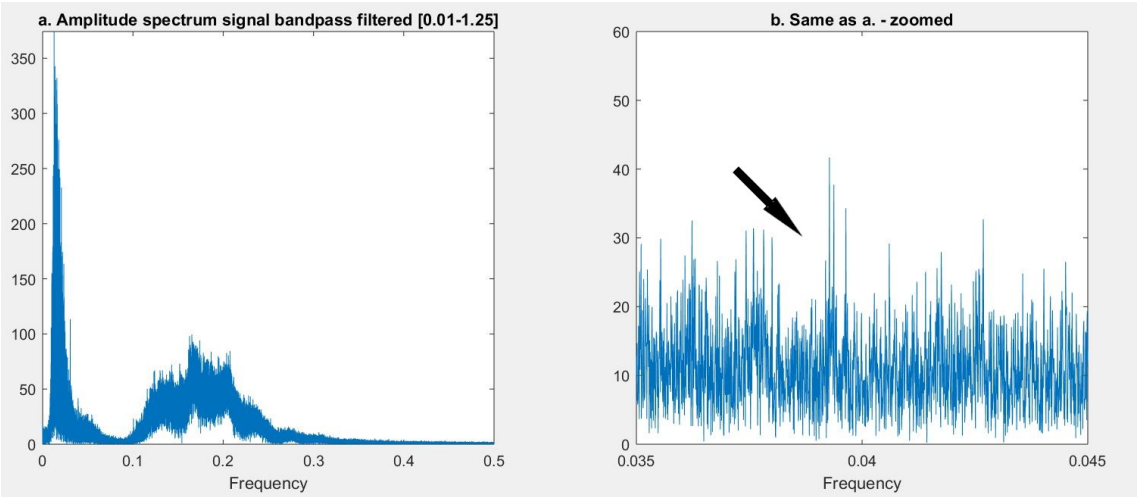

Figure 3.12: (a) Amplitude spectrum of cross correlated data from the NEONOR2 stations NBB30 and NBB28. (b) The same as a., but zoomed in on the microseism at 26 s (0.038 Hz)

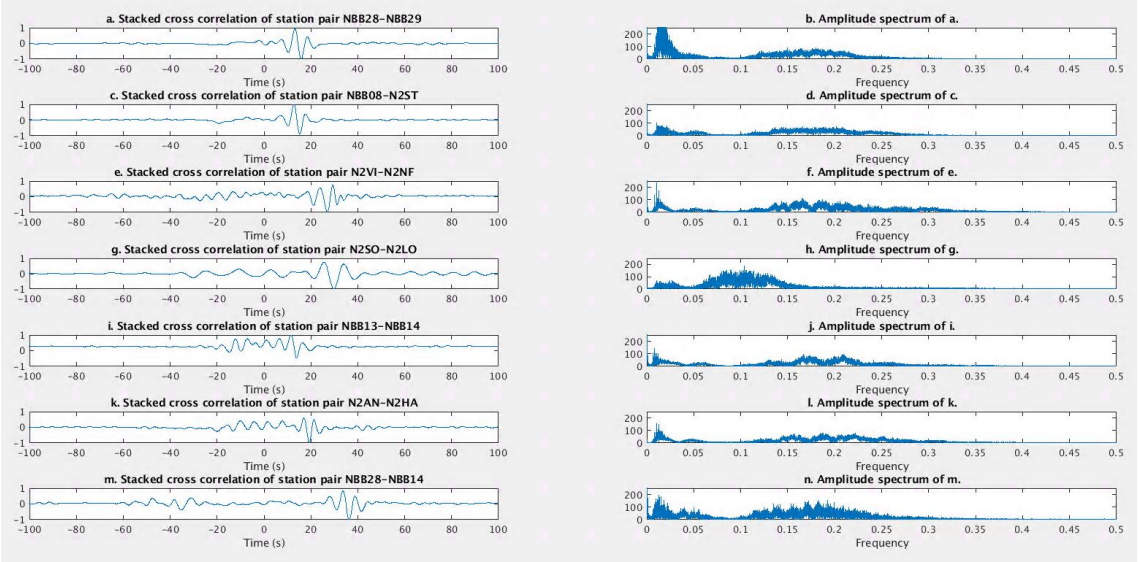

Figure 3.13: Noise correlation and amplitude spectrum of cross correlated data from a selecting of NEONOR2 stations.

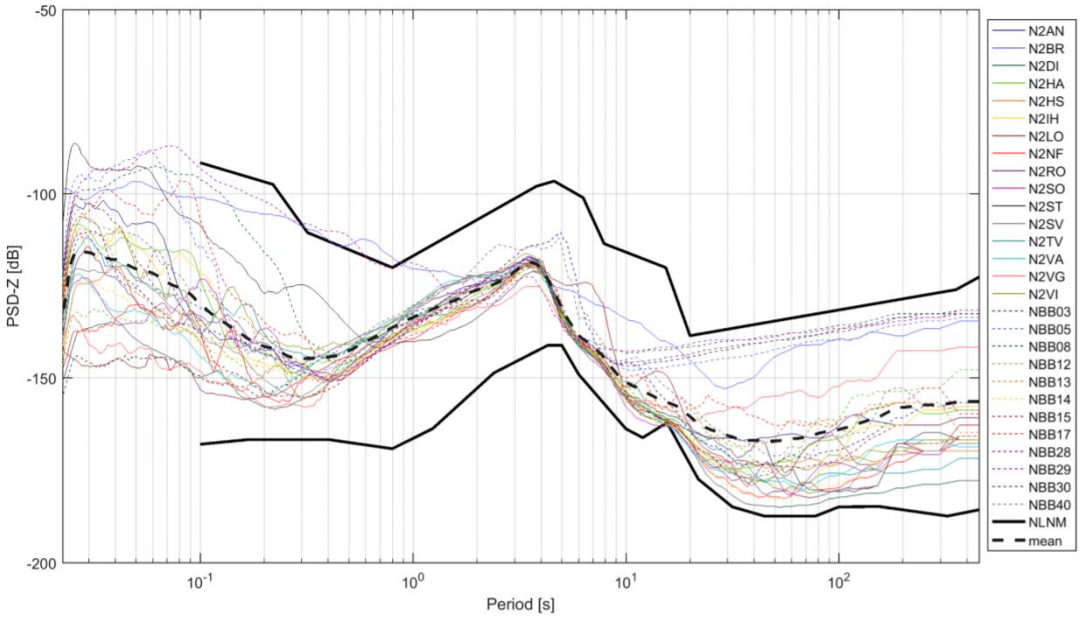

Figure 3.14: Power spectral density spectra of noise recorded on all the NEONOR2 stations in May 2014 (Michálek et al., 2018)

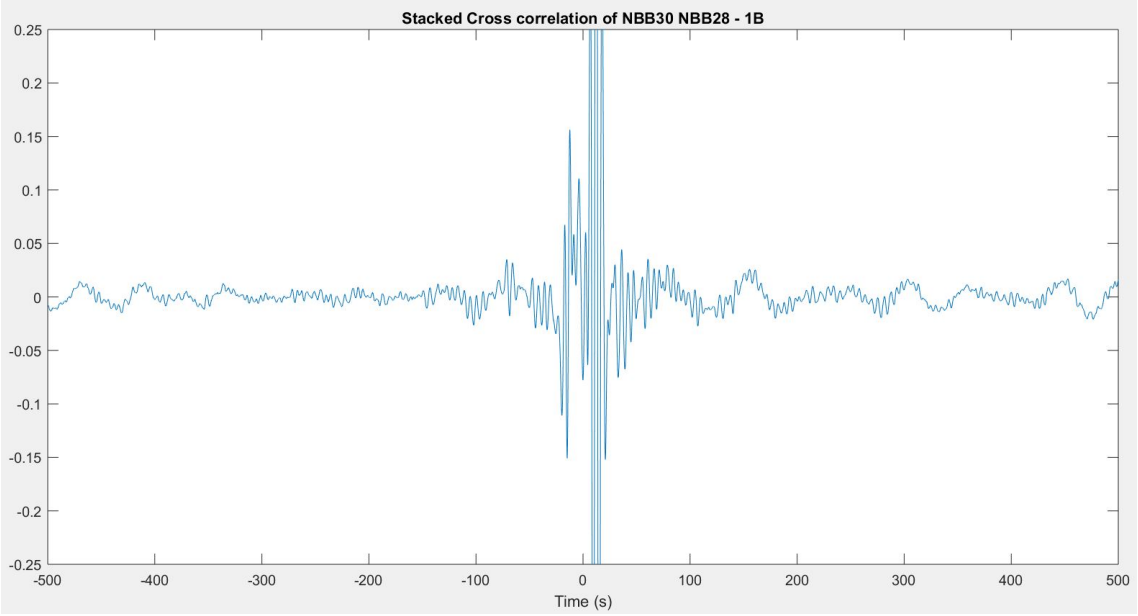

Figure 3.15: When looking at the cross correlation of the onebit normalized signal at longer times, a long period signal becomes visible.

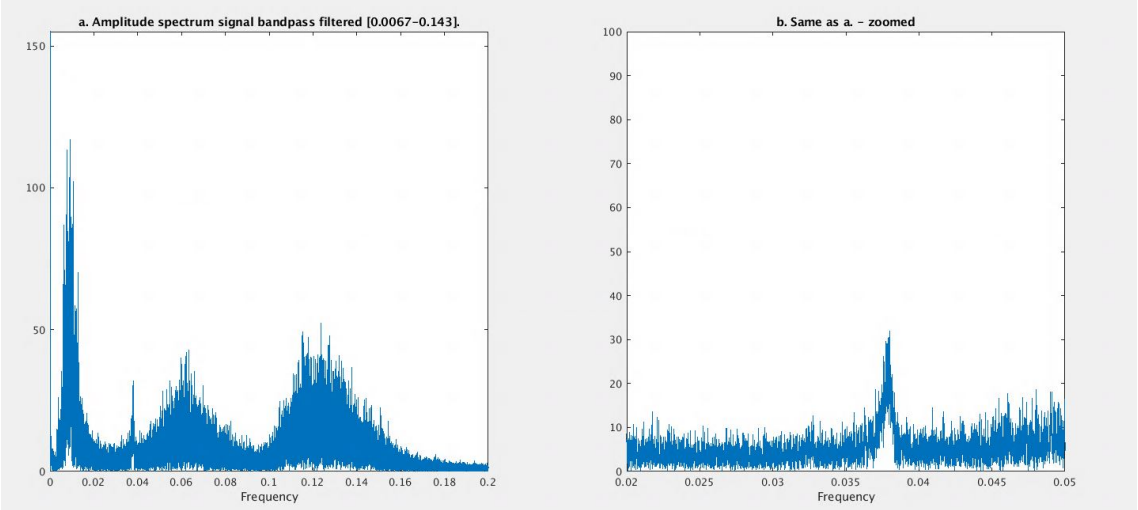

Figure 3.16: (a) Amplitude spectrum of cross correlated data from the American stations ANMO and CCM. (b) The same as a., but zoomed in on the microseism at 26 s (0.038 Hz)

When testing different filters with various frequency bands in the pre-processing process, one observation is that certain cut-off frequencies can strongly affect the shape of the microseismic peaks. This is especially true for the low frequency peak

above 50 s, and the microseism at 26 s. This effect demonstrates the importance of carefully choosing frequency band for filtering in the pre-processing process.

I have tested different filters with cut-off frequencies close to some of the microseismic peaks, the result can be seen in figures 3.9 and 3.17. Cross correlations that are bandpass filtered with small lower cut-off frequencies ($< 0.01Hz$), show sharp high amplitude peaks at low frequencies, centred around 0.01 Hz, see figures 3.9(e) and 3.17((e) and (h)). The same tendencies can be seen when using a cut-off frequency close to the microseism at 26 s (0.038 Hz). For the cross correlation of noise recorded on the American stations ANMO and CCM, the narrow band filter [0.008-0.07] Hz, gives a microseism at 26 s that is clearly visible even without zooming (figure 3.17(h)). This has a clear effect on the waveform (figure 3.17(g)). A similar effect can be seen for the cross correlation of noise recorded on the NEONOR2 station NBB30 and NBB28, though less clearly. The narrow band filter [0.01-1.25] Hz, gives a higher amplitude peak around 26 s (figure 3.9(f)), than the bandpass filter [0.005-1.5] Hz (figure 3.9(c)).

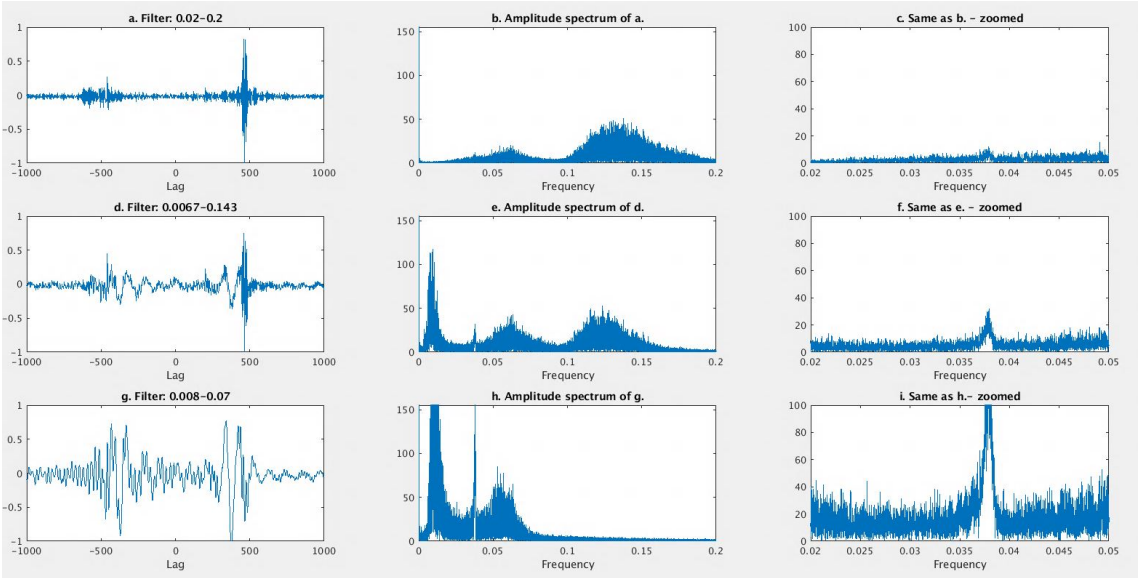

Figure 3.17: (a) Stacked cross correlation of data recorded on ANMO-CCM where the data has been bandpass filtered between [0.008-0.07] Hz during the pre-processing process. (b) Amplitude spectrum of a., (c) zoomed version of b. (d) Same as a., but filtered between [0.0067-0.143] Hz, (e) Amplitude spectrum of d., (f) zoomed version of e. (g) Same as a., but filtered between [0.02-0.2] Hz, (h) Amplitude spectrum of g., (i) zoomed version of h.

These findings show that it can be necessary to compromise between a broad bandpass filter and the effect of microseismic peaks. In the case of the NEONOR2 station, the narrower bandpass filter [0.01-1.25] Hz, gives less sharp peaks at low frequencies,

but a sharper microseism peak at 26 s, compared to the bandpass filter [0.005-1.5] Hz. An alternative is to normalize the cross correlation in the frequency domain by applying spectral whitening. This method will be explained later in this chapter.

3.2.4 Removal of instrument response

The instrument response is removed to recover the ground displacement of the signal. This is done so that the seismogram is displayed in terms of displacement instead of counts (Havskov and Alguacil, 2010).

The instrument response function is given by a set of poles and zeros. The pole-zero file is extracted from SEED files using *RDSEED*. The instrument response function is removed using the MATLAB function *transfer*, where the correction is done by deconvolving the instrument response function from the data.

3.2.5 Time domain normalization

Time domain normalization reduces the effect of earthquakes and instrument irregularities (Bensen et al., 2007). There are several different normalizations procedures described for the noise correlation method. A much used-method is the onebit (1B) normalization method, where the amplitudes are completely disregarded by setting all amplitudes above zero to 1 and all amplitudes below zero to -1. Onebit normalization increases the signal to noise ratio, but is controversial because it changes the amplitudes radically and can negatively influence the frequency content of broad band series (Larose et al., 2004; Sabra et al., 2005a). Several alternatives to onebit normalization are given by Bensen et al. (2007) including clipping and running-absolute-mean normalization. I use onebit-normalization mainly to save time, since it is both easy and fast to implement, but at the same time gives a satisfactory SNR.

The onebit normalization is done in MATLAB by dividing the seismic trace $x(t)$ with its absolute value. The absolute value is derived using the inbuilt MATLAB function *abs*.

$$x(t)_1 B = \frac{x(t)}{abs(x(t))} \tag{3.2}$$

The cross correlations in figure 3.18a. and b. are both the stack of the daily cross correlations without onebit normalization. However, in figure 3.18b. the daily cross correlations are normalized by setting the maximum to 1 prior to stacking. Figure 3.18 shows that the cross correlated signal without any normalization shows no resemblance to the Green's function, while the cross correlation with a simple normalization has similar shape to the cross correlation with onebit normalization.

This shows that the daily variations in amplitudes are so large that normalization is necessary prior to cross correlation.

The main difference between the two different normalizations shown here is the long period signal in the simple normalized cross correlation (figure 3.18b.). This is investigated further by comparing the amplitude spectrum and applying different highpass filters (figure 3.19). When frequencies below 0.01 Hz are removed, the simple normalized cross correlation becomes more similar to the onebit normalized. However, onebit normalization preserves the low frequencies and gives a sharper noise correlation than the noise correlation with a simple normalization. This shows that onebit normalization is an efficient and useful normalization operation.

The high amplitude peak at low frequencies in the amplitude spectrum of the onebit normalized noise correlation (figure 3.18d. right) are hidden in the signal, as shown in figures 3.15 and 3.10.

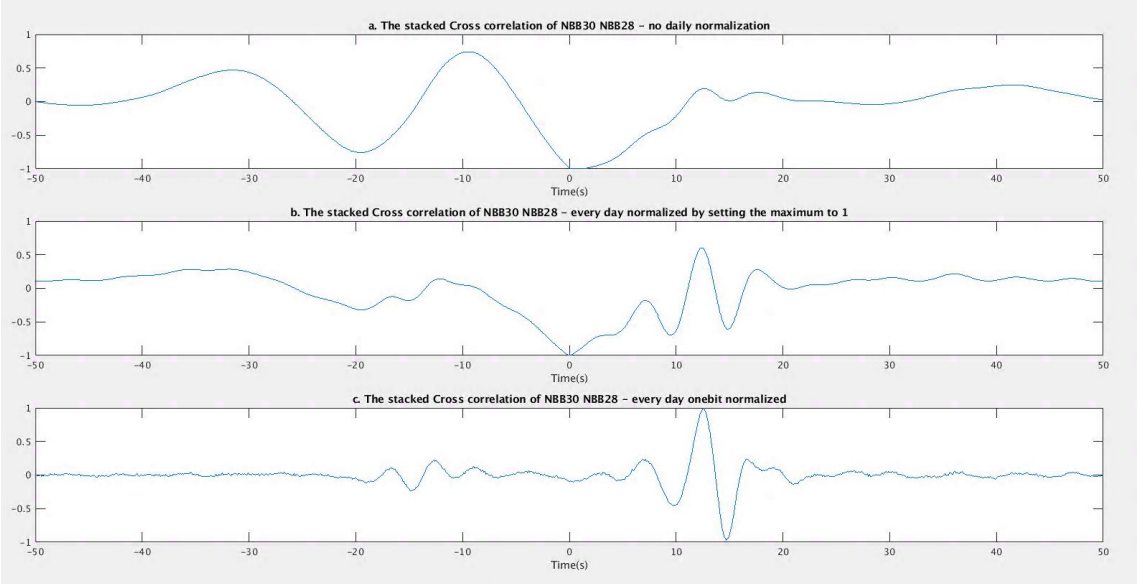

Figure 3.18: Noise correlation (a) without any daily normalization, (b) with every day normalized by setting the maximum to 1 and (c) with onebit-normalization.

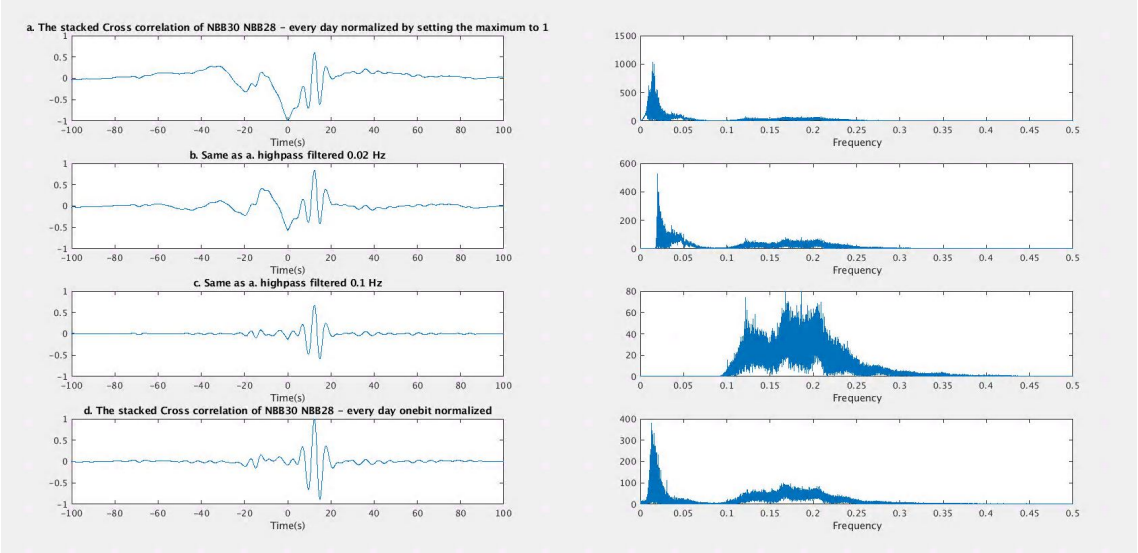

Figure 3.19: Noise correlation (left) and amplitude spectrum (right) where (a) every day is normalized by setting the maximum to 1 and (b) same as a., but highpass filtered at 0.02 Hz, (c) same as a., but highpass filtered at 0.1 Hz, (d) normalized with onebit.

3.2.6 Spectral whitening

As mentioned in the filtering section, ambient seismic noise has several microseismic peaks in the frequency domain (figure 3.20).

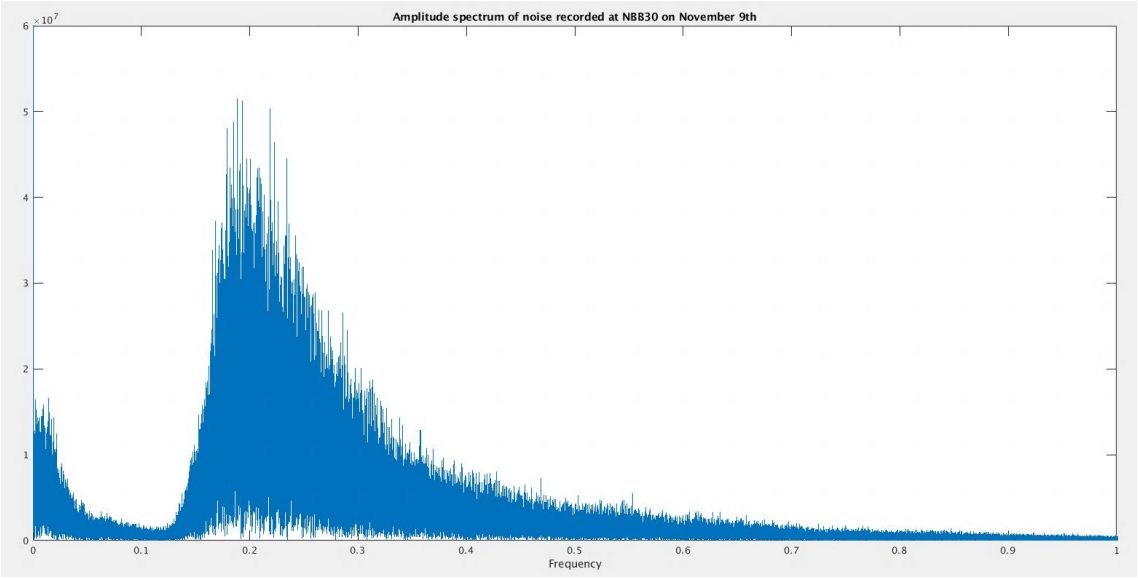

Figure 3.20: Amplitude spectrum of noise recorded on the station NBB30 on November 9th 2014. There are two significant peaks in the frequency domain.

Since these microseisms come from monochromatic sources, they can affect the waveform of the signal. Spectral whitening, normalization in the frequency domain, is therefore applied. Spectral whitening flattens the amplitude spectrum and thus creates a better distribution over frequency. This is done by applying a spectral whitening filter $f(n)$ to the amplitude $A(\omega)$ spectrum, and set the output close to 1:

$$f(n)A(\omega) \approx 1 \tag{3.3}$$

The spectral whitening filter then becomes:

$$f(n) \approx \frac{1}{A(\omega)} \tag{3.4}$$

To avoid that the whitened spectrum equals exactly 1, the amplitude spectrum is smoothed before dividing (Bensen et al., 2007). I have smoothed the amplitude spectrum by applying a third degree running average filter $y(n)$ (McClellan et al., 2007):

$$y(n) = \sum_{k=0}^{2} \frac{1}{3} A(n-k) \tag{3.5}$$

The running average filter is implemented using the inbuilt MATLAB function *filtfilt*. The smoothed spectrum $y(\omega)$ is then divided by the Fourier transform of the signal, before being transformed back to time domain. To avoid division with zero, a small constant α is added to the smoothed spectrum before dividing:

$$S(w) = \frac{F(w)}{\alpha + y(\omega)} \tag{3.6}$$

The effect of the running average filter on the amplitude spectrum can be seen on figure 3.21. The smoothed amplitude spectrum has noticeably less peaks and more stable amplitudes.

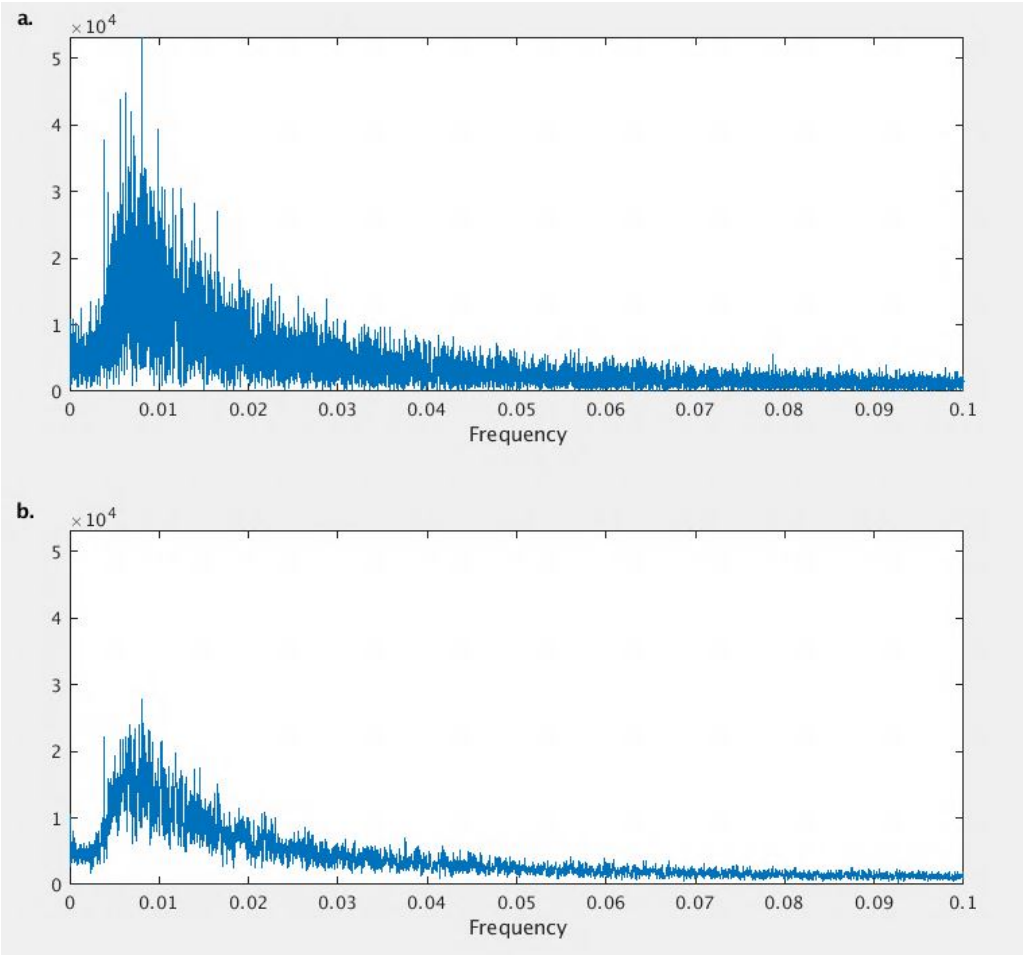

Figure 3.21: (a) The amplitude spectrum of data recorded on the station NBB30 on June 29th 2015. (b) Same as a, but smoothed by a third degree moving average filter

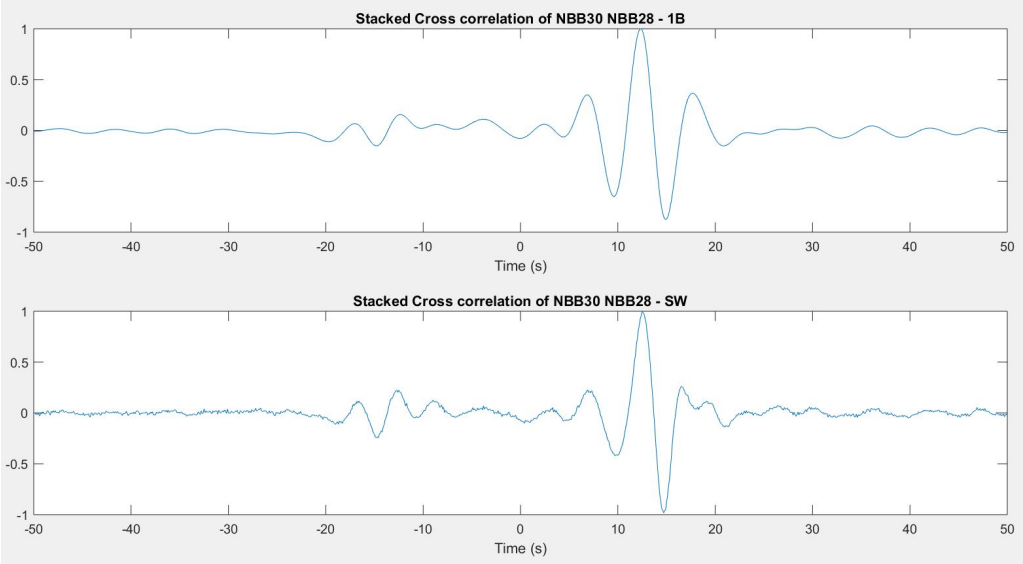

Figure 3.22: (a) The stacked cross correlated signal. A bandpass filter between [0.01-1.25] Hz and onebit normalization is applied prior to cross correlation. (b) The stacked cross correlated signal that is filtered between [0.01-1.25] Hz and both onebit normalized and spectral whitened prior to cross correlation.

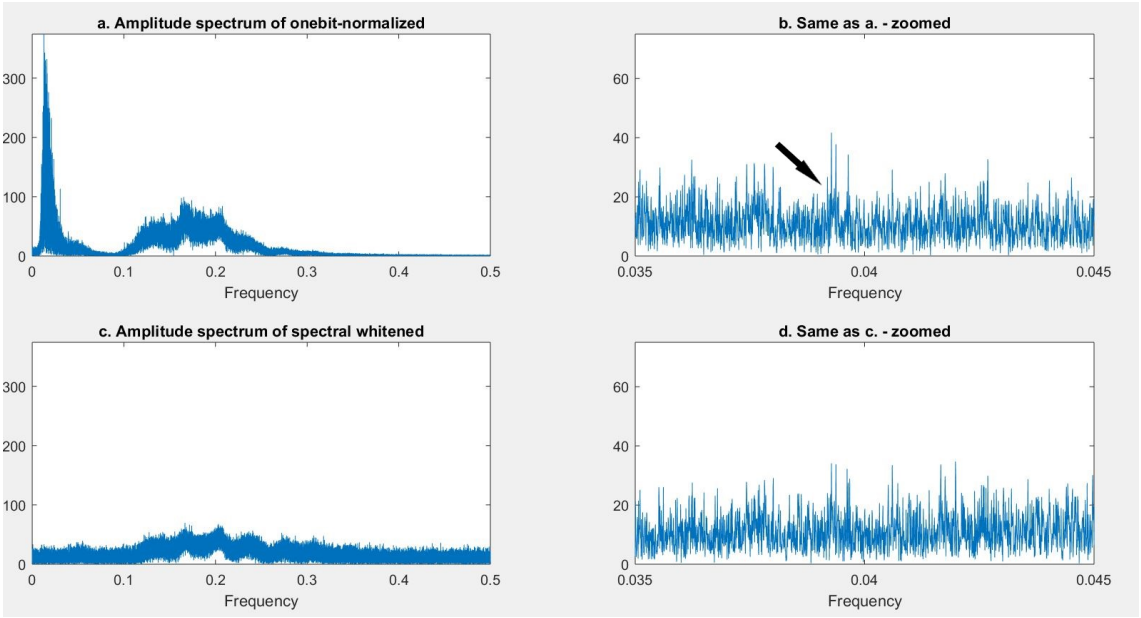

Figure 3.23: (a) Amplitude spectrum of noise correlation that is filtered between [0.01-1.25] Hz and onebit normalized prior to cross correlation. (b) Zoomed version of a. (c) Amplitude spectrum of noise correlation where spectral whitening is also applied prior to cross correlation. (d) Zoomed version of c.

The effect of the spectral whitening can be seen on the signal in figure 3.22, and the amplitude spectrum in figure 3.23. There is a noticeable difference between the signal with only onebit normalization and the signal with spectral whitening. The low frequency peak in the amplitude spectrum, is removed with spectral whitening. The second microseismic peak and the microseism at 26 s (fig. 3.23b and d) are still there, but with lower amplitudes.

3.2.7 The order of application

Since temporal normalization and spectral whitening induce non-linear changes to the signal, the order in which they are applied can affect the final result. Bensen et al. (2007) recommend applying spectral whitening after the time normalization, before the cross correlation. However, there are also studies where spectral whitening is applied before time normalization (Brenguier et al., 2008b; Groos, 2010). Spectral whitening can also be applied after cross correlation, before stacking, either as addition to the whitening done before the cross correlation, or as the only spectral whitening. This is either to broaden the frequency spectrum of the noise correlation, or to save time and computational cost (Bensen et al., 2007; Groos, 2010). I have tested these different approaches and calculated the SNR for the resulting waveforms to see if any of the approaches is better than others (3.24).

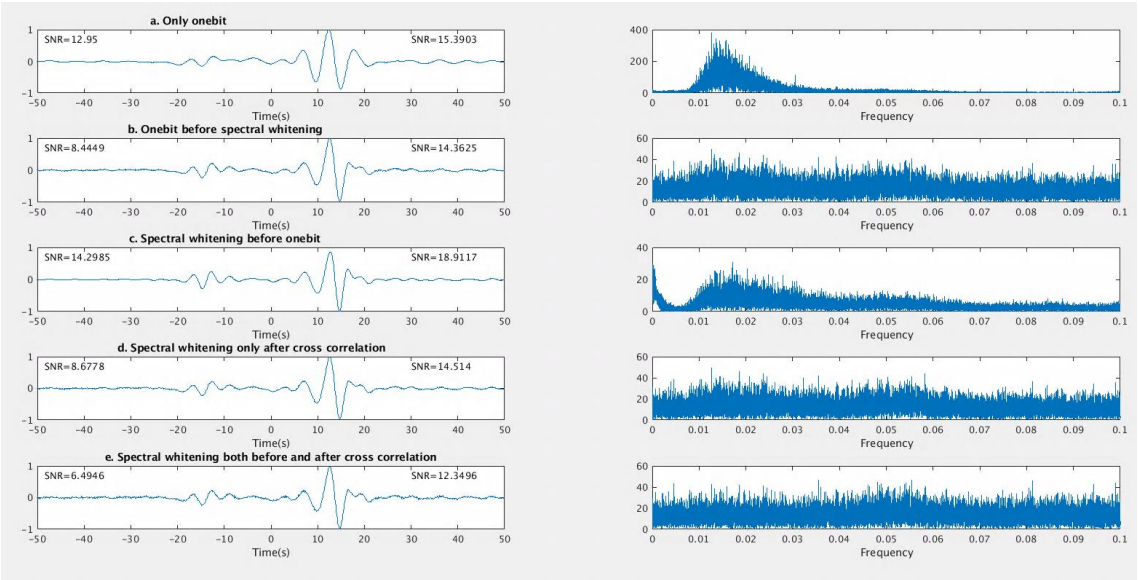

Figure 3.24: Noise correlation (left) and amplitude spectrum (right) after applying (a) onebit as the only normalization, (b) onebit prior to spectral whitening, (c) spectral whitening prior to onebit, (d) spectral whitening both before and after cross correlation, and (e) spectral whitening only after cross correlation

The main difference between the various combinations of spectral whitening and onebit-normalization, is seen on the amplitude spectrums. When spectral whitening is applied last, either before or after cross correlation, the spectrum is fairly flat. While onebit-normalization, clearly has an impact on the amplitude spectrum. The shape of the emerging Green's function, on the other hand, stays mostly the same, independently of the order. There is, however, a small variation in SNR, spectral whitening applied prior to onebit normalization gives the highest average SNR, but a less flat amplitude spectrum. Surprisingly enough, spectral whitening applied only after cross correlation, gives a higher SNR than spectral whitening applied both before and after. This shows that spectral whitening, has a significant effect on the noise correlation signal and should be used with caution. Spectral whitening also increases the high frequencies, a bandpass filter should therefore be applied after spectral whitening.

3.3 Cross correlation and stacking

Cross correlation is a method that measures the similarity between two signals x(t) and f(t). The cross correlation is done by evaluating the integral of the product of x(t) and f(t+L) where L is shifted by a lag time L:

$$C(L) = \int_{-\inf}^{+\inf} x(t)f(t+L)dt \tag{3.7}$$

The two functions are the most similar at the time shift, lag, where C(L) is maximum (Stein and Wysession, 2003).

After pre-processing, the daily traces are cross correlated and stacked. The cross correlation is done using my own MATLAB function where the second of the two traces is flipped right to left in time, before convolving. This is possible since the only difference between cross correlation and convolution is the sign of the time shift. The convolution is done in time domain using the inbuilt MATLAB function *conv*.

As mentioned in the Background section, averaging over time is necessary for the cross correlation of ambient seismic noise to properly convert towards the Greens function. This is done by stacking shorter time series, generally day-long or 6-hour segments. Since cross correlation is a linear operation, stacking of shorter cross correlated time series gives the same result as cross correlating longer time series (Bensen et al., 2007). In addition to providing randomization of the noise by averaging, stacking also gives higher SNR (Bensen et al., 2007; Shapiro and Campillo, 2004). The stacking is done using the inbuilt Matlab function *sum*.

The 10 first daily cross correlations compared to the stacked cross correlation, are shown in figure 3.25. The daily cross correlations vary largely day from day, while the stacking gives a clean signal with higher signal-to-noise ratio.

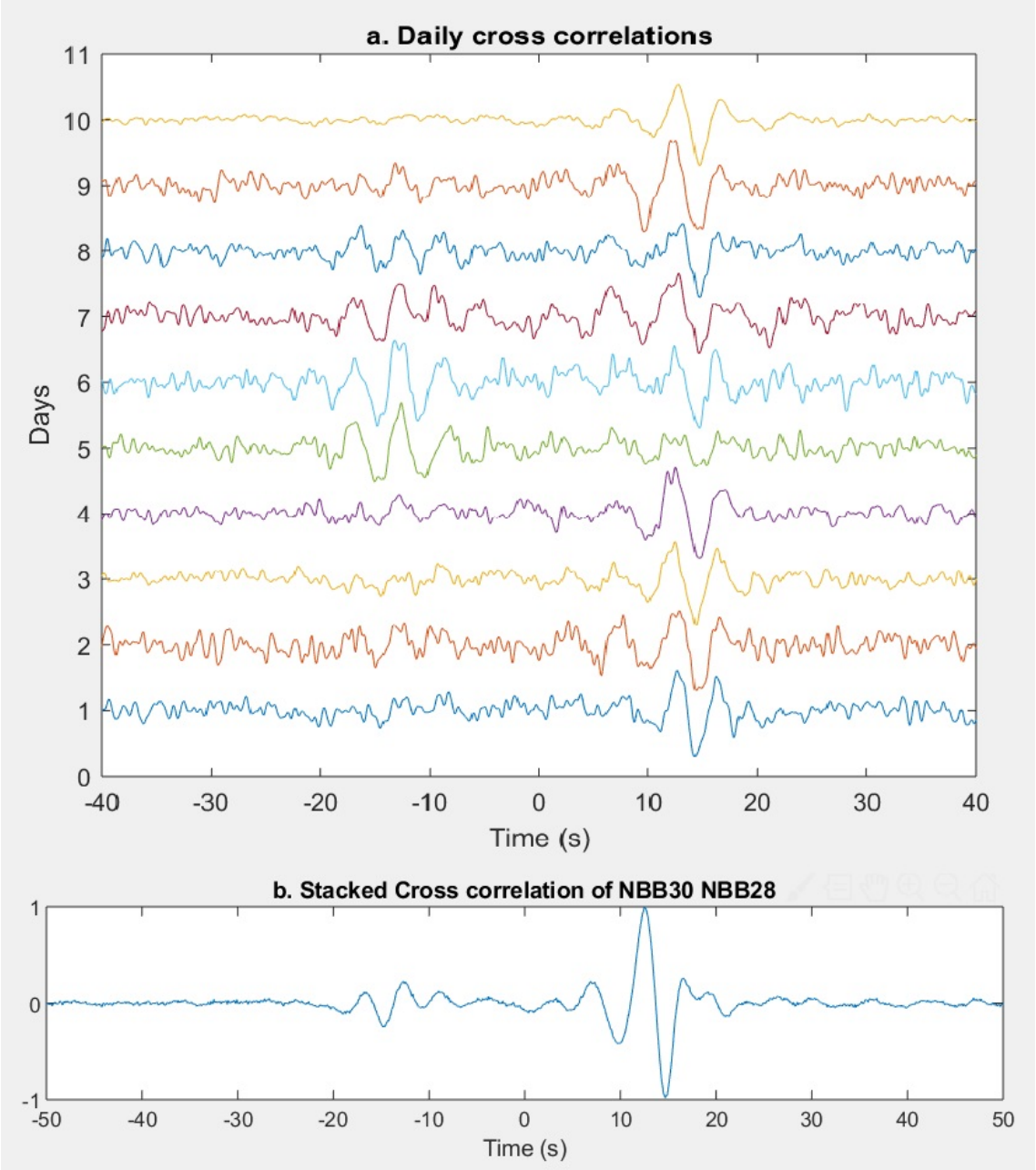

Figure 3.25: (a)The first 10 daily cross correlation of noise recorded at the stations NBB30 and NBB28. (b) The stacked cross correlation of all the test days.

3.3.1 Time window length

In the example given above, day-long traces are cross correlated and stacked over the entire available period. This is done to ensure averaging and randomization of

the noise sources. Most noise correlation studies cross correlate daily seismic traces and stack over a longer period. However, it is also possible to cross correlate shorter or longer time windows before stacking. I have applied the processing method and cross correlated time windows of varying length and stacked over different periods to see the effect these variables have on the estimated Green's function (figure 3.26).

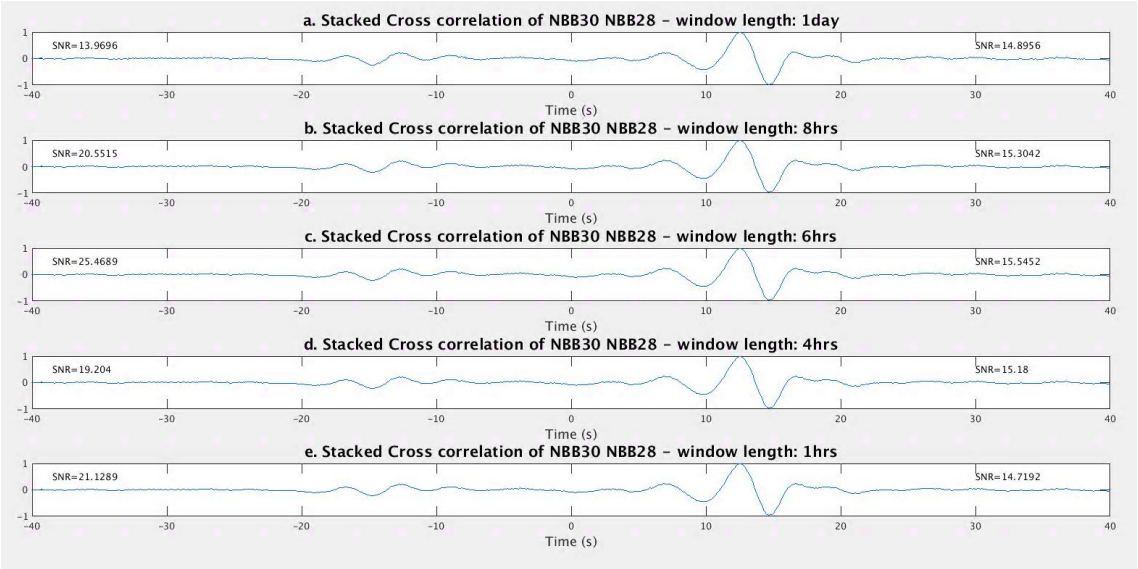

Figure 3.26: (a) The noise correlation of the station pair NBB30-NBB28 cross correlated over day long, (b) over 8-hour, (c) over 6-hour and (d) over 4-hour and (e) over 1-hour time windows.

From both comparing the waveforms and signal-to-noise ratios in figure 3.26, it is clear that cross correlating over different time window lengths has little effect on the final stacked noise correlation. This is because of the linear nature of the cross-correlation operation, as mentioned above. The computation time, on the other hand, is affected by the time window. Figure 3.27 shows that the computation time increases almost linearly with time window length. To save time, I therefore generally cross correlate over 6-hour time windows

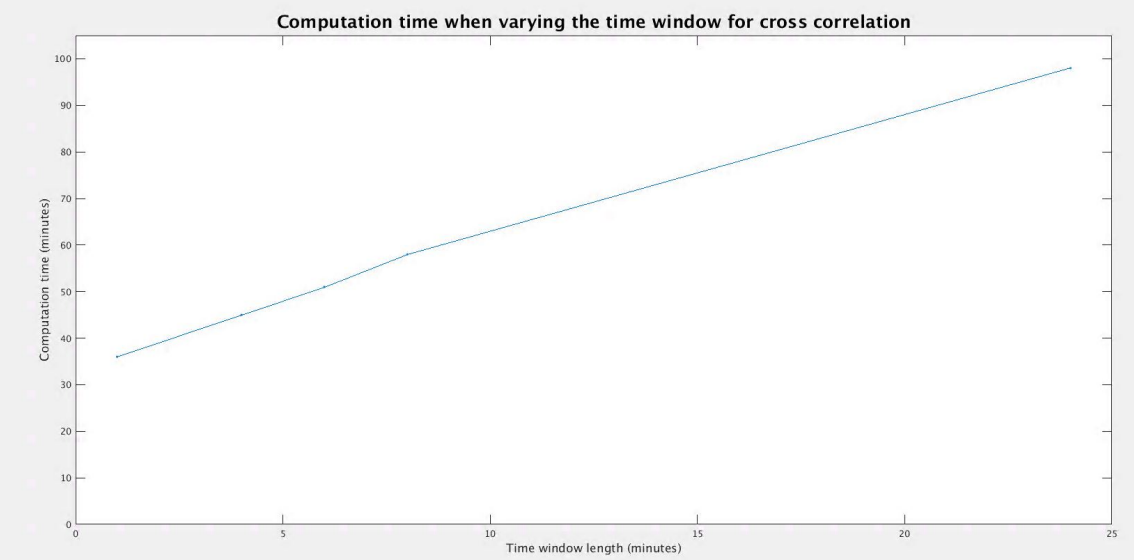

Figure 3.27: (a) The computation time to process and cross correlate noise recorded on the station pair NBB30-NBB28 between 1th of November 2014 and 29th of June 2015. The cross correlating is done over day long, (b) 6-hour (c) 1-hour time windows.

In figure 3.26 I have only applied the cross correlation to the smaller time windows, and used the same day-long time window for the pre-processing. Using smaller time windows also during preprocessing does little change to the final result (figure 3.28), but takes significantly longer to compute (figure 3.29).

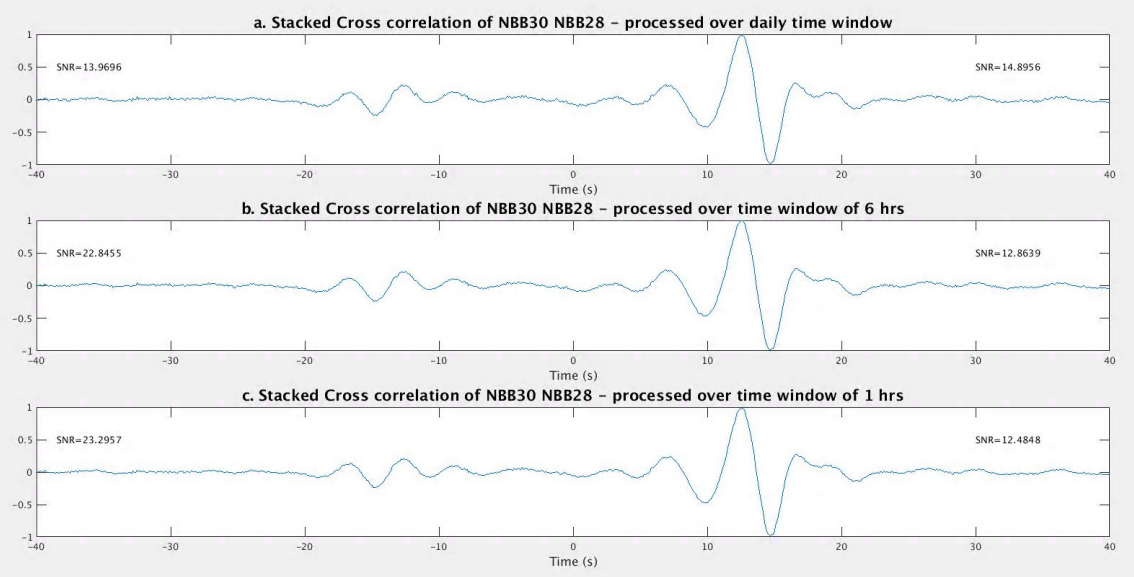

Figure 3.28: (a) The noise correlation of the station pair NBB30-NBB28 processed and cross correlated over day long, (b) over 6-hour and (c) over 4-hour time windows.

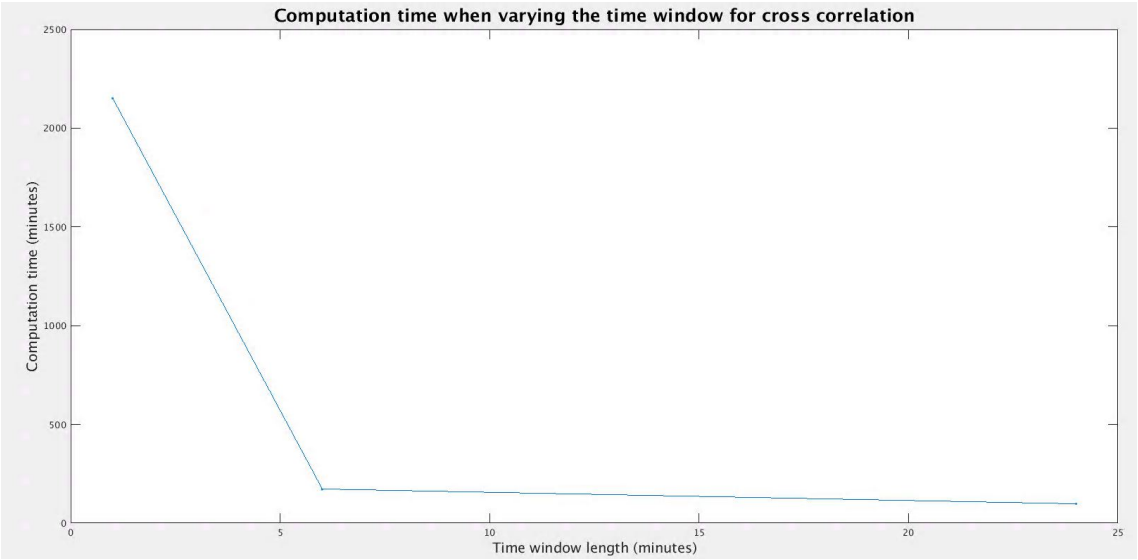

Figure 3.29: The computation time to process and cross correlate noise recorded on the station pair NBB30-NBB28 between 1th of November 2014 and 29th of June 2015. The processing and cross correlating is done over day long, 6-hour and 1-hour time windows.

3.4 Measuring the timing error

The main objective of this thesis is to develop a method to detect changes in the estimated Green's function, specifically changes caused by instrumental timing errors, Timing errors are usually caused by problems with the GPS receiver or digitizer, which can result in clock drift or sudden jumps in the data. When cross correlating seismic noise with timing errors, the estimated Green's function is shifted in time. Noise correlations can thus be used to detect possible instrumental errors.

I have mostly followed Stehly et al. (2007), Gouédard et al. (2014), and Sens-Schönfelder (2008) when developing the method to measure timing errors. According to Stehly et al. (2007), time shifts of the Greens function are mainly caused by three factors: change in noise distribution, property changes in the medium, or instrumental errors. These causes can be distinguished from each other by looking at the way the cross correlation is shifted. While a change in noise distribution will affect the causal and acausal time lags of the cross correlation independently (figure 3.30c), a change in property will cause the same change on both time lags (figure 2.6), and an instrumental error would shift the entire cross correlation in one direction, causing an asymmetric shift (figure 3.30b).

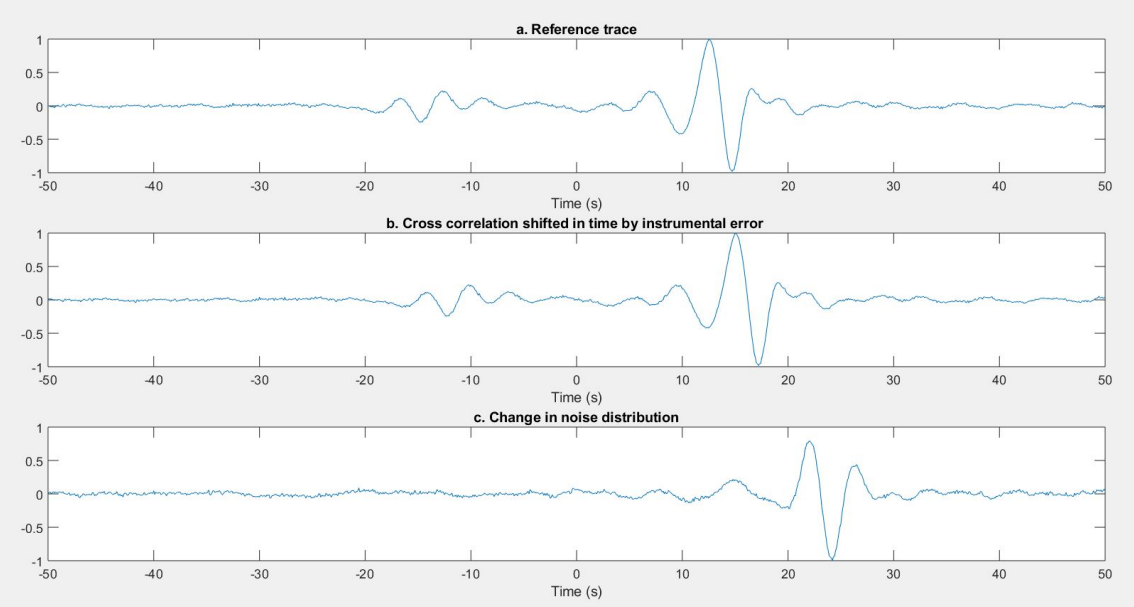

Figure 3.30: (a) The noise correlation of the station pair NBB30-NBB28 stacked over the test period (01.11.14-29.06.15), used as reference trace (b) The same noise correlation as in a., shifted by 2.5 s to illustrate a simple instrumental time shift. (c) The noise correlation of the station pair NBB30-NBB29, where the noise source distribution is different from that of the station pair in a.

To find time errors specifically caused by instruments, I therefore differentiate between one-sided time shifts and time shifts detected on both the causal, positive lag, and the acausal, negative lag, part of the signal. This is done by measuring the time delay for the causal and acausal part of the signal separately. I further make sure that the time delay of the negative side $d^-(t)$ and positive side $d^+(t)$ are caused by an asymmetric shift, following the condition:

$$d^+(t) \approx -d^-(t) \tag{3.8}$$

The time shift is measured by comparing the daily cross correlations $s(t)$ to a reference trace $r(t)$. I use cross correlations stacked over a specific period as reference. The length of this period depends on seasonal variations and availability of the data and is further discussed later in this chapter.

Prior to comparison, I separate the causal and acausal part of the reference and daily cross correlations and normalize by setting the absolute maximum to one. The daily correlations are compared to the reference using cross correlation, and the time shift

is measured as the time lag where the resulting correlation is maximum.

$$d(t) = max(r(t) * s(t)) \tag{3.9}$$

The resulting cross correlation is normalized using the autocorrelations:

$$\overline{d^+(t)} = \frac{d^+(t)}{max(\sqrt{((r^+(t) * r^+(t))(s^+(t) * s^+(t)))})} \tag{3.10}$$

To ensure that the daily cross correlations have converged towards the Green's functions, only the resulting cross correlations with correlation coefficient above a certain threshold are used. I set this threshold value to 0.4 following Sens-Schönfelder (2008). This is a relatively arbitrary constant, mainly chosen as an extra step to ensure quality measurements.

The final time delay d(t) is set as the average of the time shift found for each side, following the condition of equation 3.8.

$$d(t) = \frac{d^+(t) + (-d^-(t))}{2} \tag{3.11}$$

Since the reference trace is found from potentially erroneous data, I correct the cross correlations for the found time delays and run the measuring process again. The daily cross correlations are corrected using the Fourier transform and the shift theorem (McClellan et al., 2007):

$$y(n) = x(n - n_d) \leftrightarrow Y(\omega) = X(\omega)exp(-j\omega n_d) \tag{3.12}$$

The new reference trace is the stack of the corrected daily traces (figure 3.31). I run this process multiple times to improve the final result. To verify the improvement of each iteration, I run the method 10 times and calculate the SNR of the corrected reference trace (figure 3.32), and the sum of the found time delay and fluctuations (figure 3.33). As can be seen from figure 3.33 and 3.32, the results stabilize after three iterations.

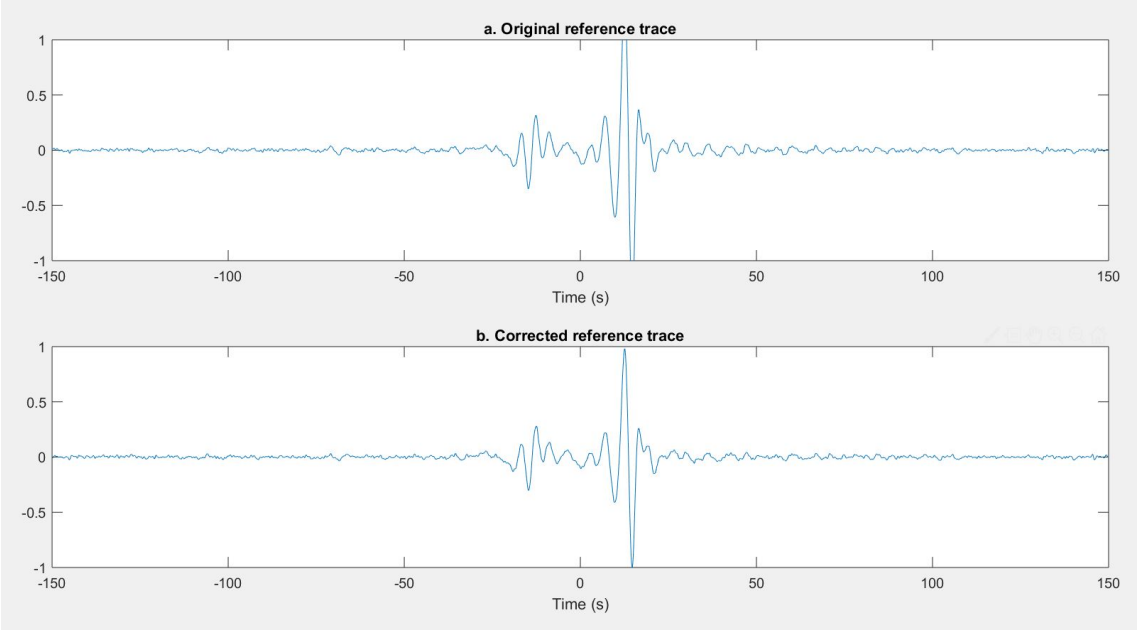

Figure 3.31: (a) the original reference trace, and (b) the corrected reference trace after 3 iterations.

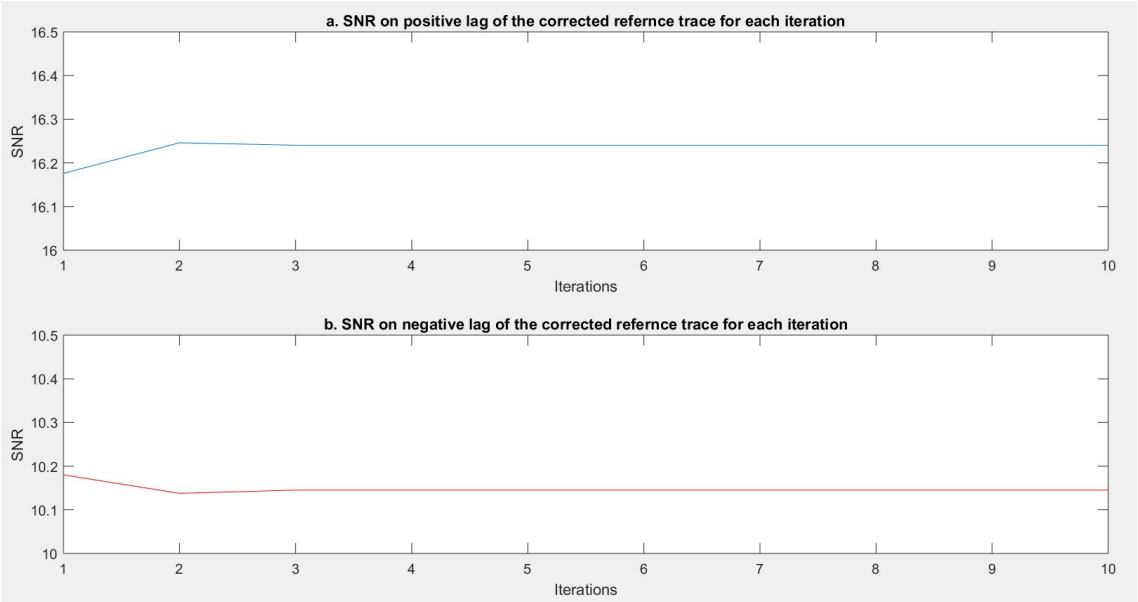

Figure 3.32: The signal to noise ratio (SNR) of the (a) positive lag and (b) negative lag of the corrected reference traces

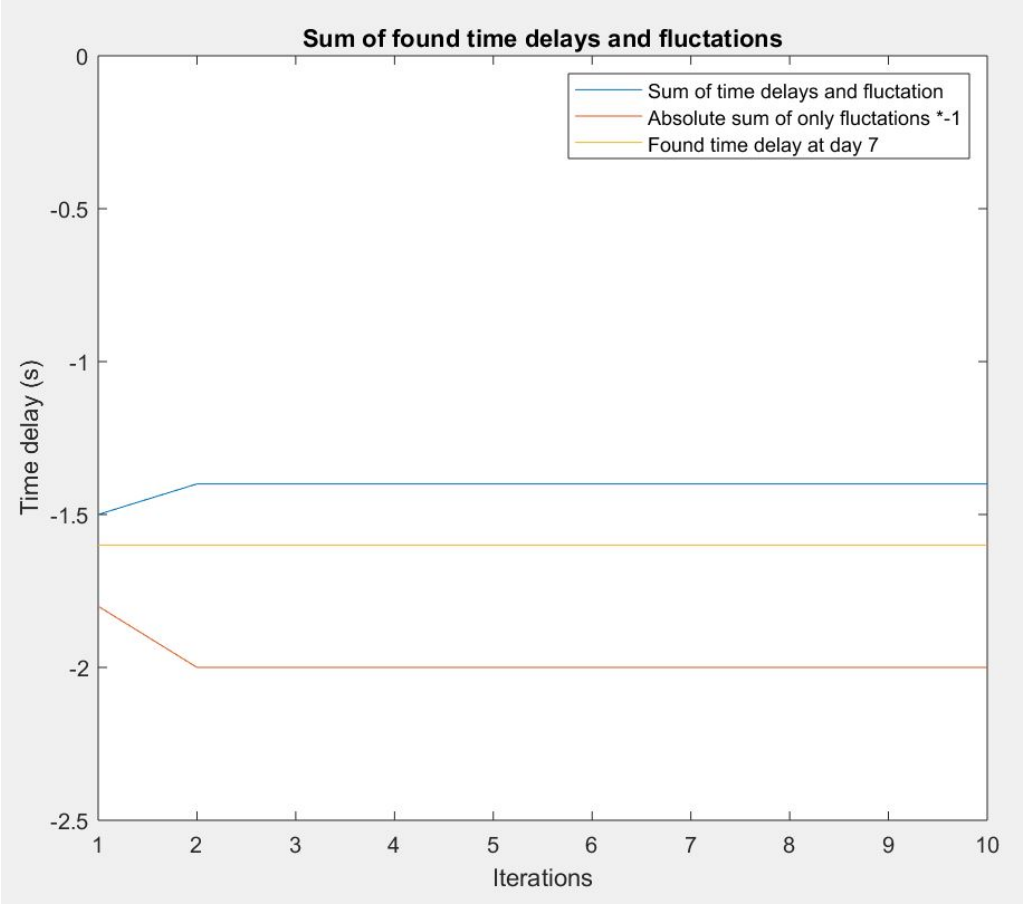

Figure 3.33: The sum of time delays and fluctuations (blue), the negative absolute sum of only the fluctuations (red), and the found applied time delay (yellow).

The found time delay is the relative time delay of the different station pairs. The final time delay of each station is estimated using inversion. The relation between the station pair time delays and the time delay of each individual station can be expressed in matrix form:

$$Gm = d$$

$$\begin{bmatrix} 1 & -1 & 0 & 0 \\ 1 & 0 & -1 & 0 \\ 1 & 0 & 0 & -1 \\ 0 & 1 & -1 & 0 \\ 0 & 1 & 0 & -1 \\ 0 & 0 & 1 & -1 \end{bmatrix} \begin{bmatrix} \Delta_A \\ \Delta_B \\ \Delta_C \\ \Delta_D \end{bmatrix} = \begin{bmatrix} \delta_{A-B} \\ \delta_{A-C} \\ \delta_{A-D} \\ \delta_{B-B} \\ \delta_{B-D} \\ \delta_{C-D} \end{bmatrix} \tag{3.13}$$

Where G represents the different combinations of station pairs, m represent the final

timing errors Δ_A of station A, and d represents the found timing error δ_{A-B} of the station pair A-B. The matrix is inverted to find the unknown final timing error m. Since the matrix G is not square, I use the generalized inverse G^{-g} for the inversion (Stein and Wysession, 2003):

$$m = G^{-g}d \tag{3.14}$$

I find the generalized inverse using the Matlab function *pinv*, which calculates the Moore-Penrose pseudoinverse of a matrix. G is a matrix of rank 3, meaning that a constant offset can be added to all stations without changing the time differences (Sens-Schönfelder, 2008). The found timing error Δ is therefore still relative, and the absolute time error can only be found after the stations are adjusted to a reliable network time.

I initially chose the station with the smallest absolute sum of time delays, as the station with the most reliable time, and tie the network time to this station by removing the station's time delay from all the stations' time delays. However, this is only possible if the measured time delays are accurate. If one or more of the station-pairs does not converge towards the Greens function, because of bad data recordings or uneven noise distribution, the measuring method is not able to measure the correct time delay and the time delay remains zero. This will affect the result of the inversion and an absolute time correction will add time delays to the bad station, instead of correcting shifts caused by the inversion.

Most seismic station networks do not have perfectly uniform noise distribution, including the NEONOR2 network which is situated along the Nordland coast and therefore has stronger noise sources coming from the ocean. A completely automatic measuring procedure is therefore not possible as the station with the most reliable clock must be chosen manually based on individual judgement. Sometimes it might even be better to avoid the inversion and rather derive which station the error occurred on, and the time and size of the error, by comparing the daily cross correlations and relative time delays found for all station pairs. An example where this is the case is shown in the Result chapter (figure 4.9).

3.4.1 Testing the method

The time delay measuring method is tested by applying a time delay using the Fourier transform and the shift theorem (equation 3.12). The shift is applied to data recorded by station NBB30 on November 7th, and cross correlated with stations NBB08, NBB05 and NBB28 for the entire test period, from November 1th 2014 to June 29th, 2015.

To check the sensitivity, I also test the method using different stack length for the reference trace and varying applied time delays.

The induced time shift is applied as a simple measure to check if time shifts are detected by the method. Since the time shift is applied as a single jump only affecting one day, this is a simplified version of a time error. Real instrumental errors are usually more complicated and likely to affect more days than the time shift example shown here.

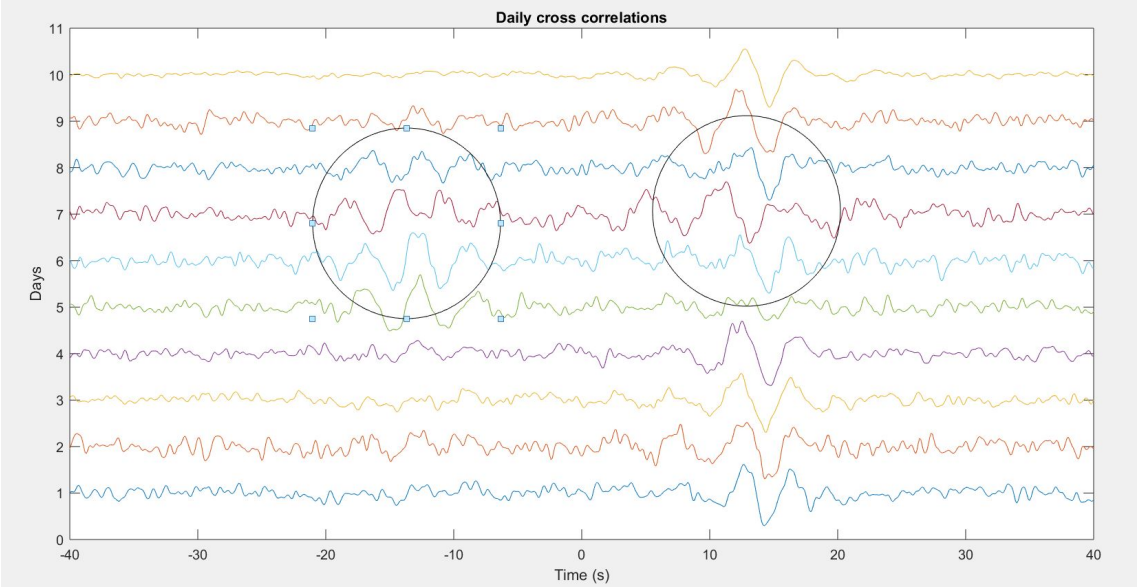

Figure 3.34: The daily cross correlations of data recorded on stations NBB30 and NBB28 between 4th and 9th of November. The time delay applied on NBB30 data from the 7th of November, can clearly be seen on the resulting cross correlation.

Figure 3.34 shows that the induced time delay has affected the resulting cross correlation. This is also clear from the cross correlation with the reference trace, as seen in figure 3.35, where the peak of the negative side correlation (figure 3.35(a)) is situated at about 1.6 s. The same goes for the peak of the positive side correlation (figure 3.35(b)), which is at -1.6 s. Note that 1 s equals 10 samples.

The found timing errors can be seen in the figures 3.36, 3.37 and 3.38. The method detects the applied time delay for all the station pairs involving NBB30 (figure 3.38). In addition to the applied time delay of 1.5 s on day 7, there are several fluctuations of up to 0.2 s. I assume that fluctuations this small have natural causes and are not caused by instrumental timing errors.

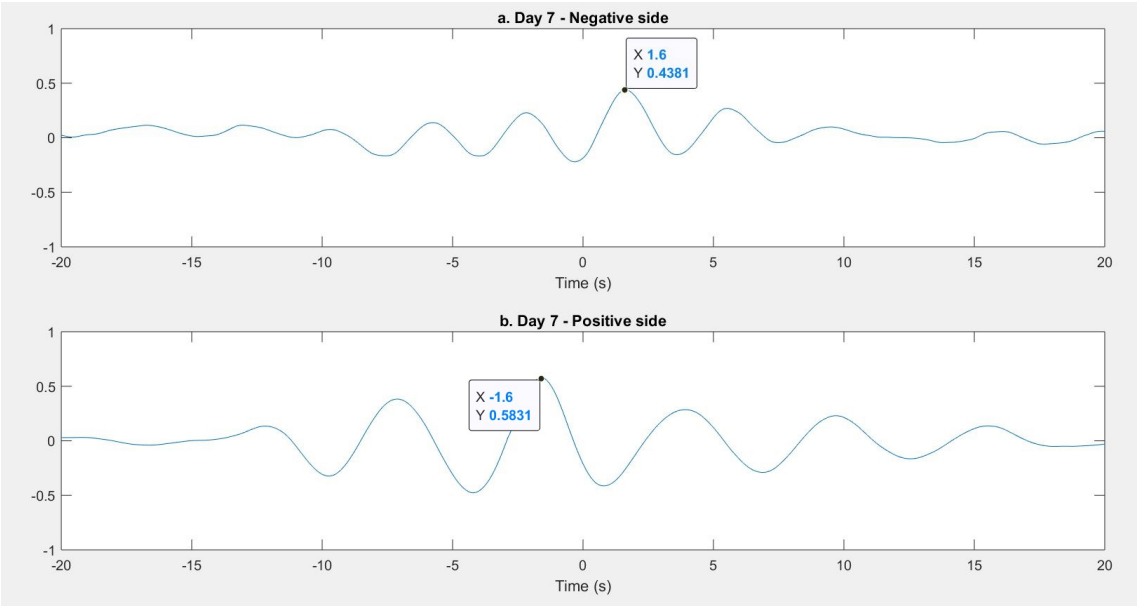

Figure 3.35: Cross correlation between the daily trace and the reference trace. The traces are separated into negative lag side (a), and positive lag side (b), prior to the cross correlation. The induced time delay can be seen as positive shift for the negative side and a negative shift for the positive side.

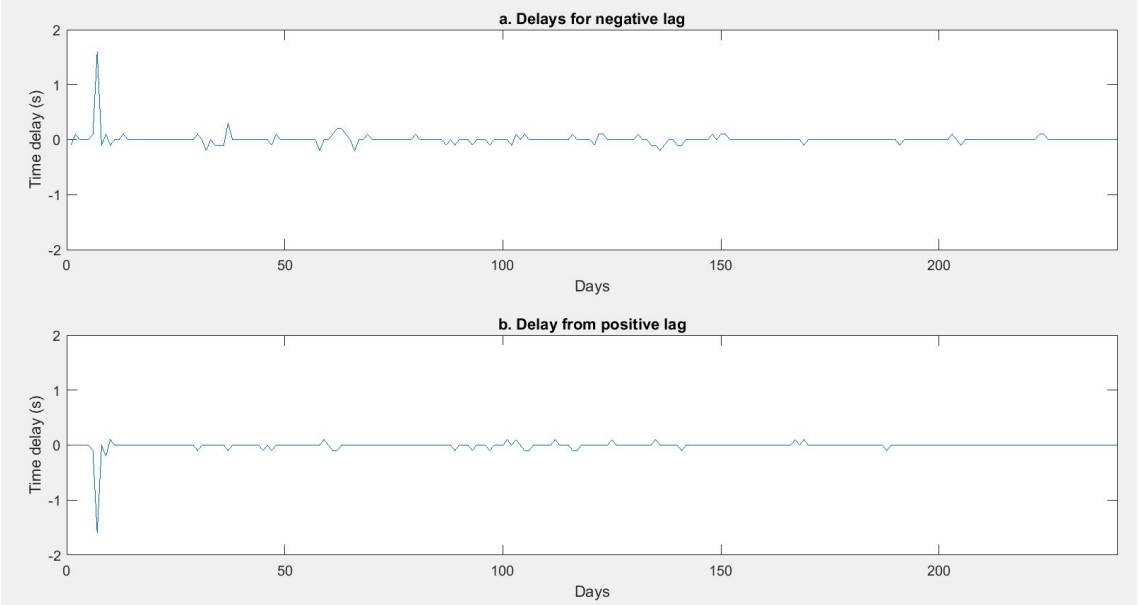

Figure 3.36: Relative time delays found from cross correlating (a) the negative lag side of the daily trace and reference trace, and (b) the positive lag side, using data recorded on NBB30 and NBB28 between 4th and 9th of November.

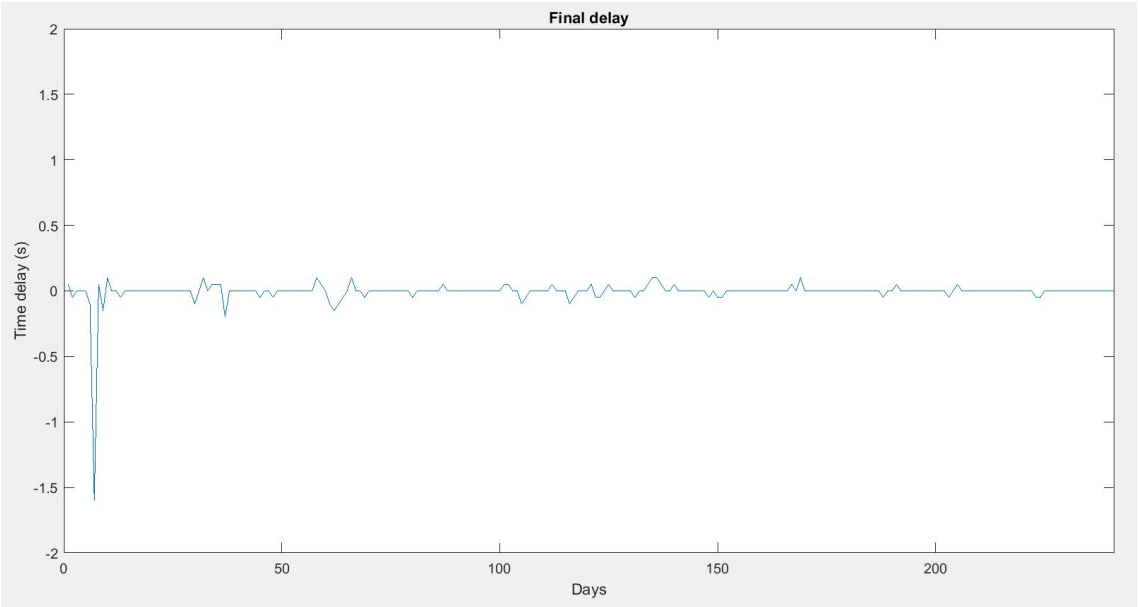

Figure 3.37: The final relative time delays found from averaging the time delays in figure 3.36.

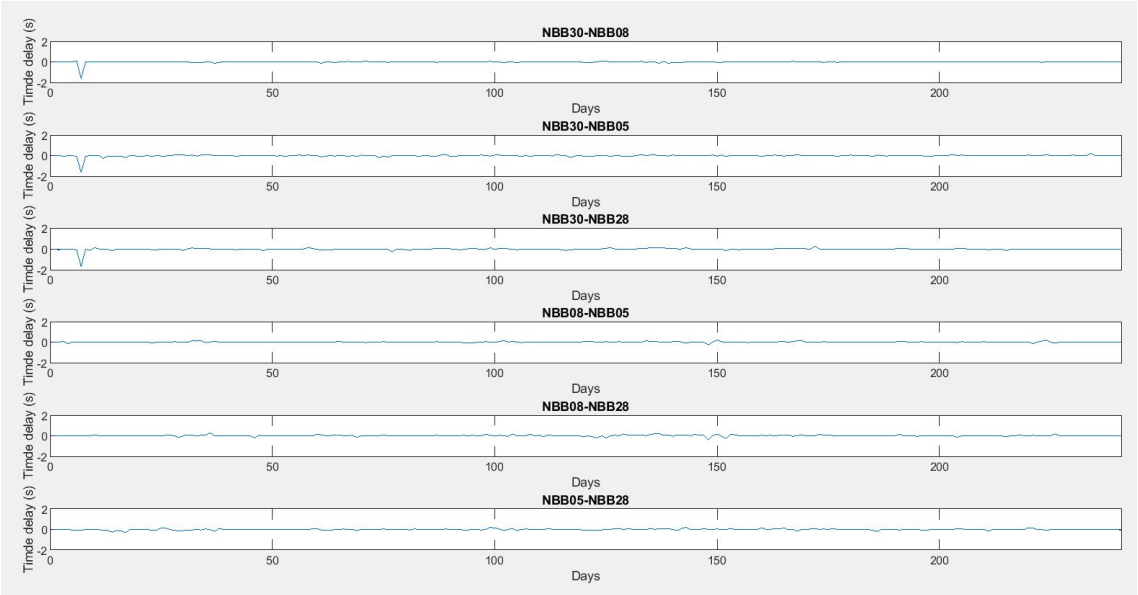

Figure 3.38: The final relative time delays for all the test station pairs. Time delays are found for all the station pairs involving NBB30

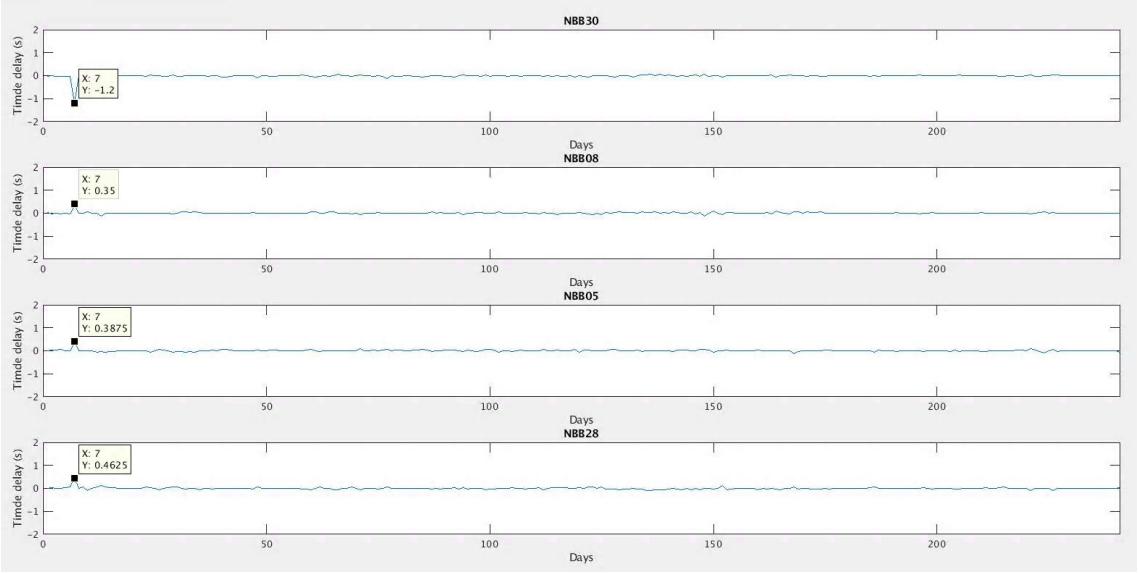

Figure 3.39: The relative time delays for all test stations found using inversion. The value of the largest delays for each station is indicated.

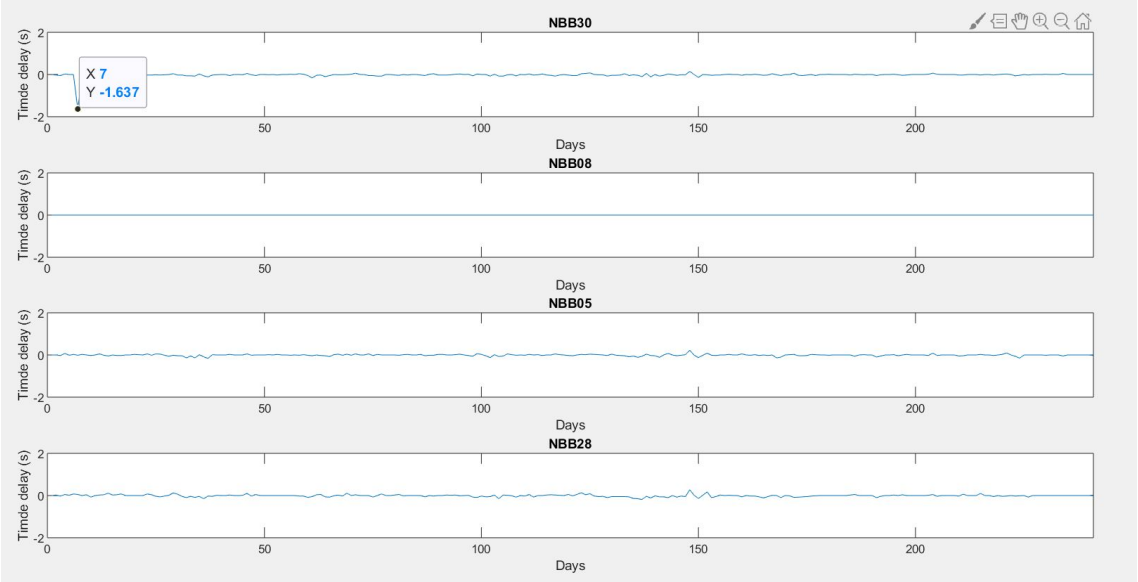

Figure 3.40: The absolute time delays for all test stations found using inversion and after correcting for absolute time. The value of the largest delays is indicated. Note that the absolute time correction sets all the time delays of station NBB08 to zero.

The result of the inversion in figure 3.39, shows a time delay of -1.2 s at day 7 of the test period (01.11.14-29.06.15) for station NBB30, and time delays between 0.35

s to 0.47 s are found on the same day for the other stations where there were no time delays applied. This is corrected for by finding the station with the smallest absolute sum of time delays, in this case NBB08, and tie the network time to this station. The result of the time correction, and the new absolute time delay can be seen in figure 3.40. The absolute time correction has set all the time delays of station NBB08 to zero, and a time delay of -1.637 s is found on day 7 only for station NBB30. The absolute time delay found is 0.137 s less that the applied time shift, which suggest a resolution of around 0.14 s. This is investigated further in the next section.

3.4.2 Resolution

I apply smaller time delays to test the sensitivity of the method. The applied time delays are found both for station pairs (figure 3.41) and for each station after inversion (figure 3.42 and 3.43). I find that applied time delays as small as 0.2 s are detected. However, since there are also natural fluctuations up to 0.2 s, it can be hard to distinguish between time errors and fluctuations this small. I therefore set the resolution limit to 0.2 s.

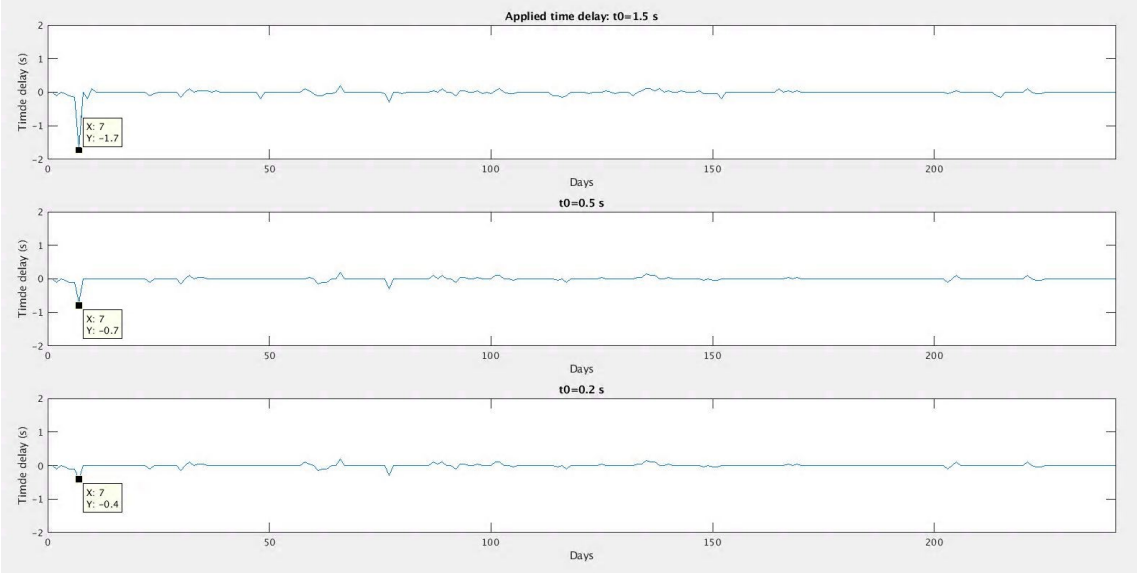

Figure 3.41: The final relative time delay found for station pair NBB30-NBB28, after applying a (a) 1.5 s, (b) 0.5 s and (c) 0.2 s time delay.

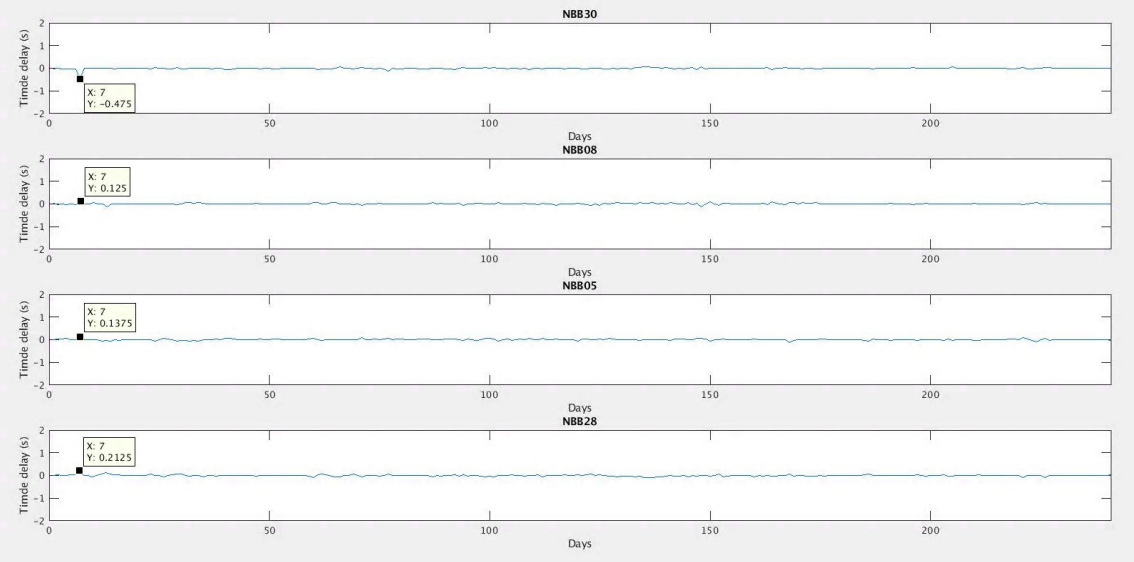

Figure 3.42: The applied time delay of 0.5 s on station NBB30 on day 7 is found using inversion. The absolute time has not been corrected for.

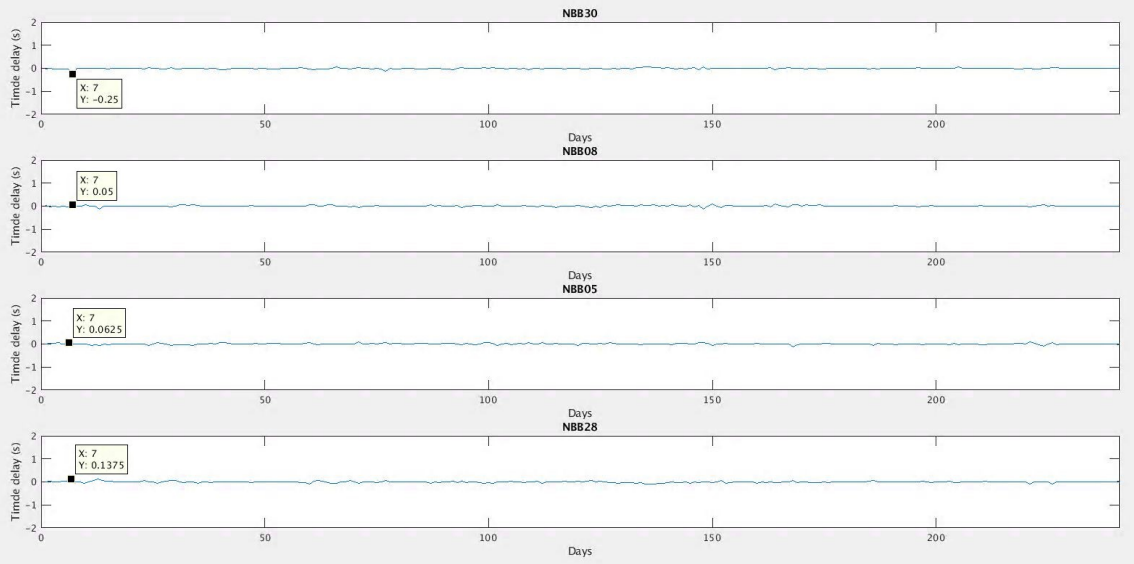

Figure 3.43: The applied time delay of 0.2 s on station NBB30 on day 7 is found using inversion. The absolute time has not been corrected for.

3.4.3 Reference trace

In the examples above I have used cross correlations stacked over the entire test period as reference. This is done to increase the SNR of the reference signal. However,

since seismic noise mostly comes from oceanic and atmospheric sources, the noise distribution varies with season. A noise correlation signal stacked over longer periods might therefore end up quite different to the daily noise correlations. I test the timing error measuring process using reference traces stacked over shorter periods, monthly and every 10 days, to check the effect seasonal and daily variations have on the final result.

Figure 3.44 shows the difference between reference traces stacked over the whole test period(figure 3.44a), each month (figure 3.44b) and 10 days (figure 3.44c). There are clearly both monthly and daily variations in the Green's function. However, when I measure the time delay using the different references, the results are mostly the same (figure 3.45). I therefore calculate the SNR of the reference traces (figure 3.46) and the sum of all the time delays and fluctuations (table 3.1), to investigate the differences of the results closer.

Table 3.1 shows that although the method using the reference trace stacked over the 10 last days, finds the correct applied time delay of 1.5 s, the absolute sum of all the fluctuations is larger than the reference traces stacked over longer period, this is also seen in figure 3.45. Figure 3.46 also shows that the reference trace stacked over the 10 last day gives the lowest SNR. The reference trace stacked over the whole period, on the other hand, gives both the highest SNR and the lowest absolute sum of fluctuations, indicating a more stable, though not exact, result. The reference trace stacked monthly gives similar results to the reference stacked over the whole period, indicating that seasonal variations does not have significant effect on the final results of the measuring method.

However, as mentioned in the start of this section, the induced time shift is only a simplified version of a time error. A realistic instrumental time error might shift the Green's function over time and affect the reference traces stacked over varying period length differently. This will be investigated further in the result chapter.

Table 3.1: The sum of all the found time delays and fluctuations

Sum	**Whole period**	**Every month**	**10 last days**
The found time delay	-1.6 s	-1.6 s	-1.5 s
Absolute sum of fluctuations (without the time delay)	2.0 s	2.25 s	2.8 s
Sum of all time delays and fluctuations	-1.4 s	-1.25 s	-1.1 s

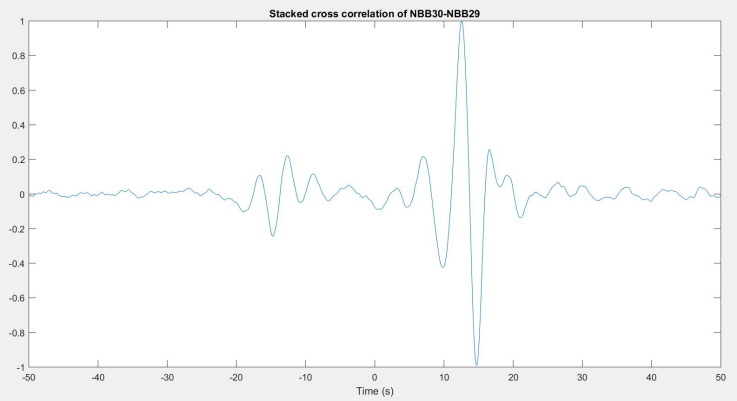

(a)

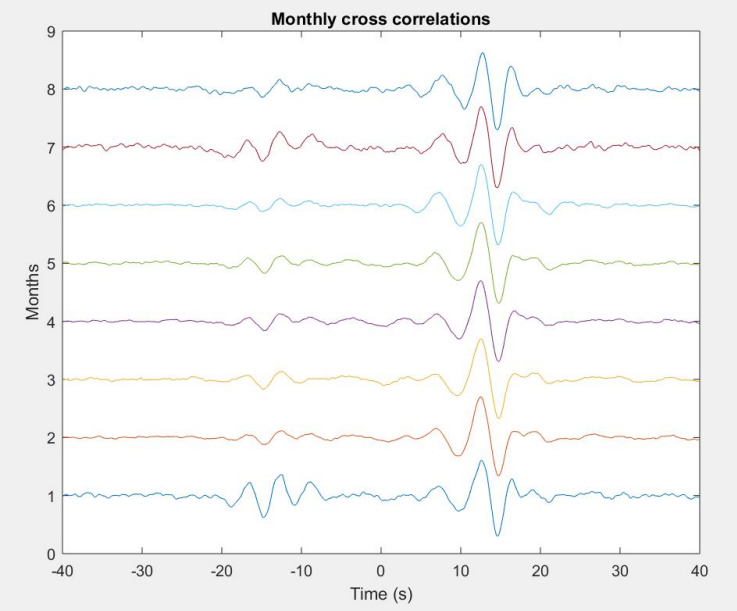

(b)

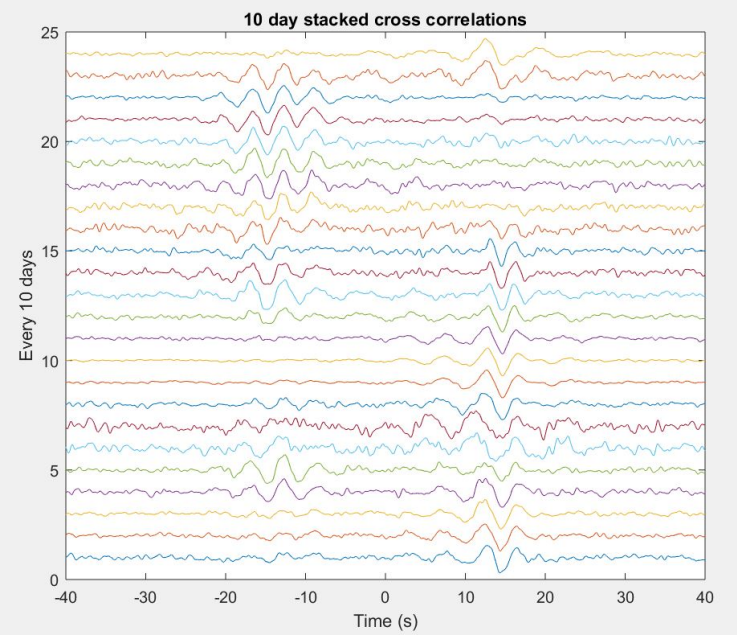

(c)

Figure 3.44: The reference traces stacked over (a) the whole period, (b) monthly and (c) the last 10 days.

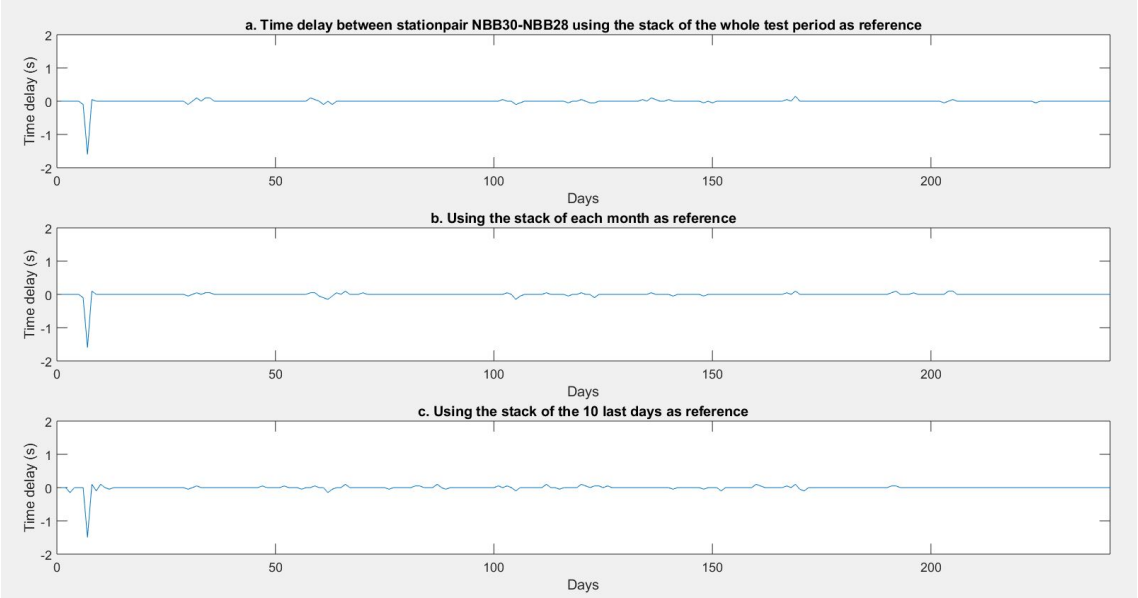

Figure 3.45: The relative time delay for station pair NBB30-NBB28, found after applying a 1.5 s time delay to station NBB30 on data recorded on the 7th of November. The time delay is found using (a) the stack of the whole test period (01.11.14-29.06.15) as reference, (b) the stack of each month as reference and (c) the stack of the last 10 days as reference.

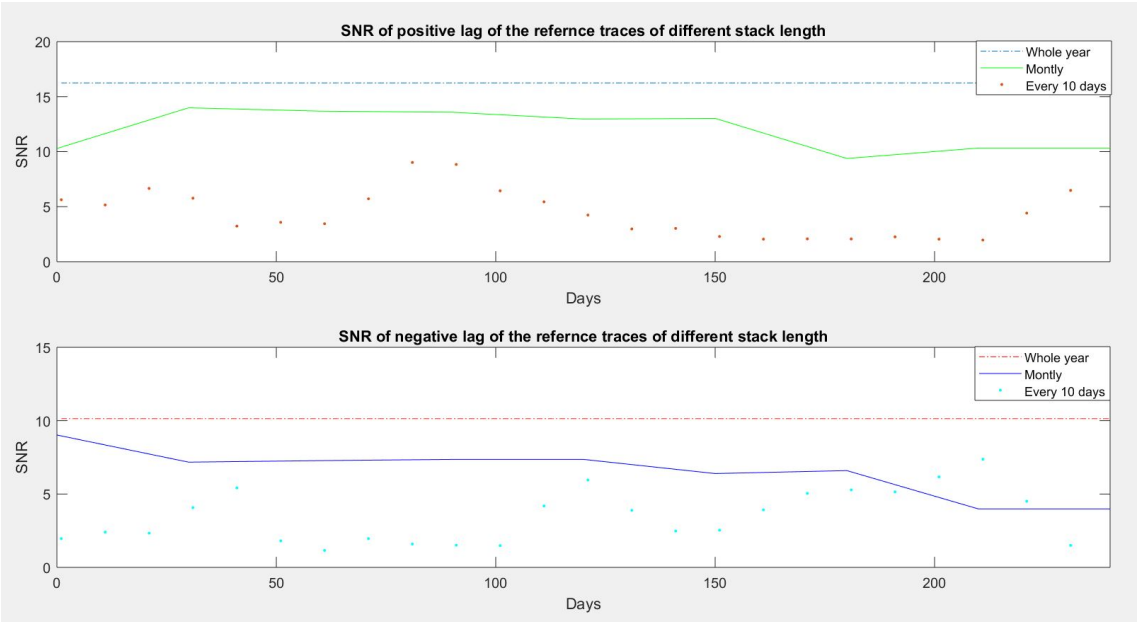

Figure 3.46: The signal to noise ratio (SNR) of the (a) positive lag and (b) negative lag of the different reference traces.

3.4.4 Asymmetric signals

As explained in the beginning of this section, the causal and acausal part of the signal is separated prior to measuring time delays. This is done to ensure quality measurements and to differentiate between shift occurring only on one side and shifts caused on both causal and causal side. However, this means that completely asymmetric signals cannot be used for measuring time delays. One sided signals, noise correlations where the Green's function is only estimated on one side, usually comes from cross correlating strongly directional noise. One example of a one-sided signal is the cross correlation of noise recorded on stations NBB30 and NBB29 (figure 3.47b.).

To deal with these issues I test the method without separating the causal and acausal part of the signal. The time delays are thus measured as one shift over the entire signal, the rest of the measuring process is as described above. To ensure quality measurements, I only use signals with correlation coefficient above 0.6. To test the method, I apply a time shift of 1.5 s to the 9th of November 2014 on station NBB30, as described above.

The result of the measuring method without separating the causal and acausal part of the signal, can be seen in figure 3.47b. The induced time shift on day 9 is detected, but so is larger time shift up to 10 s on other days. Not all of these large shift are observed in the daily cross correlations, and thus not likely to be real instrumental timing errors. This shows that measuring time delays over the entire signal can be done, but should be treated with caution because of the large uncertainty of only measuring the shift of one side.

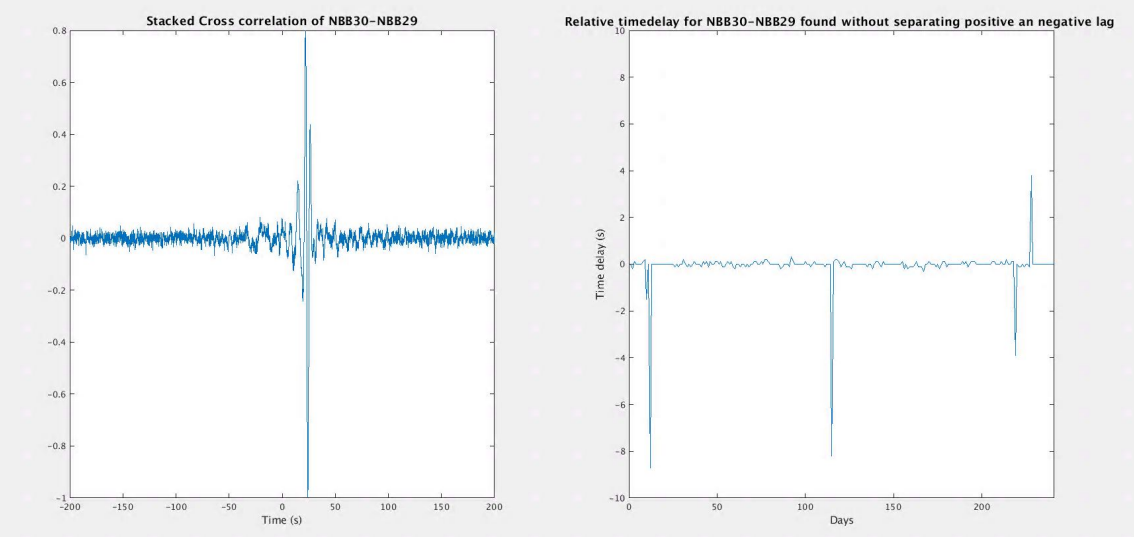

Figure 3.47: (a) The noise correlation of station pair NBB30-NBB29 show a one-sided signal. (b) The time delays of station pair NBB30-NBB29 are measured over the entire signal, without separating the causal and acausal side.

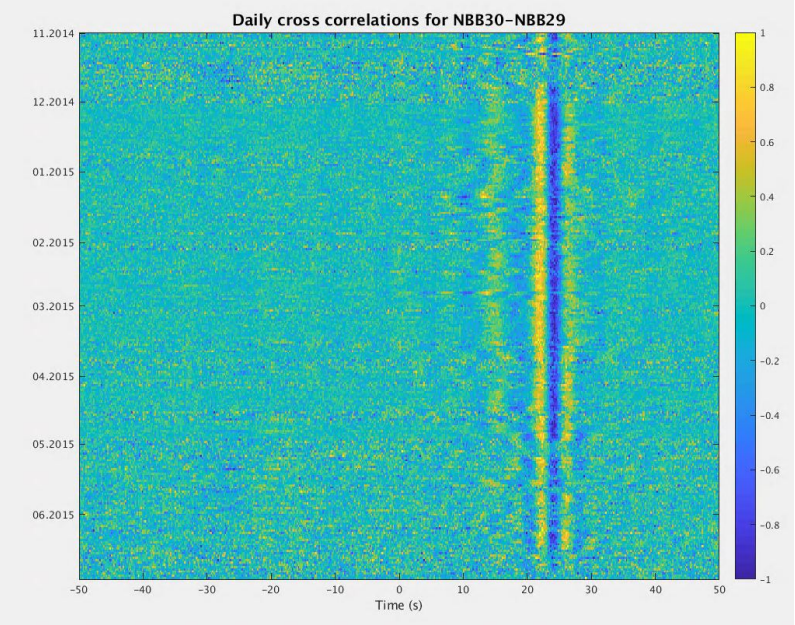

Figure 3.48: The daily noise correlation of station pair NBB30-NBB29.

Measuring time delays on the causal and acausal side of the signal separately, also becomes a problem when dealing with time shift so large that the signal is entirely

shifted from one side to the other. An example of this will be discussed in the result chapter (figure 4.5).

3.4.5 Frequency bands

Most of the cross correlations used to find time delays in the examples above, were first bandpass filtered between [0.14-0.5] Hz. I chose this frequency band because it gave the waveform with the highest SNR when testing different bandpass filters (figure 3.11). To see at what frequencies the time delays can measured, I also apply the measuring method on cross correlations filtered over different bandpass filters.

Figure 3.49 shows that the induced time delay of -1.5 s is detected by waveforms between 1-10 s period (figure 3.49c-h).

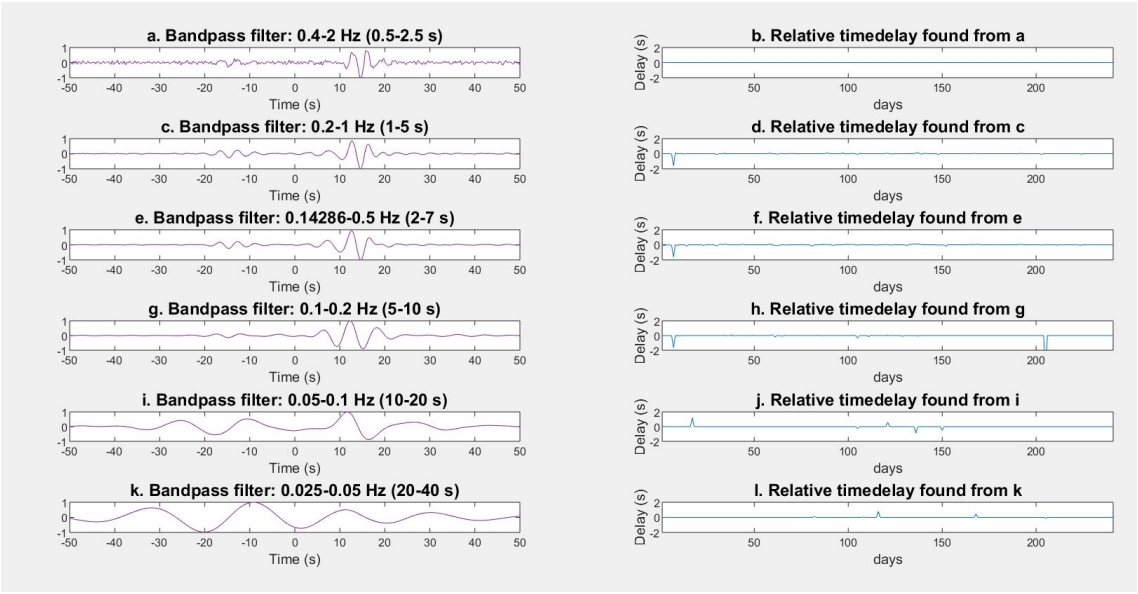

Figure 3.49: (a,c,e,g,i,k) The noise correlations bandpass filtered over different indicated narrowband filters (b,d,f,h,j,l), and the time delays measured from the a,c,e,g,i,k.

3.5 Synthetic surface wave

The estimated Green's function can be further used to investigate the Earth structure. This is done by measuring the dispersion of the surface wave Green's function, which in turn is inverted to determine the velocity. While this is not within the scope of this thesis, I create synthetic surface waves to compare with my estimated Green's function and see if they show similar dispersive character.

I model the synthetic surface wave using functions from the Bob Herrmann's package

(Herrmann, 2013). In the program I use the distance between the source and receiver, which in this case is the distance between the two test stations NBB30 and NBB28, and a standard 7-layer velocity model for Norway (Bungum and Havskov, 1986). The program uses these inputs to create eigenfunctions for surface waves, which together with a focal mechanism and a source pulse, are further used to model a three component seismogram (figure 3.51). The seismogram is displayed as ground displacement.

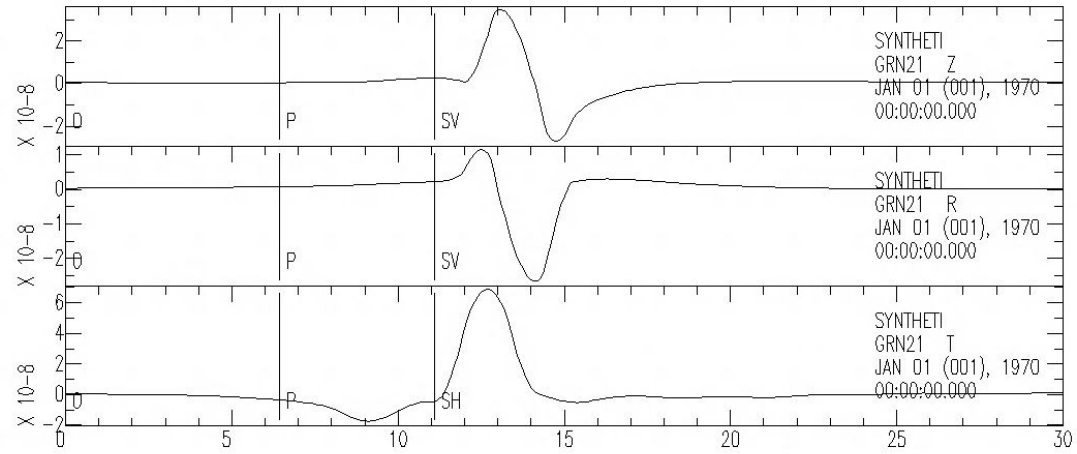

Figure 3.50: The three component synthetic seismogram modelled using the Bob Herrmann's package (Herrmann, 2013).

To compare the dispersion of the synthetic surface wave with my estimated Green's function, I apply the same narrowband filters to the vertical component of the synthetic seismogram (top component in figure 3.50) and the noise correlation of station pair NBB30-NBB28. The results show that the synthetic and found surface wave are quite similar, especially at long periods (figure 3.51). The velocity model used is the standard for all of Norway and is not necessarily correct for the North of Norway where the NEONOR2 stations were deployed. The modelled synthetic surface wave is therefore not expected to look exactly the same as the found Green's function. The found similarities, especially at long periods, are thus satisfactory.

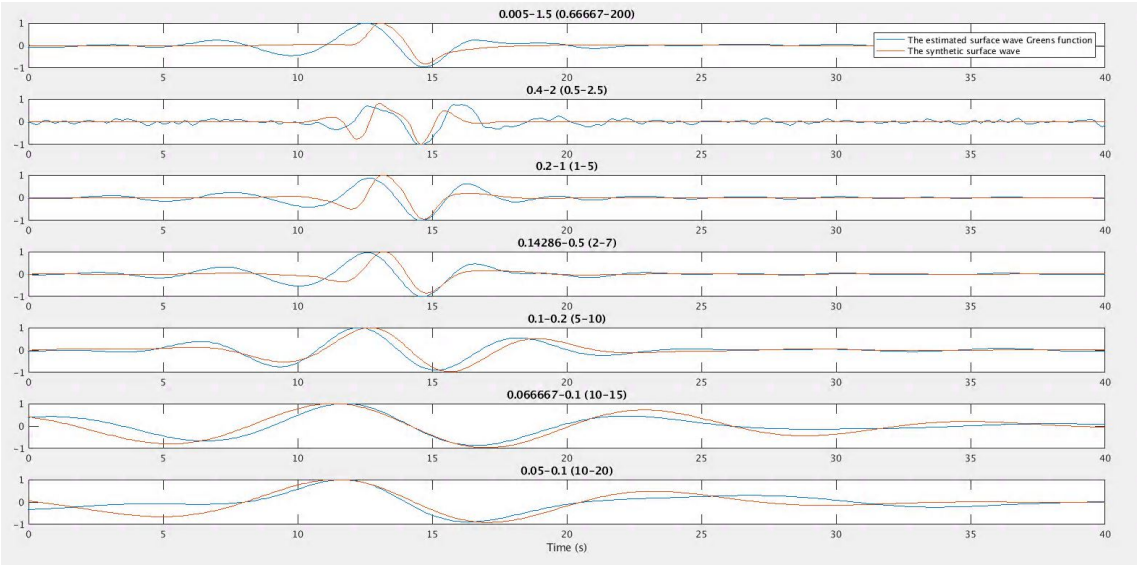

Figure 3.51: The synthetic surface wave bandpass filtered over the frequency bands indicated.

3.6 Noise distribution

I investigate the noise distribution of the study area by examining the waveforms of the final stacked noise correlations as a function of azimuth and distance.

I calculate the distance Δ and azimuth ζ using the coordinates $[\theta, \phi]$ of the stations (figure 2.9 and 2.10), following the formulas:

$$\Delta = \cos^{-1}[\cos(90-\theta_1)\cos(90-\theta_2) + \sin(90-\theta_1)\sin(90-\theta_2)\cos(\phi_2-\phi_1))] \quad (3.15)$$

$$\zeta = \sin^{-1}[\frac{1}{\sin\Delta}(\sin(90-\theta_2)\sin(\phi_2-\phi_1))] \quad (3.16)$$

Where θ_1 and θ_2 are the latitude of station 1 and station 2, respectively, and ϕ_1 and ϕ_2 are the longitude (Stein and Wysession, 2003).

I then calculate the ratio of the maximum absolute amplitude of the causal and acausal part of the noise correlation and plot the ratios as a function of location (figure 4.27), and the azimuths as a function of distance (figure 4.27). This is shown in the result chapter.

Chapter 4

Results

4.1 The Green's function

Cross correlations of ambient seismic noise recorded on NEONOR2 stations show the estimated surface wave Green's function. This is clear from how the waveform travels with distance(figure 4.1) and at different frequencies (figure 4.2). In addition, a synthetic surface wave is modelled to compare with the estimated Green's function (figure 4.3).

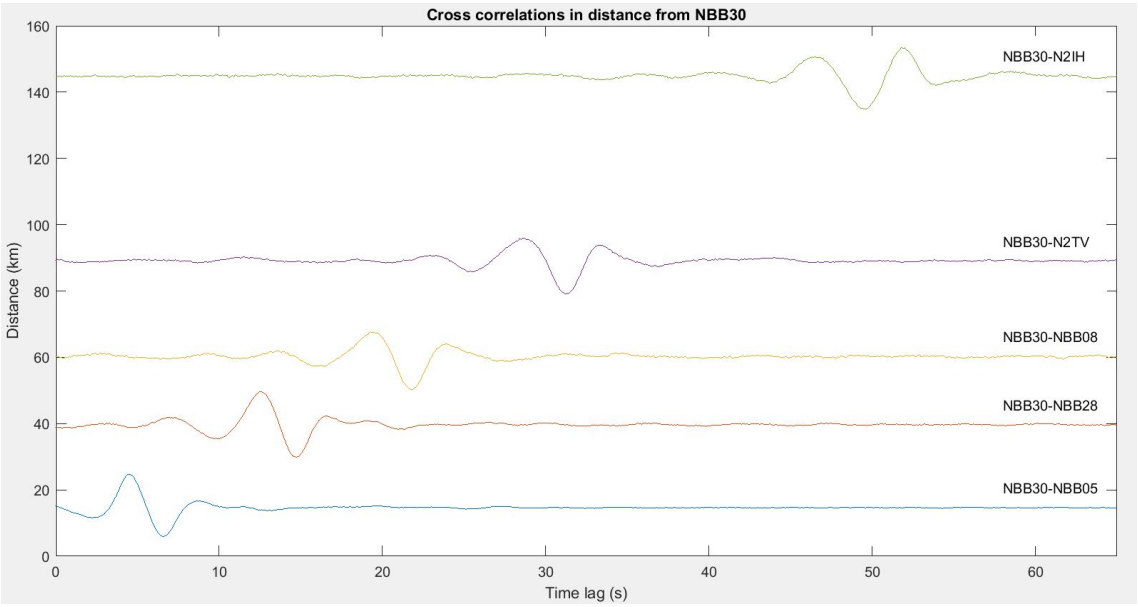

Figure 4.1: Causal part of the bandpass filtered cross correlation in figure 3.11, with the dispersion indicated.

The Green's function is the waveform travelling between two stations. This is demonstrated by cross correlating seismic noise recorded on station NBB30 with noise recorded on stations with increasing distance from NBB30. Figure 4.1 shows that the higher the distance between the stations, the later the Green's function arrives. This demonstrates that the estimated Green's function equals a travelling surface wave. The velocity of the waveform is roughly estimated as 3 km/s, which is consistent with the velocity of Rayleigh waves.

Surface waves between 1-20 s period are estimated from cross correlated noise recorded at NEONOR2 stations. Surface waves are dispersive, meaning that the velocity varies with frequency (Stein and Wysession, 2003). The dispersive character of the estimated Green's function is shown in figure 4.2. The long period parts of the signal sample deeper structures in the Earth with higher velocities, and therefore arrive earlier than the short period parts of the signal.

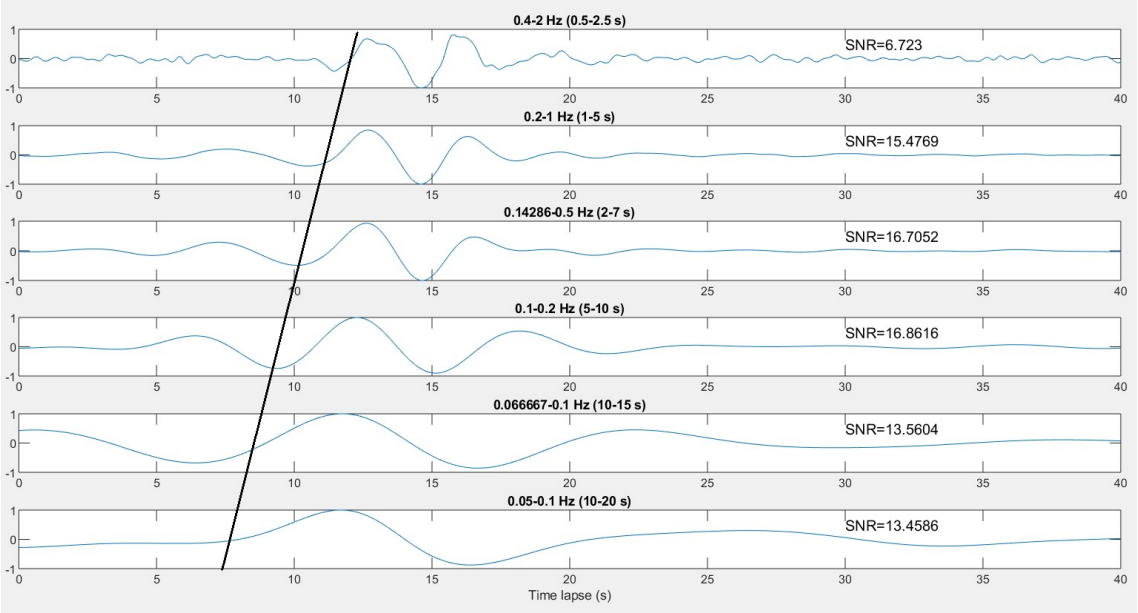

Figure 4.2: Causal part of the bandpass filtered cross correlation in figure 3.11, with the dispersion indicated.

The modelled synthetic surface wave and the estimated Green's function are fairly similar at all frequencies, especially at longer periods (figure 4.3) This also shows that the noise correlations are the estimated surface wave Green's function between two stations.

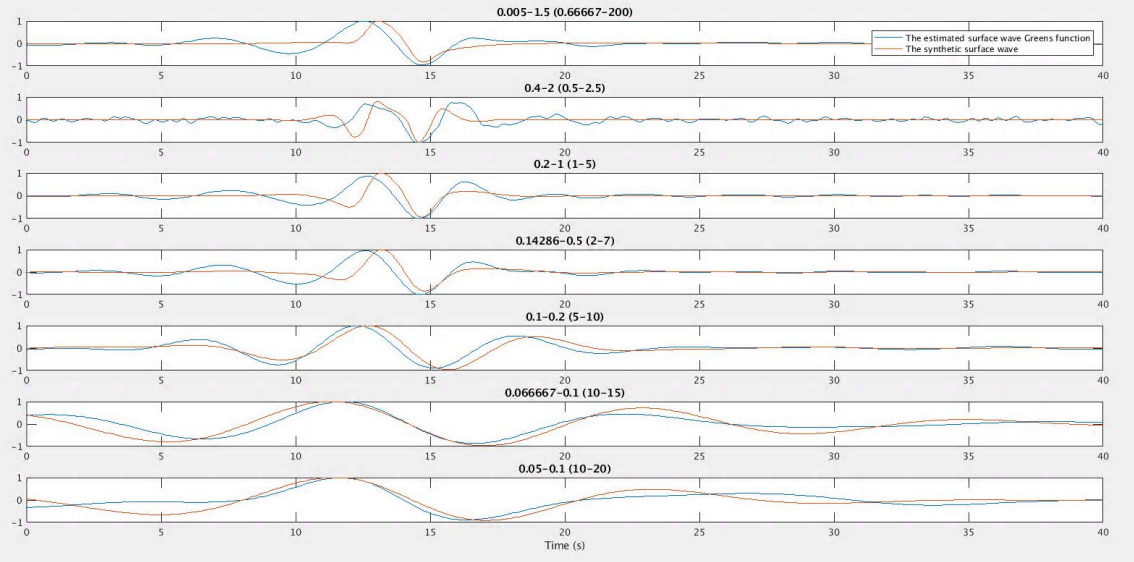

Figure 4.3: The synthetic surface wave bandpass filtered over the frequency bands indicated.

4.2 Timing errors

Each of the NEONOR2 stations is cross correlated with at least three other NEONOR2 stations. The exception is station N2VG which was deployed late in the project and therefore recorded little data. The stations are organized in groups of four, creating 6 station pairs per group, following matrix G in equation 3.13. After the first run, the station combinations are reorganized to see how the combinations affect the final result. The station combinations are given in figure 4.4.

Timing errors for station NBB15, NBB40 and NBB29 are found. This becomes clear when comparing the noise correlations and the found timing errors for stations pairs involving these stations. In addition, stations N2RO and N2VA showed some issues, though not necessarily with timing.

	Station 1	Station 2	Station 3	Station 4
1.	N2AN	N2BR	N2DI	N2HA
2.	N2BR	N2DI	N2HA	
3.	N2DI	N2HA		
4.	N2HA			
5.	N2HS	N2IH	N2LO	N2NF
6.	N2IH	N2LO	N2NF	
7.	N2LO	N2NF		
8.	N2NF			
9.	N2RO	N2SO	N2ST	N2SV
10.	N2SO	N2ST	N2SV	
11.	N2ST	N2SV		
12.	N2SV			
13.	N2TV	N2VA	NBB15	N2VI
14.	N2VA	NBB15	N2VI	
15.	NBB15	N2VI		
16.	N2VI			
17.	NBB03	NBB05	NBB08	NBB12
18.	NBB05	NBB08	NBB12	
19.	NBB08	NBB12		
20.	NBB12			
21.	NBB13	NBB14	NBB15	NBB17
22.	NBB14	NBB15	NBB17	
23.	NBB15	NBB17		
24.	NBB17			
25.	NBB28	NBB29	NBB30	NBB40
26.	NBB29	NBB30	NBB40	
27.	NBB30	NBB40		

(a)

	Station 1	Station 2	Station 3	Station 4
9	N2RO	N2VA	N2DI	NBB12
14	N2VA	N2DI	NBB12	
3	N2DI	NBB12		
20	NBB12			
23	NBB15	N2ST	NBB03	N2TV
17	N2ST	NBB03	N2TV	
11	NBB03	N2TV		
13	N2TV			
11	N2ST	NBB14	NBB17	NBB29
22	NBB14	NBB17	NBB29	
24	NBB17	NBB29		
26	NBB29			
27	NBB30	NBB40	NBB08	N2TV
28	NBB40	NBB08	N2TV	
19	NBB08	N2TV		
13	N2TV			
23	NBB15	NBB28	N2ST	N2TV
25	NBB28	N2ST	N2TV	
11	N2ST	N2TV		
13	N2TV			

(b)

Figure 4.4

4.2.1 NBB15

Timing errors are clearly seen when comparing the daily cross correlations of station pairs involving NBB15 in figure 4.5 and 4.6.

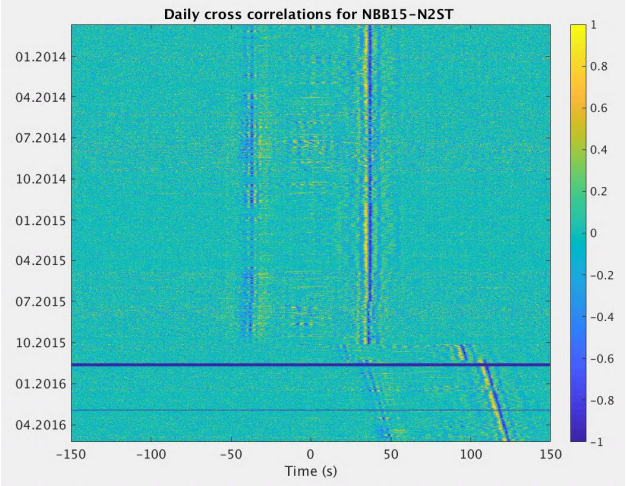

(a)

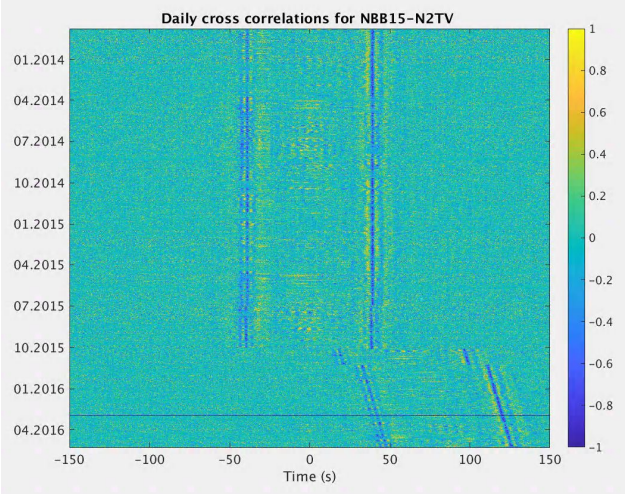

(b)

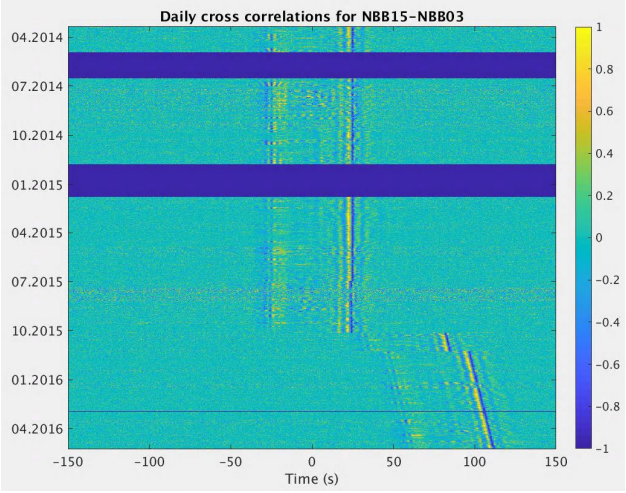

(c)

Figure 4.5: The daily noise correlations found for the stations NBB15 and N2ST plotted over the entire period.

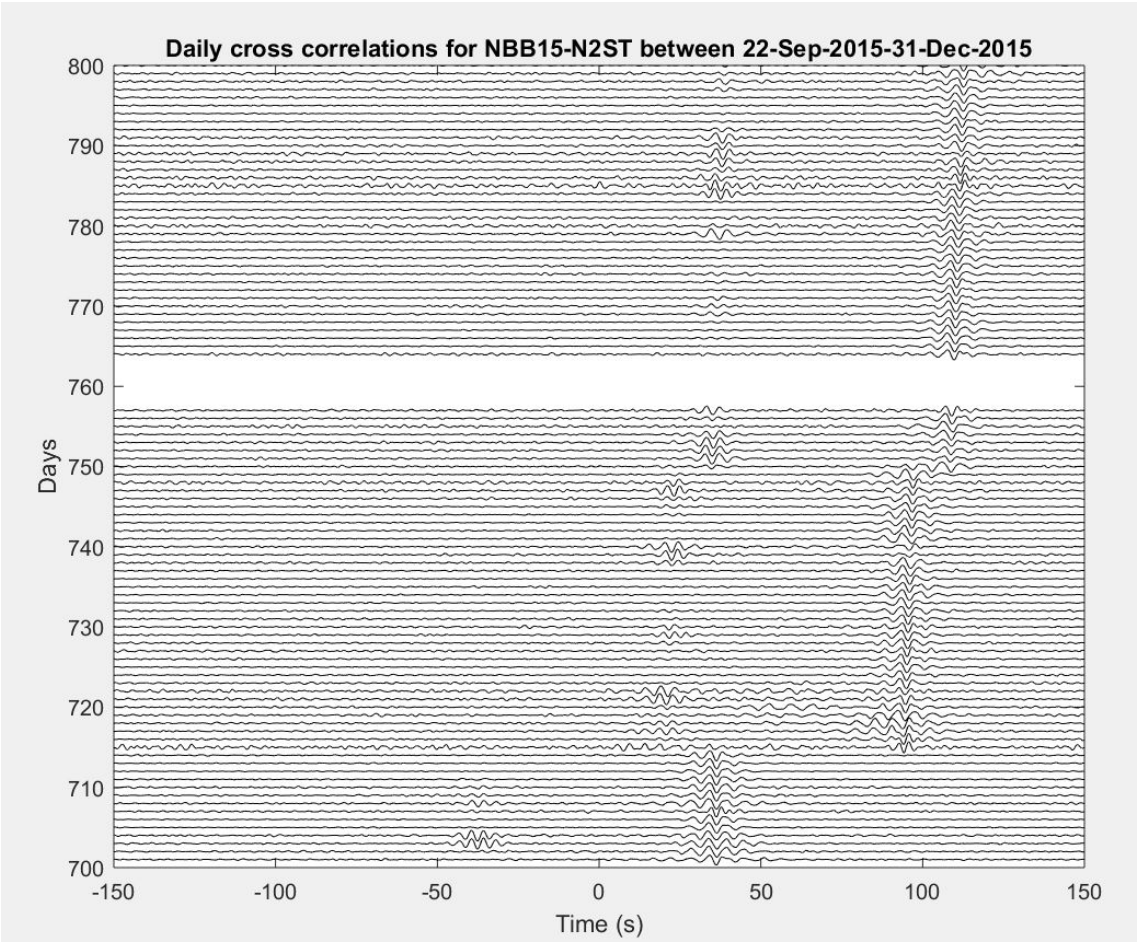

Figure 4.6: The noise correlations and relative time delays found for station pairs NBB15-N2ST between 22th of September until 31th of December 2015.The signal jump about 50 s on day 715 (5th of October) and 10 s on day 755 (11th of November 2015). The signal drifts linearly with about 0.1 s/day from the first jump until the end of recording (day 920).

Figure 4.5 and 4.6 show that the Green's function is shifted with almost 100 s from around October 2015. The signal starts to shift with a few seconds around 21th of July 2015 and then make two time jump of about 50 s on 5th of October and 10 s on 11th of November 2015. From the first jump in the beginning of October, the signal drifts linearly with about 0.1 s/day.

When comparing these dates with the GPS logs of NBB15, it shows that the GPS did not manage to record (lock) the time after a disconnection on the 5th of October. This is consistent with the jump and drift seen in figure 4.5.

However, only the smaller time delays in July 2015 are detected when applying the

measuring method to the cross correlations. In figure 4.7, when station NBB15 is cross correlated with stations NBB13, NBB14 and NBB17, time delays up to about 1 second are found for the days 638 until 731, the 21st of July until the 22nd of October 2015. Similar time delays are found when station NBB15 is cross correlated with stations NBB28, N2ST and N2TV (figure 4.8). The relative time delays for the station pairs are all zero after day 731, this indicates that the timing was either perfect or that the daily noise correlations after this date were too poor to be used for measurement. The latter is more likely, seeing the large time shifts in the daily cross correlations in figure 4.5.

The noise correlations in figure 4.7 show that station NBB15 is located very close to both NBB13 and NBB17, this might also have affected the found time delays. However, the fact that similar time delays were found for different station combinations, indicates that the measurements are otherwise reliable.

When inverting to find the time delays of each station and correcting to set the absolute time, time delays up to - 0.55 s are found between the days 638-730, 21th of July until 21th of October 2015 (figure 4.9). However, the accuracy of the inversion depends on the measured time delays of all the station pairs, meaning that if only one station pair gives inaccurate measurements, this will affect the result of the inversion. In this example, the noise correlation of station-pair NBB28-N2ST is one-sided and the measuring method has thus not been able to detect time delays (figure 4.8 fourth line from the top). The inverted timing errors for each station in figure 4.9 is therefore not necessarily accurate.

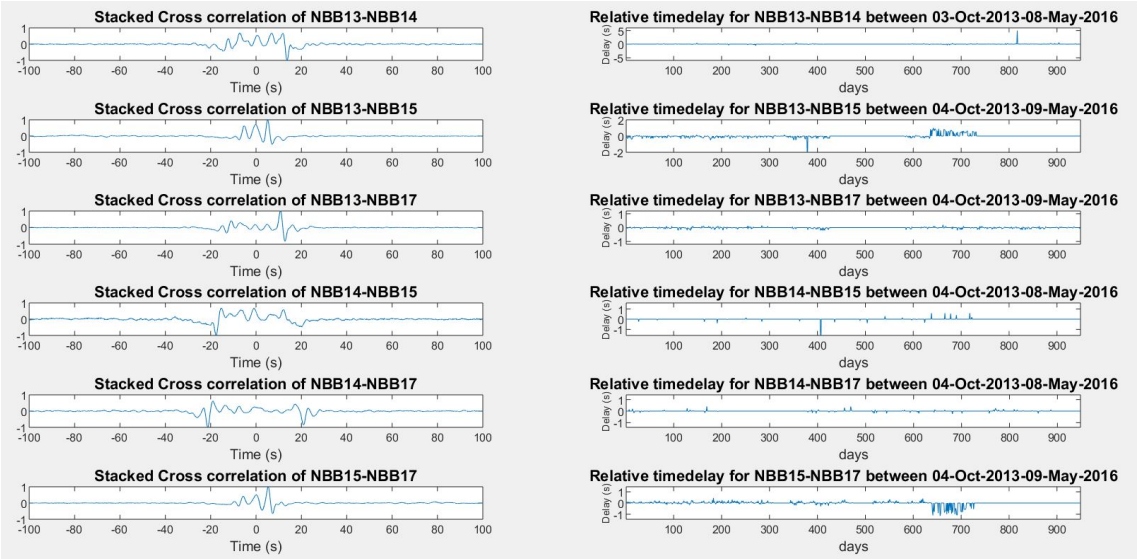

Figure 4.7: The noise correlations and relative time delays found for station pairs involving the station NBB15.

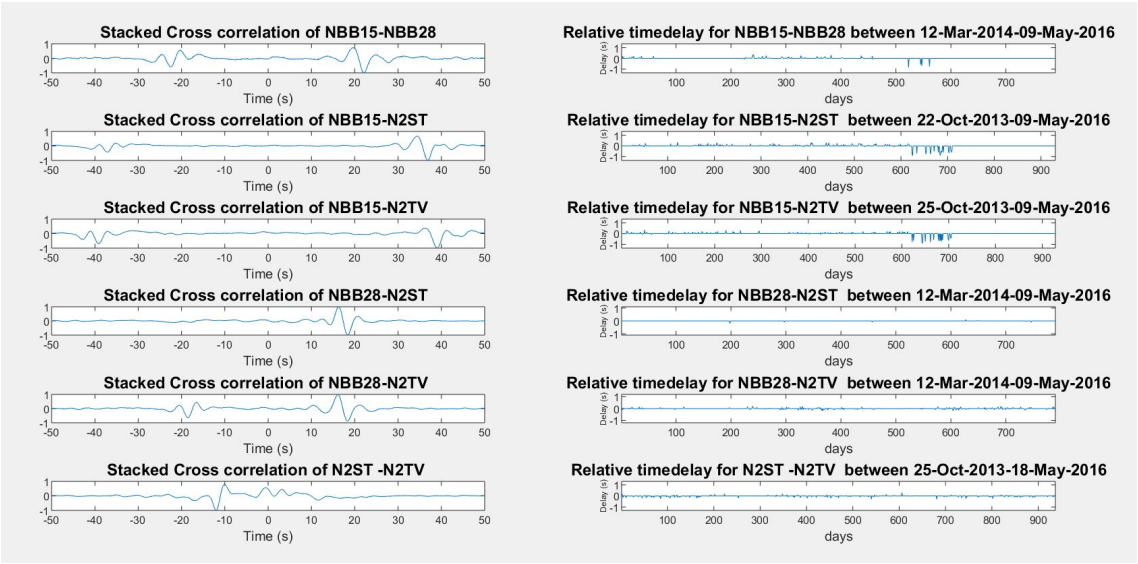

Figure 4.8: The noise correlations and relative time delays found for station pairs involving the station NBB15.

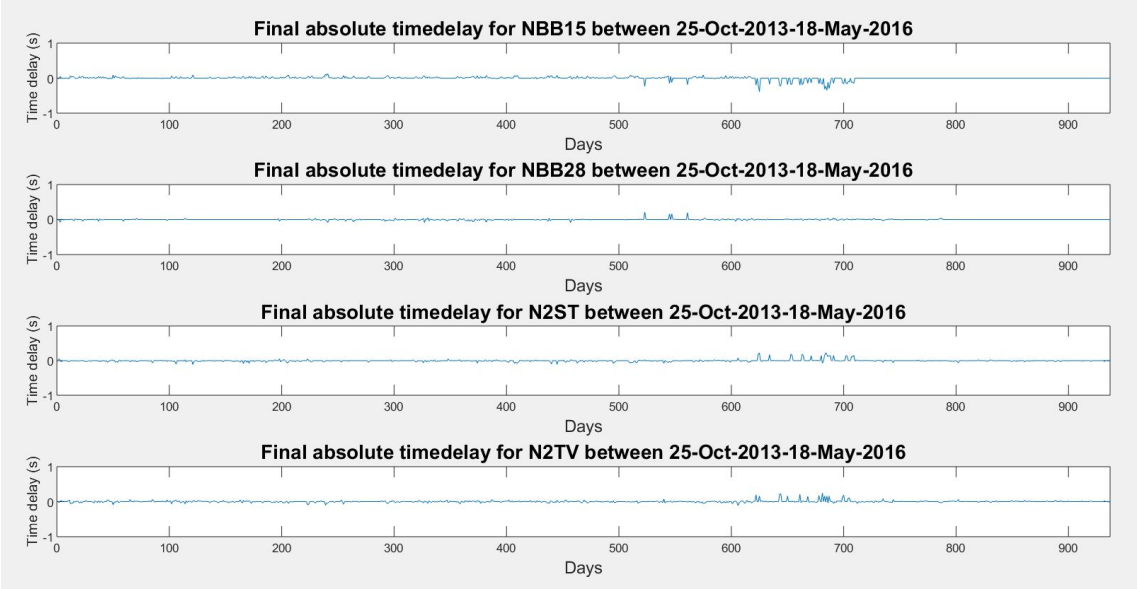

(a)

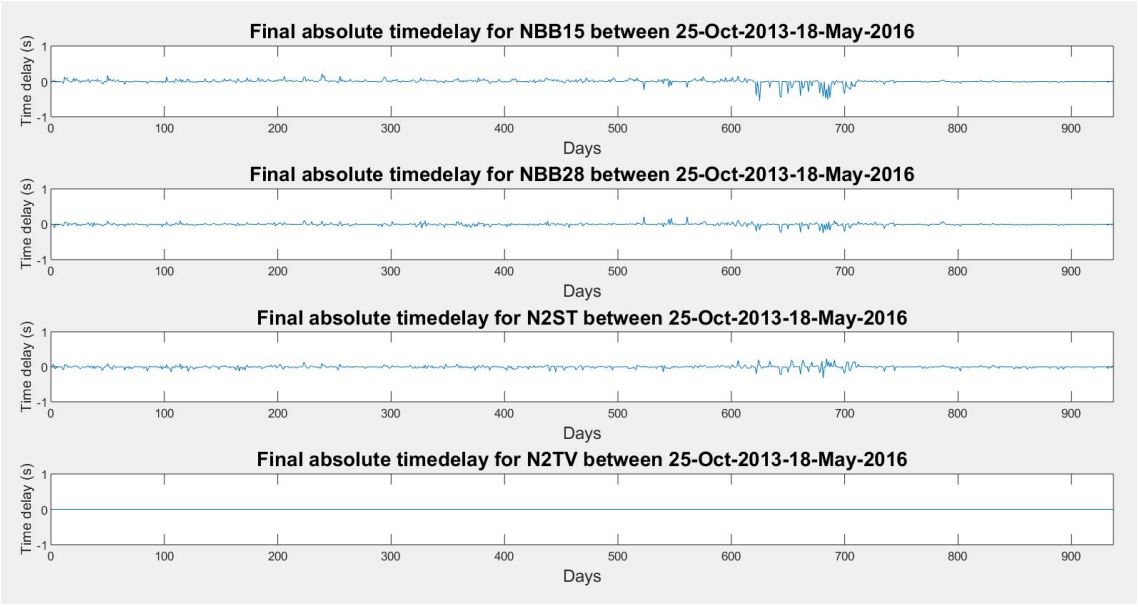

(b)

Figure 4.9: The time delays found for each station. (a) before and (b) after absolute time correction.

The time delays shown above were found using a reference trace stacked over the entire period the stations were active. The noise correlations used were bandpass filtered over 0.01-1.25 Hz and spectral whitening applied after onebit normalization in the pre-processing process. The cross correlation were done over daily (figure 4.7)

or 6 hours long time windows (figure 4.8). To test the effect these variables have on the final result, the time error measuring process were run several times using different variables (figure 4.10).

Time and frequency domain normalization

As discussed in the method chapter, onebit normalization and spectral whitening are non-linear operations and the order of which they are applied can affect the final result. Figure 4.10 shows that, just like different combinations of onebit normalization (1B) and spectral whitening (SW) give slightly different waveforms (figure 4.10a,c,e), the measured time delays are similar with only small differences. When measuring time delays from the cross correlation of only onebit normalized noise, the found time delays are slightly higher, up to 1 s compared to 0.8 s from the cross correlation of first spectral whitened and then onebit normalized noise, and 0.6 s from the cross correlation of first onebit normalized then spectral whitened noise. These differences are mainly found between day 650 and 705, 12th of August until 26th of September 2015.

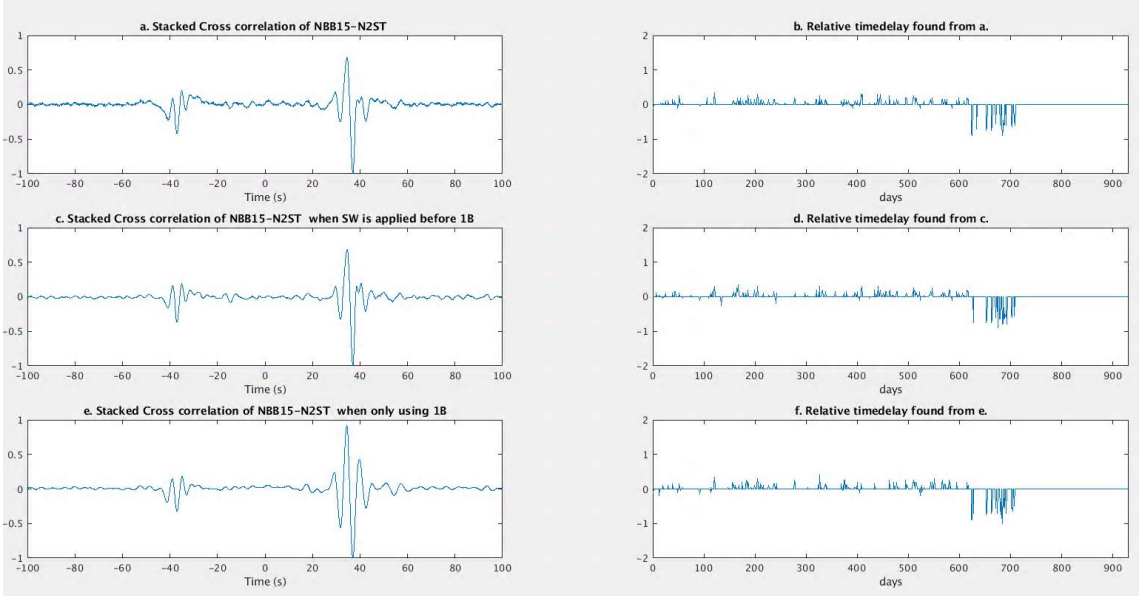

Figure 4.10: The noise correlations and relative time delays found for station pair NBB15-N2ST using different variables.

Reference trace

As described in the method chapter, the time delays are measured by comparing daily cross correlations with a reference trace. The reference trace is usually derived from the same cross correlations, but stacked over longer periods. Figure 4.11 shows

the measured time delays when the reference trace is stacked over the entire period (figure 4.11b), every month (figure 4.11d) and over the 10 previous days (figure 4.11f). The different reference traces do not give the same results. For the days 638 until 731 (21st of July until 22nd of October 2015), the found time delays are more accurate for the reference trace stacked over the entire period. On the other hand, the reference trace stacked over the entire period measures no time delays after day 731, when the large time shift shown in figure 4.5 occurs. This is also the case for the trace stacked monthly, but not for the reference trace stacked over the previous 10 days. Still, the time delays measured using reference traces stacked over 10 days are not comparable to the shifts seen in figure 4.5. However, this is only the case for station pair NBB15-N2ST, when using reference traces stacked over 10 days on other station pairs involving NBB15 the time delays are still zero after day 710 (figure 4.12)

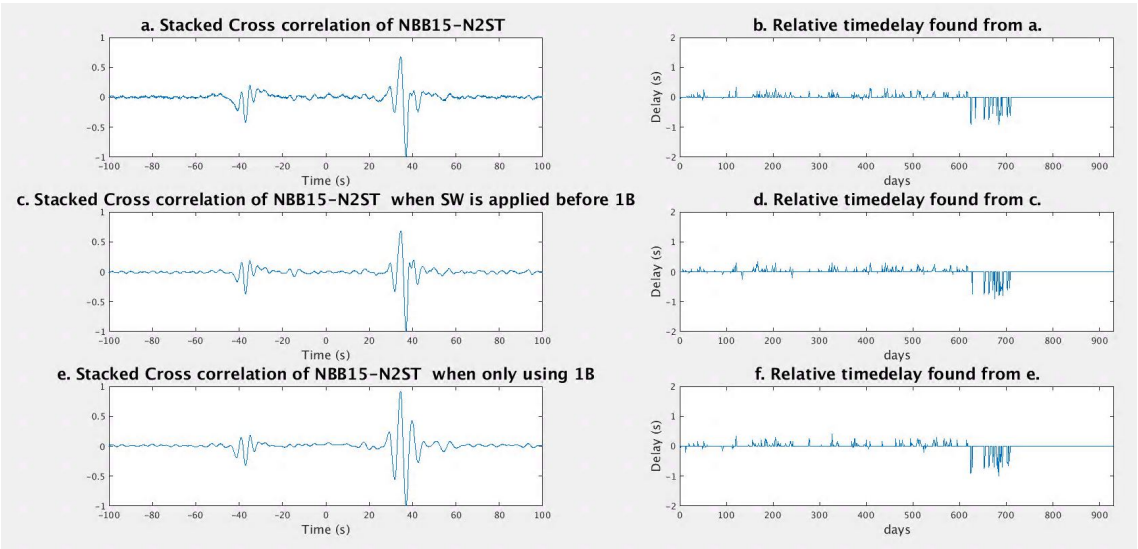

Figure 4.11: The noise correlations(a,c,e) and relative time delays found for station pair NBB15-N2ST, using a reference trace stacked over the (b) entire period, (d) monthly and (f) over the 10 previous days. Note that the time delays in f are found using 10 iterations of the measuring method instead of 3.

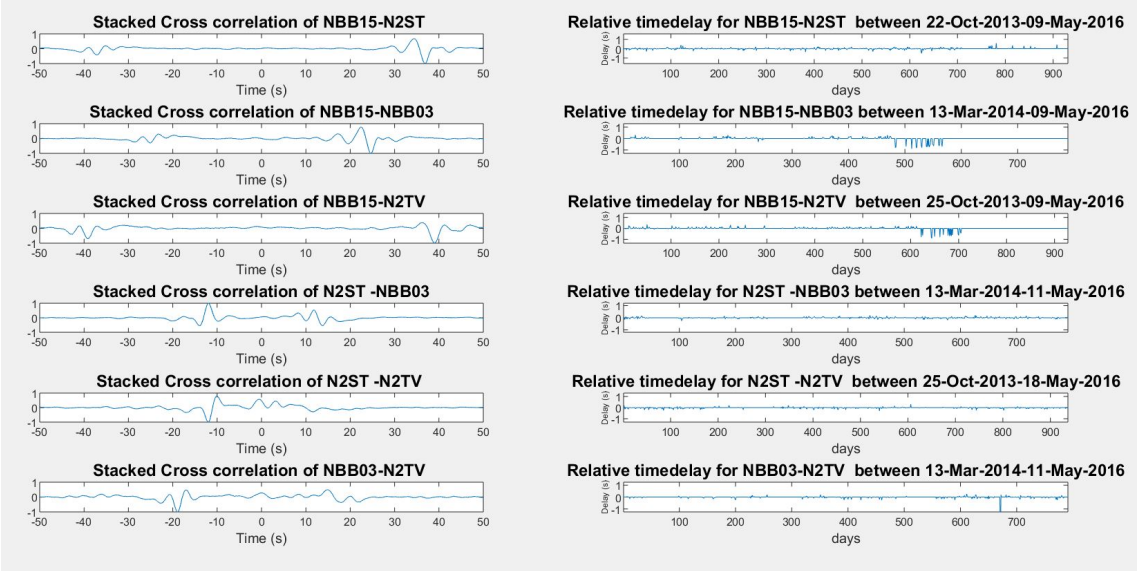

Figure 4.12: The noise correlations and relative time delays found for station pairs involving the station NBB15, using reference traces stacked over 10 days.

Measuring time delays on the entire signal

The time shifts of station NBB15 have shifted the entire signal so that both the causal and acausal part of the signal is on positive lag side. Since the measuring method separates positive and negative side before measuring, and only the time shifts that occur on both sides, but with opposite sign, are registered, the large time shifts of NBB15 are not detected. The measuring method without separating the causal and acausal part of the signal, is therefore also applied to stations involving NBB15.

Figure 4.13 shows when measuring over the entire signal, the time delays found after day 700, October 2015, are consistent with the large time shifts observed for the daily cross correlations (figure 4.5a and 4.6). However, a few large time shifts are also detected before day 700, which are not observed for the daily cross correlations.

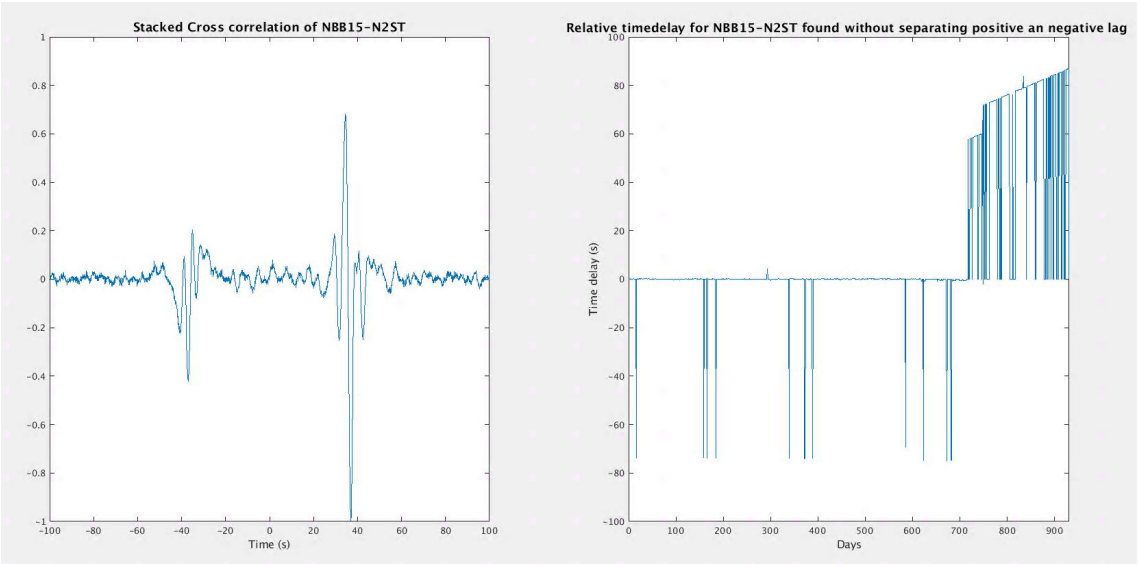

Figure 4.13: The noise correlations and relative time delays found for station pairs NBB15-N2ST. found by measuring the time delays over the entire signal without separating the causal and acausal side. Note that only signals with correlation coefficient above 0.6 are used.

4.2.2 NBB40

Time shifts are observed for station pair involving NBB40 in figure 4.14 and 4.15. The signal jumps with about -8 s on the 22th of January. After the jump, the time drifts with about 0.07 s/day before jumping about 15 s on the 25th of February and -10 s on the 3th of March. When comparing the found time delays of other station pairs involving these two stations, it becomes clear that the errors have occurred at station NBB40 (figure 4.16 and 4.17). This is also consistent with the GPS logs of NBB40 which recorded only connection to the internal GPS during this period. There were therefore no GPS lock registered between the 22rd of January until the 2nd of March, when the external GPS was reconnected.

Both the time drift and the two jumps are detected by the measuring process (figure 4.16 and 4.17). When inverting the time delays found for each station pair to find the time delay of each station, time delays up to -7.6 s and time drift of 0.25 s is found for station NBB40 (figure (4.18). This is consistent with the jumps and drift observed for the daily cross correlations in figure 4.14 and 4.15.

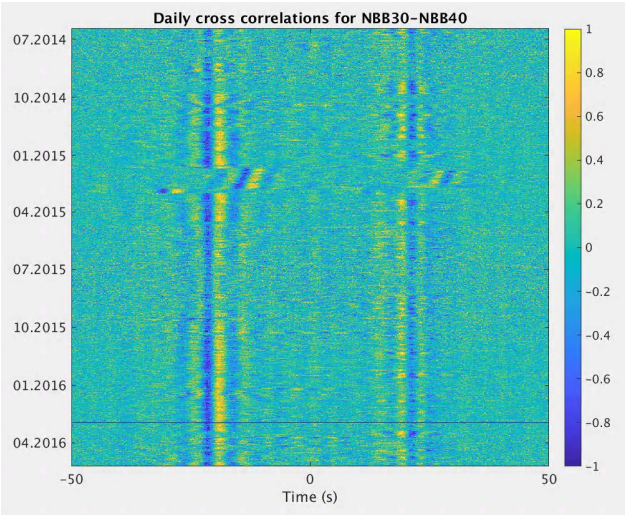

(a)

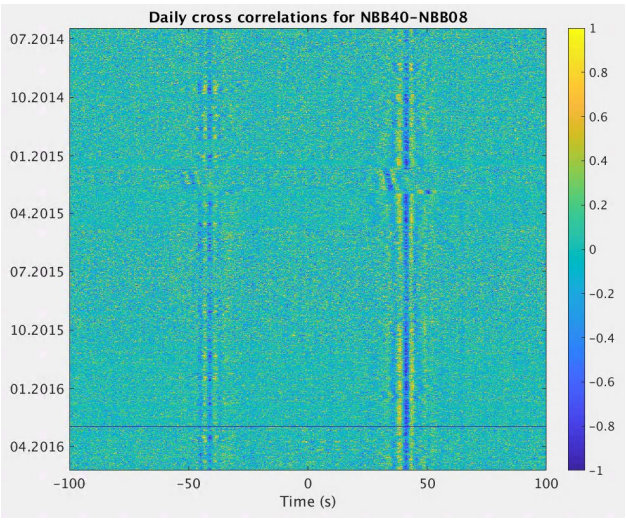

(b)

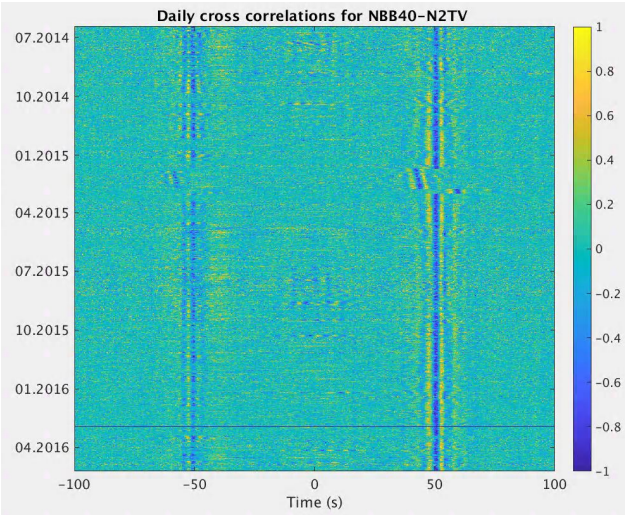

(c)

Figure 4.14: The daily noise correlations found for stations pairs involving NBB40 plotted over the entire period.

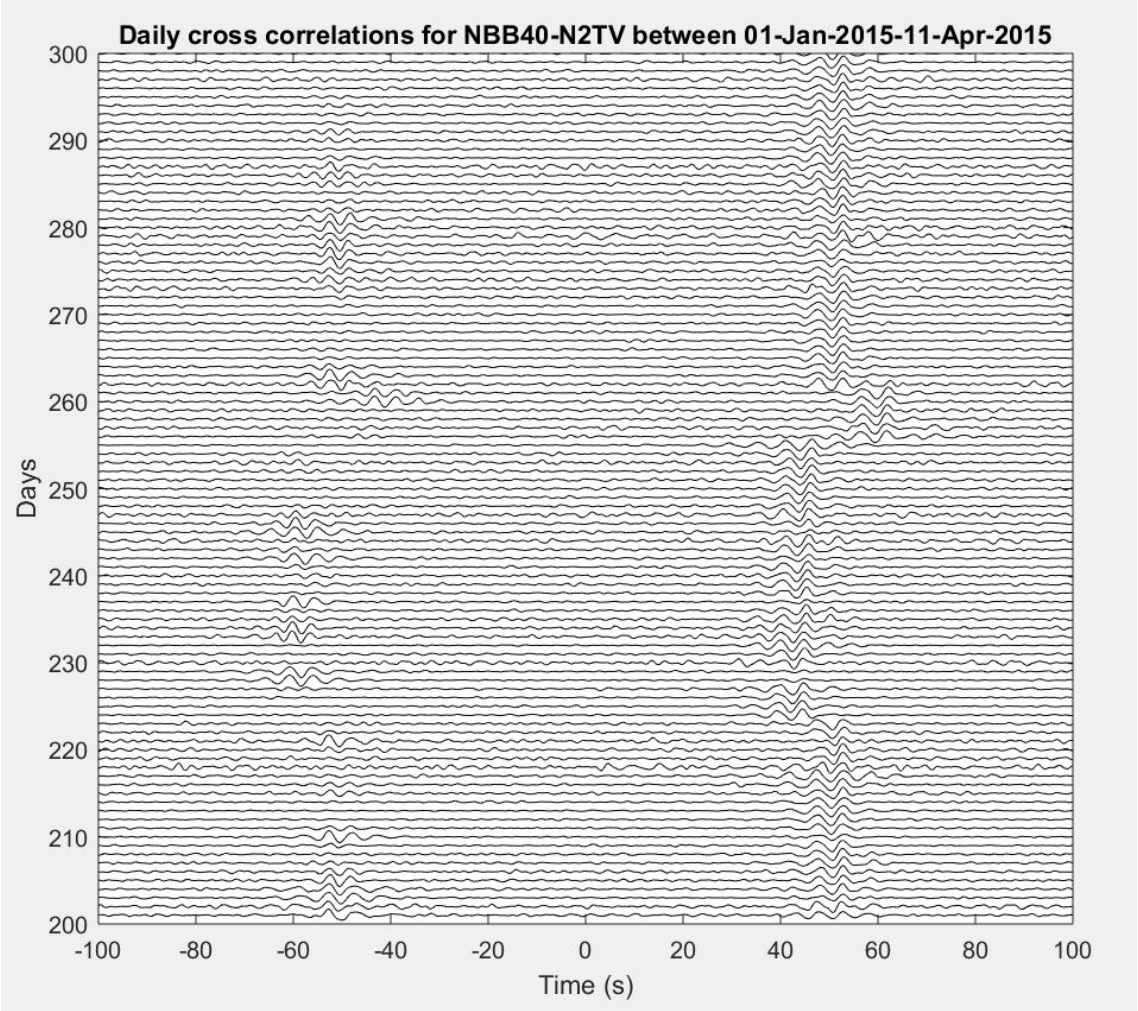

Figure 4.15: The noise correlations and relative time delays found for station pairs NBB40-N2TV between 1th of January until 11th of April 2015. The signal jumps with about -8 s on day 225 (22th of January), drifts with about 0.07 s/day before jumping about 15 s on day 257 (25th of February) and -10 s on day 262 (3th of March).

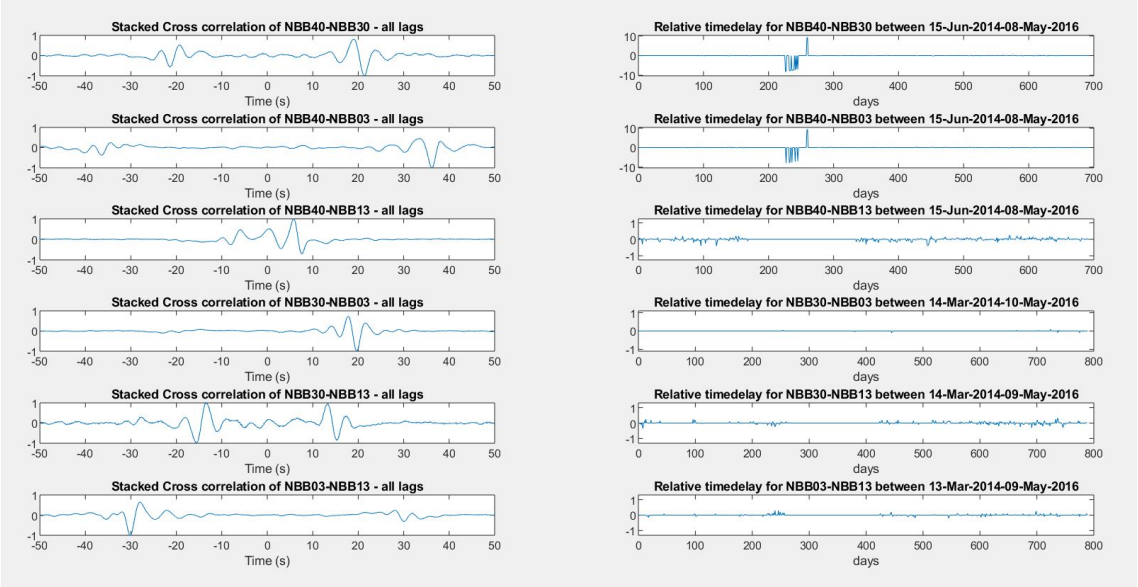

Figure 4.16: The noise correlations and relative time delays found for station pairs involving station NBB40.

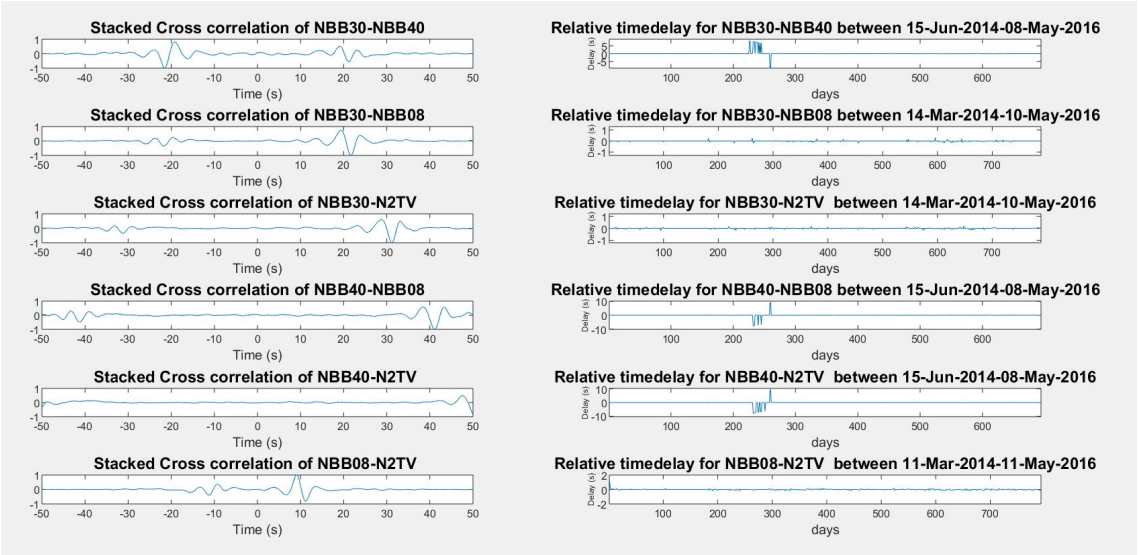

Figure 4.17: The noise correlations and relative time delays found for station pairs involving station NBB40 using reference traces stacked over the 10 previous days.

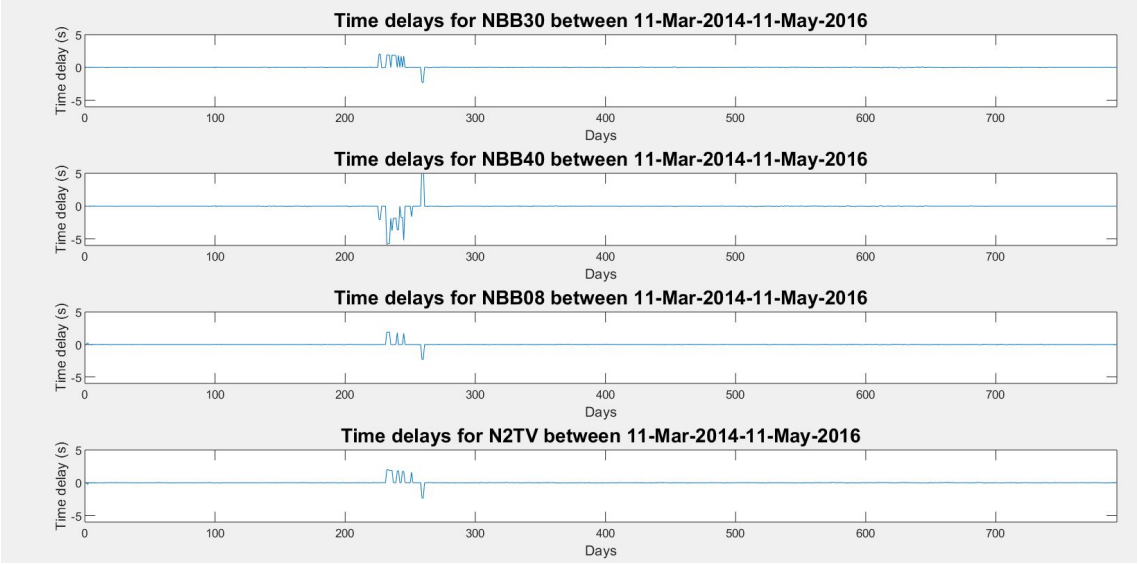

(a)

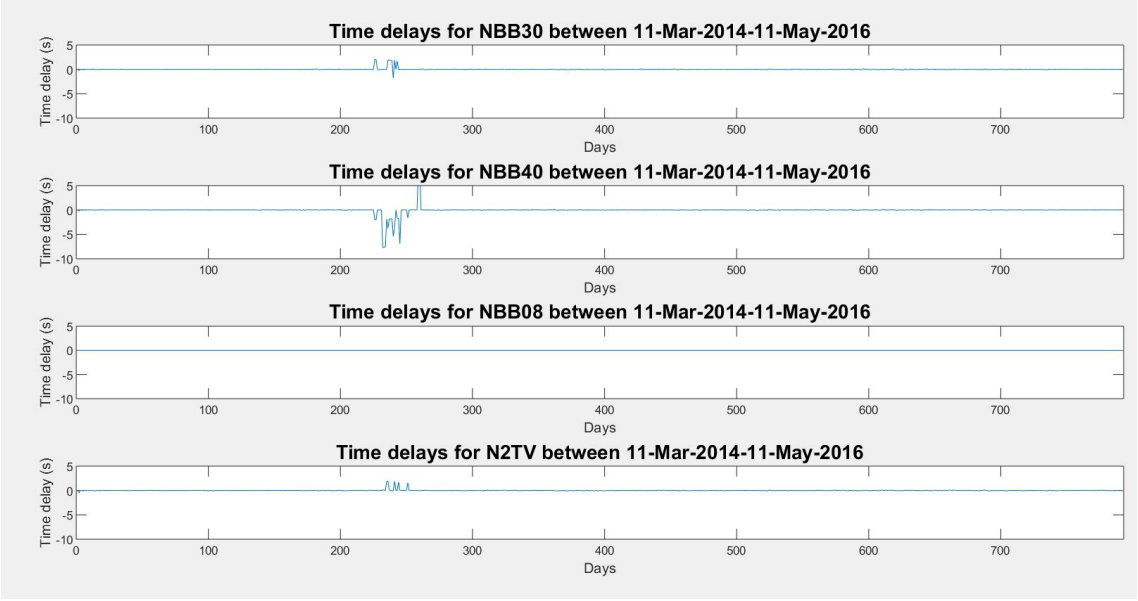

(b)

Figure 4.18: The time delays found for each station. (a) before and (b) after absolute time correction.

4.2.3 NBB29

Smaller time shifts are also observed for station NBB29. These time delays are more inconsistent between the different station pairs involving NBB29. When NBB29 is cross correlated with NBB14, time delays up to 0.5 s are measured (figure 4.21 fifth line from the top). These time shifts occur around day 600, 3rd of November 2015, until day 705, 9th of December 2015. Time shifts this small are difficult, but not impossible, to see when comparing the daily cross correlations (see arrow in figure 4.19). Figure 4.19 shows that the signal drifts with about 0.01 s/day from 3rd of November, and jumps about 0.5 s around 9th of December 2015. The GPS logs for NBB29 showed no GRP locks on these dates .

The same time shift and drift are not visibly detected by the measuring method for the other station pairs involving NBB29 (figure 4.21), but appears after inverting to find the time delays for each station (figure 4.22). The inversion finds time shifts up to 0.45 and time drift of 0.012 s/day, which is consistent with what is observed for the daily cross correlations (figure 4.19).

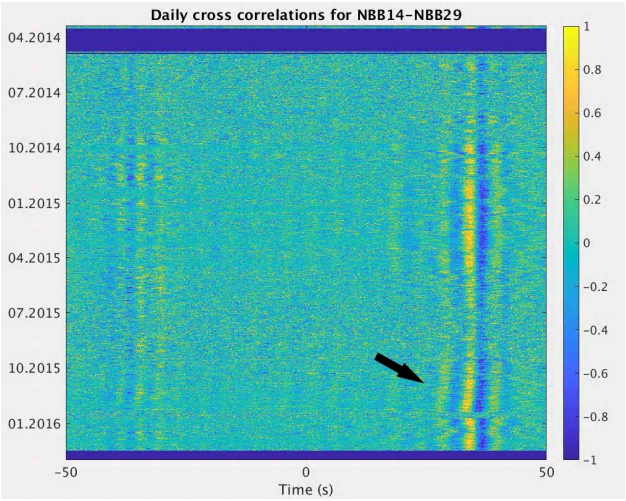

(a)

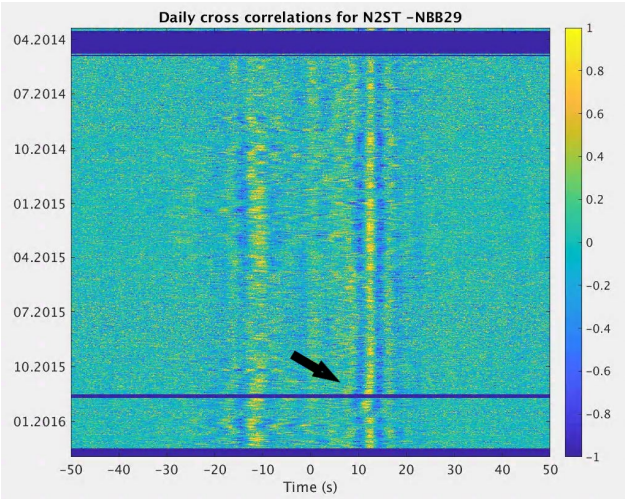

(b)

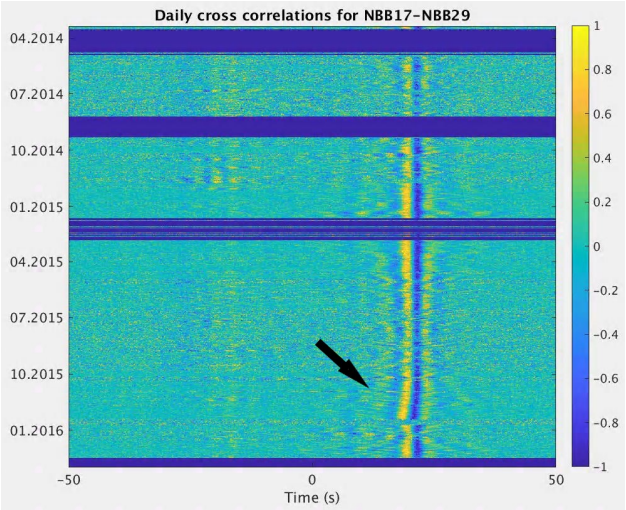

(c)

Figure 4.19: The daily noise correlations found for station pairs involving NBB29, plotted over the entire period.

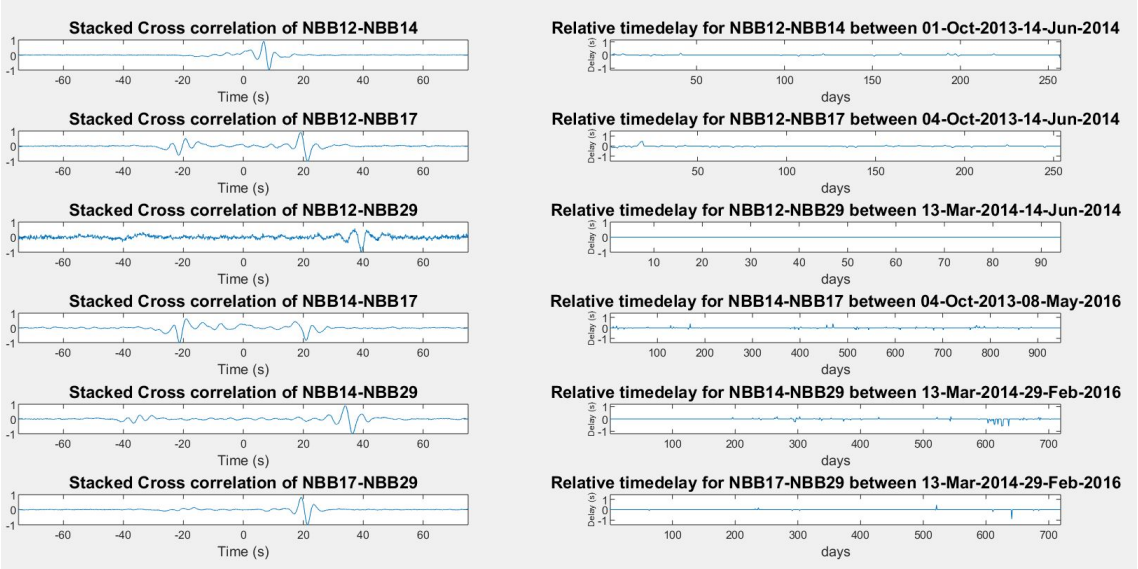

Figure 4.20: The noise correlations and relative time delays found for station pairs involving station NBB29.

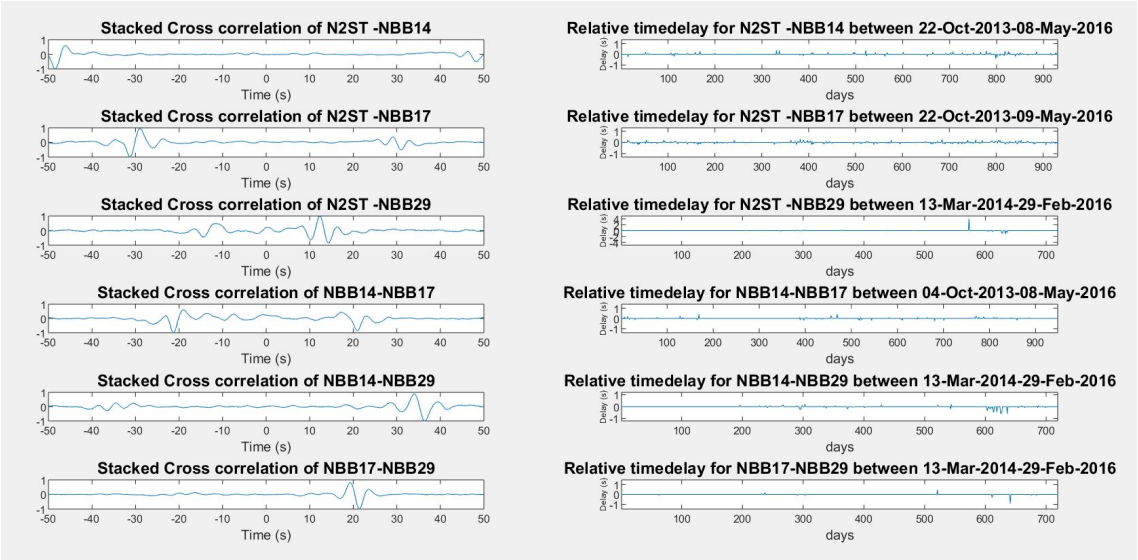

Figure 4.21: The noise correlations and relative time delays found for station pairs involving station NBB29 using reference traces stacked over the 10 previous days.

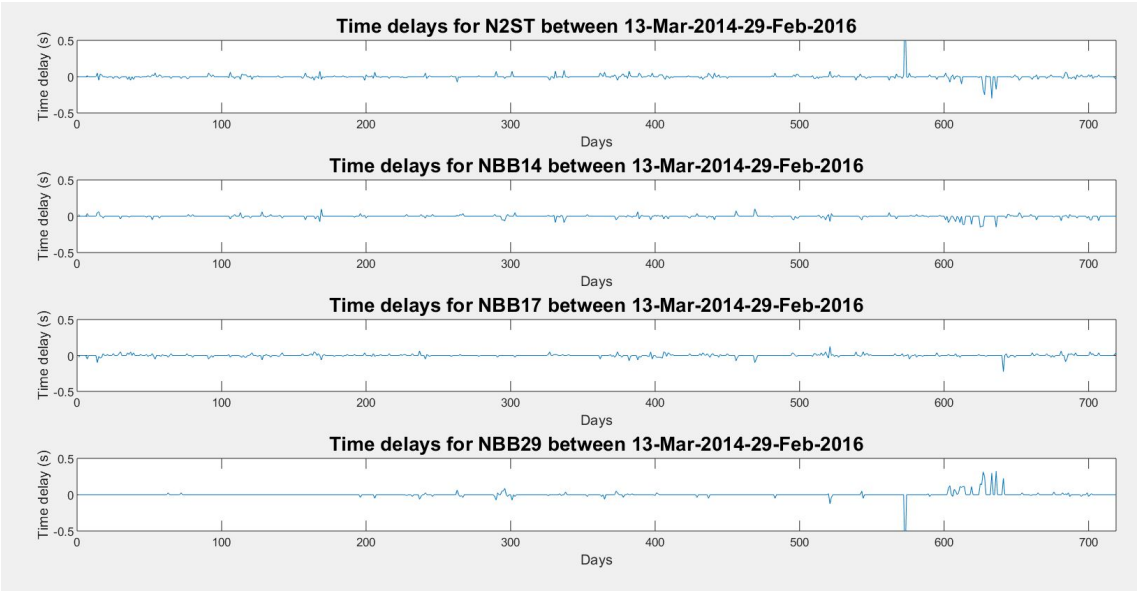

(a)

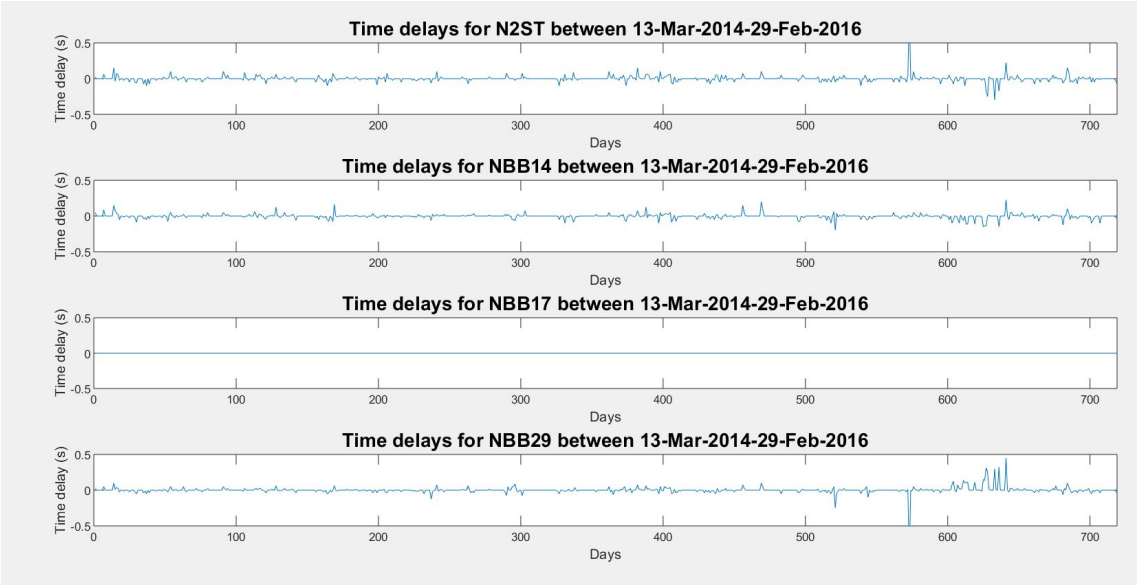

(b)

Figure 4.22: The time delays found for each station. (a) before and (b) after absolute time correction.

4.3 Instrumental problems

4.3.1 N2RO and N2VA

The stations N2RO and N2VA have no apparent timing issues, but it is difficult to retrieve useful Green's function from. Several of the cross correlations involving these two stations do not converge towards the Green's function and are therefore not possible to measure time shifts from (figure 4.24, 4.25 and 4.26). There are two exceptions, when N2RO and N2VA are cross correlated with each other or with station N2SV, which is also the station closest to N2RO and N2VA.

N2RO, N2VA N2SV are located on the islands Røst, Værøy and Moskenes, respectively (figure 2.8). The structure of the crust and mantle under these islands is complicated compared to the area around, with a shallow Moho estimated to 20 km depth (Michálek et al., 2018)). Station N2RO and N2VA are also situated in buildings close to town centres, see overview of station locations in figure 2.9. However, there can be many reasons for why cross correlations with stations N2RO and N2VA do not converge towards the Green's function, this is not within the scope of this thesis.

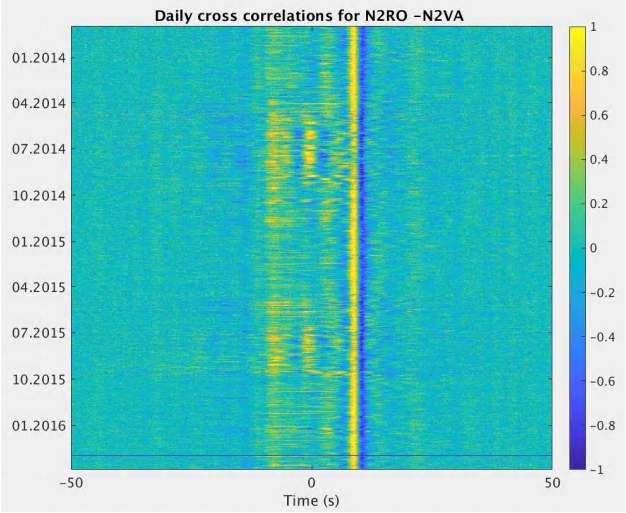

(a)

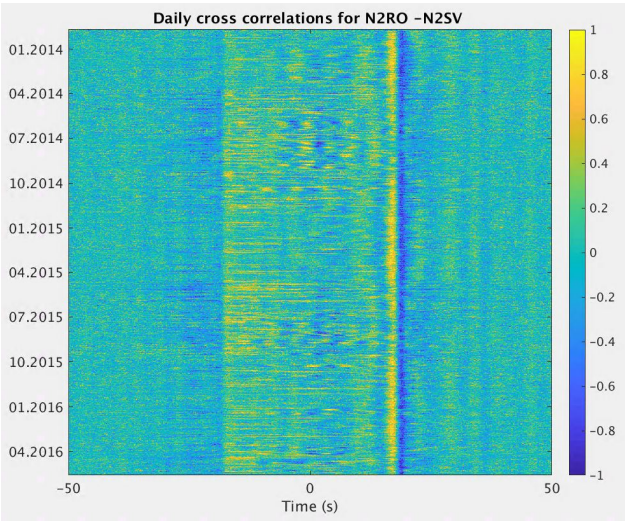

(b)

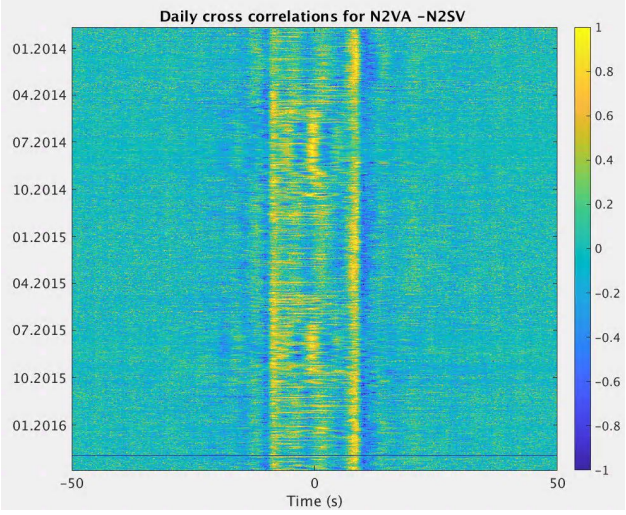

(c)

Figure 4.23: The daily noise correlations found for station pairs involving N2RO, plotted over the entire period.

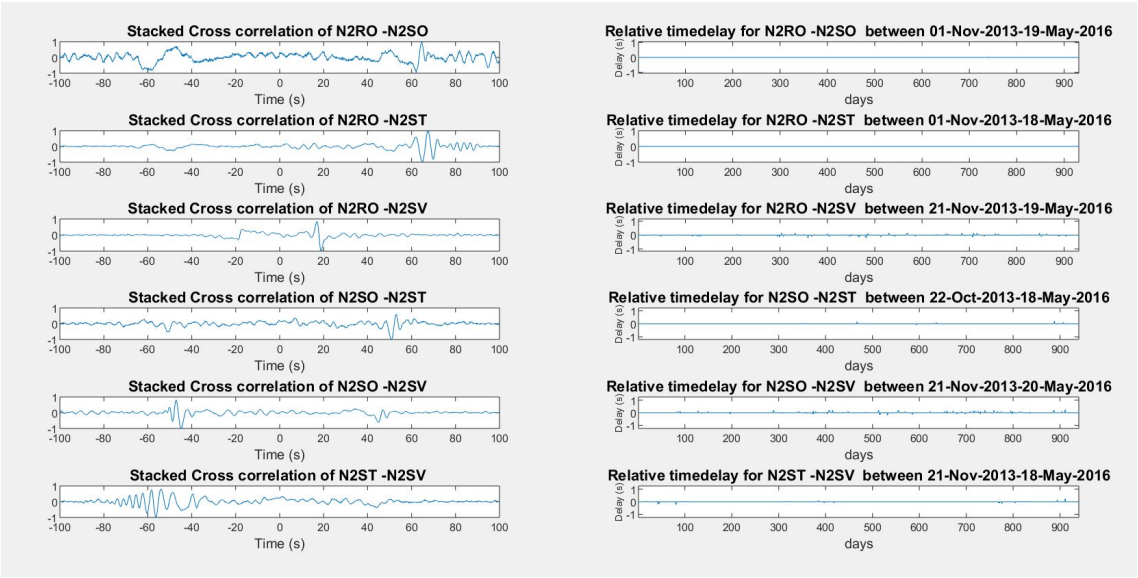

Figure 4.24: The noise correlations and relative time delays found for station pairs involving station N2RO.

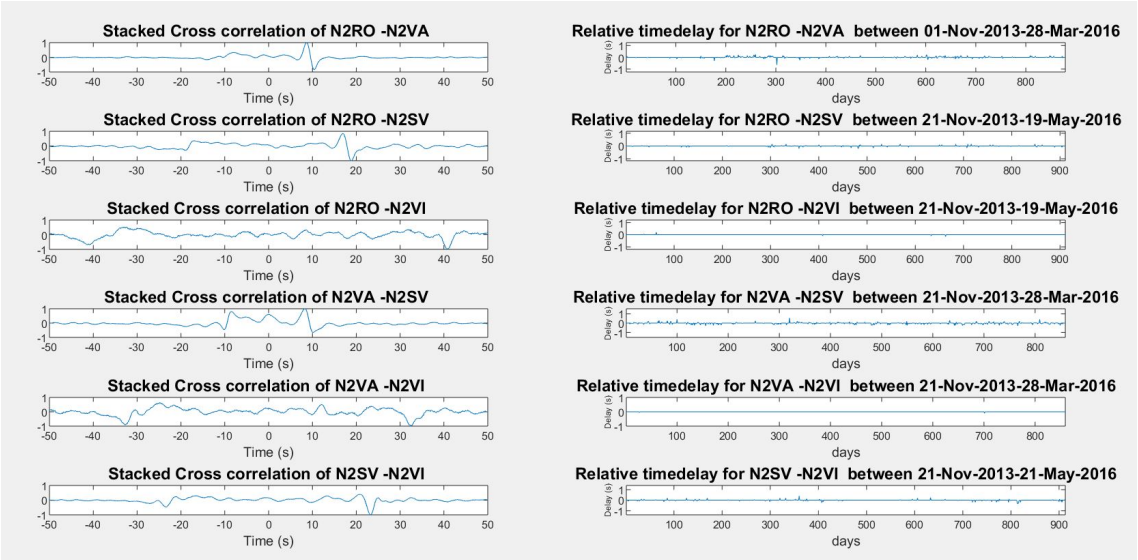

Figure 4.25: The noise correlations and relative time delays found for station pairs involving stations N2RO and N2VA.

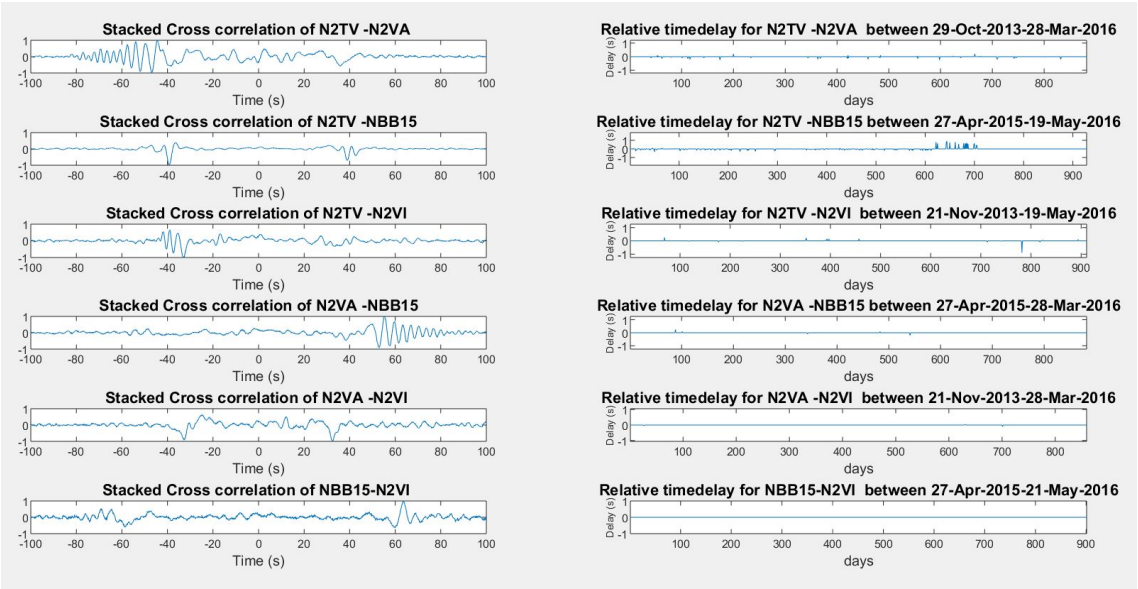

Figure 4.26: The noise correlations and relative time delays found for station pairs involving station N2VA.

4.4 Noise distribution

The distribution of noise sources is investigated using the found noise correlations, the calculated azimuth of the station pairs and amplitude ratio between the causal and acausal part of the signal. Figure 4.27 shows the stations pairs plotted in colour coded lines, where blue indicates a small causal/acausal signal ratio, and red indicates a high causal/acausal signal ratio. The station pairs are mostly cross correlated in the same direction, from south-west to north-east, see arrows in figure 4.27. This shows that station-pairs which are approximately aligned with the coast mostly have a small causal/acausal signal ratio, meaning that the signal is more or less symmetric. The station pairs aligned more perpendicular to the coast usually have higher causal/acausal signal ratio, and thus a more asymmetric signal.

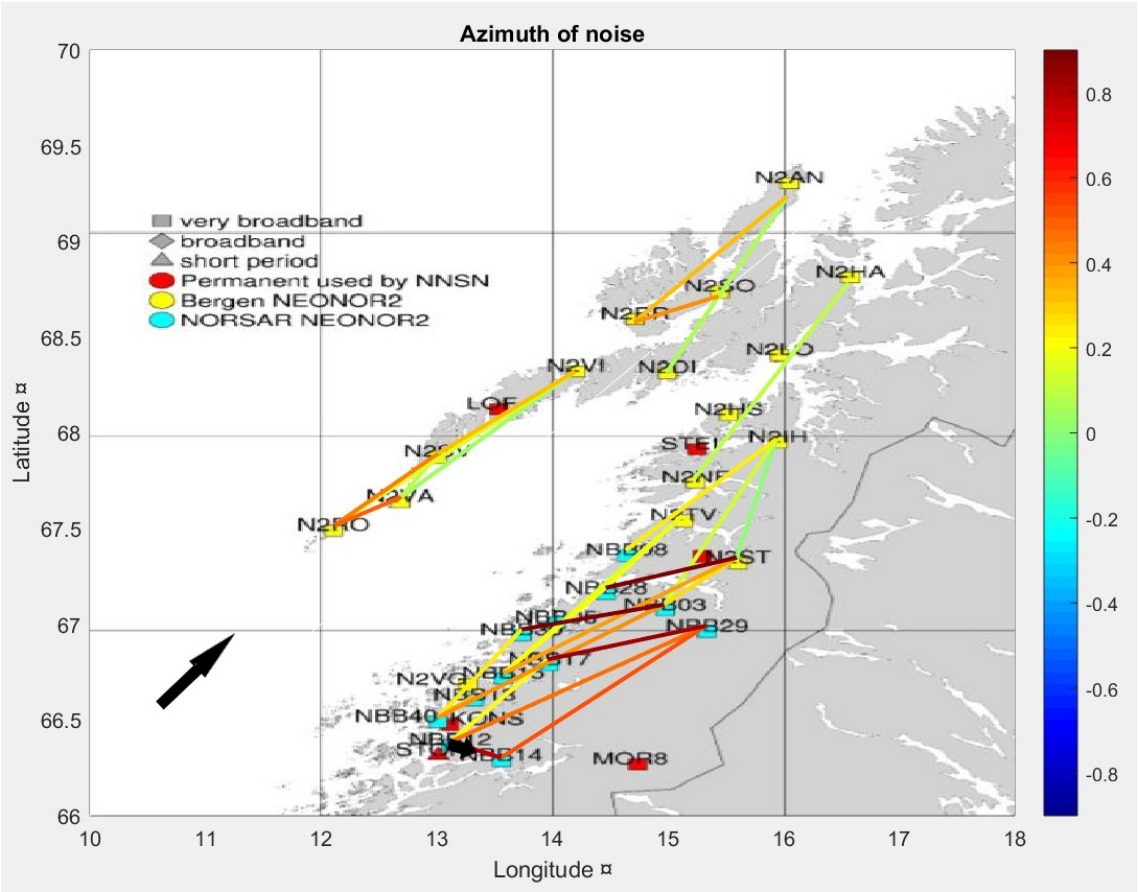

Figure 4.27: Map over the NEONOR2 study area, where the cross correlated station pairs are linked by lines colour coded by the causal/acausal signal ratio. The value of the ratios are indicated next to the colorbar, blue indicates small causal/acausal signal ratio, and red indicates high causal/acausal signal. Most of the station pairs are cross correlated from south-west to north-east, see the direction of large arrow. The exception is station NBB12-NBB14, which is cross correlated from west to east, see the small arrow.

The cross correlations are also plotted as a function of azimuth and distance, as shown in figure 4.28 and 4.29. These figures show that the noise correlations are more or less symmetric, with slightly stronger amplitudes at causal side, for station pairs in the north-east direction, azimuth 20 to 50 degrees. Station pairs with higher azimuths, on the other hand, have much higher amplitudes on the causal side of the signal.

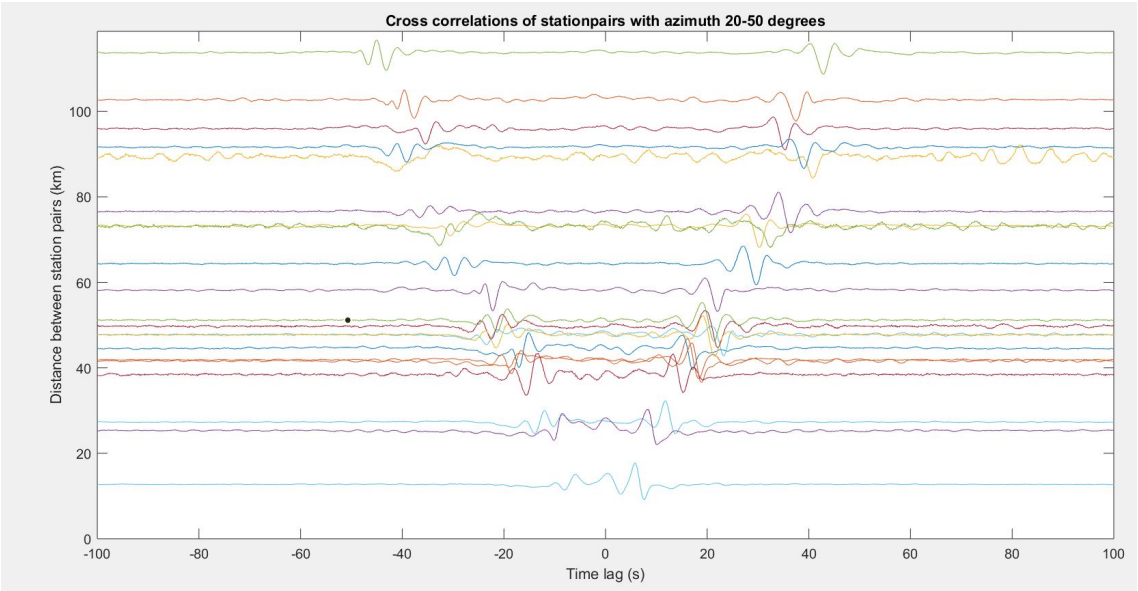

Figure 4.28: Stacked cross correlations with station pair azimuth between 20-50 degrees.

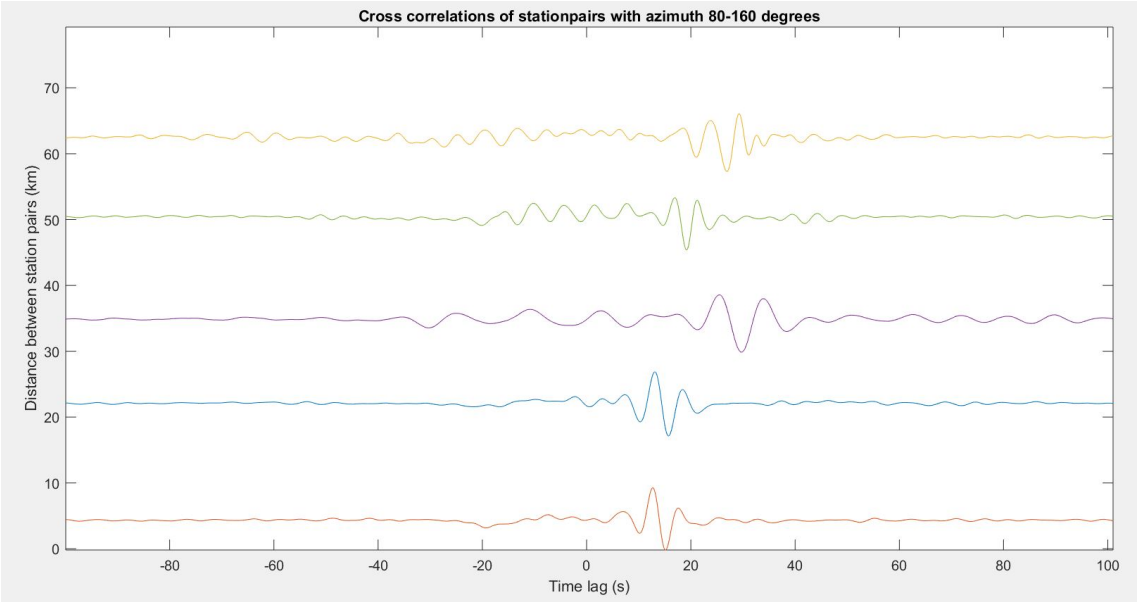

Figure 4.29: Stacked cross correlations with station pair azimuth between 80-160 degrees.

Chapter 5

Discussion

In this thesis, I have developed a tool to estimate the Green's function from ambient seismic noise, and a measuring method to find changes in the Green's functions. Here, these changes are used to investigate instrumental timing issues. However, the same procedure can be applied to measure changes in the physical properties of the structure.

Careful processing is necessary before the Green's function can be derived from ambient seismic noise. I have carefully examined the importance and limitations of the different aspects of the process and found timing errors in the data set.

5.1 Noise distribution

The main uncertainty of the method is the noise distribution. An even distribution of noise sources is a necessary requirement for estimating the Green's function from noise correlations. Since changes are found as shifts in the Green's function, a good estimate of the Green function is crucial in the measuring process.

The NEONOR2 network used in this thesis, is located along the Nordland coast and the noise sources are therefore not uniformly distributed. Seismic noise mainly comes from oceanic sources, as is discussed in the Background chapter, and station-pairs that are aligned with the coast show more symmetric noise correlations than those that are more perpendicular to the coast. This is shown in the noise distribution analysis in the result chapter.

Instrumental timing errors shifts the entire Green's function, causing an asymmetric change in the waveform. This contrasts with velocity changes in the structure, which induce the same shift to both causal and acausal part of the signal. To ensure qualitative measurements, time shifts are therefore measured for the causal and

acausal part separately and only the time shifts that occur on both sides, but with opposite sign, are used. However, this requirement makes completely asymmetric signals unusable in this process. An alternative is to apply the measuring process to the entire signal. However, this increases the uncertainty of the found time delays, as shown in the method chapter, and should rather be used as comparison to time delays measured from more reliable cross correlations.

These issues make it difficult to keep the process completely automatic, as station pairs should be chosen with regards to the noise directivity and one-sided signals should be measured with care.

5.2 Timing errors

Timing errors were found for station NBB15, NBB40 and NBB29. Instrumental timing errors are usually caused by problems with the digitizer or GPS receiver, which can result in time jumps or drift in the signal. Both these effects are observed in NEONOR2 stations and successfully detected for stations NBB40 and NBB29.

However, only smaller timing issues are measured by the measuring method. This is especially clear for station NBB15, where the daily cross correlations show two large time jumps of 10-50 s and linear drift up to 0.1 s/day (figure 4.5), while only smaller time delays up to 0.5 s and no time drift are detected by the original measuring process (figure 4.7 and 4.8).

The large time shifts of NBB15 are not detected because the signal has shifted both the causal and acausal part over to the positive lag side of the signal. This makes the signal asymmetric, and as explained above, the method does not measure time delays of completely asymmetric signals. An alternative is to measure the time delays over the entire signal instead of separating the causal and acausal part of the signal, as shown in figure 4.13. However, not separating the causal and acausal part of the signal, makes is harder to distinguish between instrumental timing errors and natural shifts, like seasonal fluctuations and velocity changes. In addition, large time shifts and drift are easily observed when comparing daily cross correlations, like in figure 4.5 and 4.6, and can thus be measured directly, without applying the method.

Another important consideration is the stack length of the reference trace used to measure the time delays of the daily cross correlations. Stacking over longer time periods gives a cleaner signal with higher SNR (figure 3.44 and 3.46). Nevertheless, if there are large fluctuations, shifts or drift in the signal, the reference trace stacked over longer periods might end up too different from the daily cross correlations, and time delays cannot be measured. In these cases, using a reference trace stacked over shorter periods might be beneficial. This is however not the case for station pairs

involving NBB15. Although using a reference traces stacked over 10 days measured more time delays than the reference traces stacked over longer period (figure 3.44), the measured time delays were not compatible the time shifts observed in figure 4.5.

The observed, but not measured, timing issues with station NBB15 shows that the measuring method is only semi-automatic, as the daily cross correlations should also be checked manually and the measuring process should be adjusted to more complicated signals. However, when combining observations from daily cross correlations and the time delays measured using the measuring method, a good overview of the network timing, is obtained.

5.3 Different variables

Finally, after having tested the processing procedure and measuring method using different bandpass filters, time window length, normalization combination and reference traces, it is clear that the different variables have little significant effect on the final waveform and measured time delays. The most sensitive step is the bandpass filtering, both before and after cross correlations. It is especially true when not applying spectral whitening, since the microseismic peaks in the amplitude spectrum can affect the shape of the waveform (figure 3.17), and the frequency band should be chosen accordingly.

5.4 Outlook

Although the measuring method requires some improvements, the process scheme successfully calculates the Green's function between stations in the NEONOR2 network. These Green's functions can be further used to search for property changes in structure or extract dispersion curves for tomography inversion.

Since the processing scheme for estimating the Green's function is fully automatic, it can also be applied continuously to a recording network and thus estimate the Green's function in real time. This can be further used to monitor immediate velocity changes.

Chapter 6

Conclusion

I have presented a method that calculates the Green's function from ambient seismic noise and use the estimated Green's function to measure time shifts caused by instrumental errors in the signal. The method has been applied to noise recorded on the temporary NEONOR2 network between October 2013 and May 2016, and timing errors were found for stations NBB15, NBB40 and NBB29. The measuring method is not completely automatic, as adjustments are needed when dealing with complicated signals or time shifts.

I have examined the effects different aspects of the method have on the final results and showed that the most important step is to calculate a good estimate of the Green's function. As long as the noise correlations converge towards a satisfactory Green's function, shifts in the signal can either be observed directly from comparing the daily cross correlations with each other, or using the measuring method. The estimated Green's function can further be used to investigate the structure of the Earth, either by extracting dispersion curves and invert for velocity, or by measuring shifts caused by property changes instead of instrumental errors.

Bibliography

Aki, K. (1957). Space and time spectra of stationary stochastic waves, with special reference to microtremors. *Bull. Earthquake Res. Inst.*, 35.

Bensen, G. D., Ritzwoller, M. H., Barmin, M. P., Levshin, A. L., Lin, F., Moschetti, M. P., Shapiro, N. M., and Yang, Y. (2007). Processing seismic ambient noise data to obtain reliable broad-band surface wave dispersion measurements. *Geophysical Journal International*, 169(3):1239–1260.

Boué, P., Poli, P., Campillo, M., Pedersen, H., Briand, X., and Roux, P. (2013). Teleseismic correlations of ambient seismic noise for deep global imaging of the Earth. *Geophysical Journal International*, 194(2):844–848.

Brenguier, F., Campillo, M., Hadziioannou, C., Shapiro, N. M., Nadeau, R. M., and Larose, E. (2008a). Postseismic relaxation along the San Andreas fault at Parkfield from continuous seismological observations. *Science*, 321(5895):1478–1481.

Brenguier, F., Shapiro, N. M., Campillo, M., Ferrazzini, V., Duputel, Z., Coutant, O., and Nercessian, A. (2008b). Towards forecasting volcanic eruptions using seismic noise. *Nature Geoscience*, 1(2):126–130.

Bungum, H. and Havskov, J. (1986). Source parameters for earthquakes in the northern North Sea. *Norsk Geologisk Tidsskrift*, 67:51–58.

Bussat, S. and Kugler, S. (2011). Offshore ambient-noise surface-wave tomography above 0.1 Hz and its applications. *The Leading Edge*, 30(5):514–524.

Chen, J. H., Froment, B., Liu, Q. Y., and Campillo, M. (2010). Distribution of seismic wave speed changes associated with the 12 May 2008 Mw 7.9 Wenchuan earthquake. *Geophysical Research Letters*, 37(18):n/a–n/a.

Demuth, A., Ottemöller, L., and Keers, H. (2016). Ambient noise levels and detection threshold in Norway. *Journal of Seismology*, 20(3):889–904.

Derode, A., Larose, E., Campillo, M., and Fink, M. (2003a). How to estimate the Green's function of a heterogeneous medium between two passive sensors? Application to acoustic waves. *Applied Physics Letters*, 83(15):3054–3056.

Derode, A., Larose, E., Tanter, M., de Rosny, J., Tourin, A., Campillo, M., and Fink, M. (2003b). Recovering the Green's function from field-field correlations in an open scattering medium (L). *The Journal of the Acoustical Society of America*, 113(6):2973.

Draganov, D., Campman, X., Thorbecke, J., Verdel, A., and Wapenaar, K. (2009). Reflection images from ambient seismic noise. *GEOPHYSICS*, 74(5):A63–A67.

Draganov, D. S., Wapenaar, K., Mulder, W., Singer, J., and Verdel, A. (2007). Retrieval of reflections from seismic background-noise measurements. *Geophysical Research Letters*, 34(4):L04305.

Duvall, T. L., Jeffferies, S. M., Harvey, J. W., and Pomerantz, M. A. (1993). Time-distance helioseismology. *Nature*, 362(6419):430–432.

Friedrich, A., Krüger, F., and Klinge, K. (1998). Ocean-generated microseismic noise located with the Gräfenberg array. *Journal of Seismology*, 2(1):47–64.

Froment, B., Campillo, M., Chen, J. H., and Liu, Q. Y. (2013). Deformation at depth associated with the 12 May 2008 MW 7.9 Wenchuan earthquake from seismic ambient noise monitoring. *Geophysical Research Letters*, 40(1):78–82.

Gerstoft, P., Shearer, P. M., Harmon, N., and Zhang, J. (2008). Global P, PP, and PKP wave microseisms observed from distant storms. *Geophysical Research Letters*, 35(23):L23306.

Gouédard, P., Seher, T., McGuire, J. J., Collins, J. A., and van der Hilst, R. D. (2014). Correction of ocean-bottom seismometer instrumental clock errors using ambient seismic noise. *Bulletin of the Seismological Society of America*, 104(3):1276–1288.

Groos, J. C. (2010). Broadband Seismic Noise : Classification and Greens Function Estimation. page 165.

Gutenberg, B. (1958). Microseisms. *Advances in Geophysics*, 5(C):53–92.

Hadziioannou, C., Larose, E., Baig, A., Roux, P., and Campillo, M. (2011). Improving temporal resolution in ambient noise monitoring of seismic wave speed. *Journal of Geophysical Research: Solid Earth*, 116(7):B07304.

Hadziioannou, C., Larose, E., Coutant, O., Roux, P., and Campillo, M. (2009). Stability of Monitoring Weak Changes in Multiply Scattering Media with Ambient Noise Correlation: Laboratory Experiments. *The Journal of the Acoustical Society of America*, 125(6):3688–3695.

Havskov, J. and Alguacil, G. (2010). *Instrumentation in Earthquake Seismology*. Modern Approaches in Geophysics. Springer Netherlands.

Havskov, J. and Ottemoller, L. (2010). *Routine Data Processing in Earthquake Seismology: With Sample Data, Exercises and Software*. Springer Netherlands.

Herrmann, R. B. (2013). Computer Programs in Seismology: An Evolving Tool for Instruction and Research. *Seismological Research Letters*, 84(6):1081–1088.

Kang, T. S. and Shin, J. S. (2006). Surface-wave tomography from ambient seismic noise of accelerograph networks in southern Korea. *Geophysical Research Letters*, 33(17):L17303.

Kedar, S., Longuet-Higgins, M., Webb, F., Graham, N., Clayton, R., and Jones, C. (2008). The origin of deep ocean microseisms in the North Atlantic Ocean. *Proceedings of the Royal Society A: Mathematical, Physical and Engineering Sciences*, 464(2091):777–793.

Köhler, A., Weidle, C., and Maupin, V. (2011). Directionality analysis and Rayleigh wave tomography of ambient seismic noise in southern Norway. *Geophysical Journal International*, 184(1):287–300.

Landés, M., Hubans, F., Shapiro, N. M., Paul, A., and Campillo, M. (2010). Origin of deep ocean microseisms by using teleseismic body waves. *Journal of Geophysical Research: Solid Earth*, 115(5):B05302.

Larose, E., Derode, A., Campillo, M., and Fink, M. (2004). Imaging from one-bit correlations of wideband diffuse wave fields. *Journal of Applied Physics*, 95(12):8393–8399.

Larose, E., Lobkis, O. I., and Weaver, R. L. (2006). Passive correlation imaging of a buried scatterer. *The Journal of the Acoustical Society of America*, 119(6):3549–3552.

Lin, F. C., Tsai, V. C., Schmandt, B., Duputel, Z., and Zhan, Z. (2013). Extracting seismic core phases with array interferometry. *Geophysical Research Letters*, 40(6):1049–1053.

Lobkis, O. I., Weaver, R. L., and Introduction, I. (2001). of a Diffuse Field. *The Journal of the Acoustical Society of America*, 110(6):3011–3017.

Longuet-Higgins, M. S. (1950). A Theory of the Origin of Microseisms. *Philosophical Transactions of the Royal Society A: Mathematical, Physical and Engineering Sciences*, 243(857):1–35.

Mainsant, G., Larose, E., Brnnimann, C., Jongmans, D., Michoud, C., and Jaboyedoff, M. (2012). Ambient seismic noise monitoring of a clay landslide: Toward failure prediction. *Journal of Geophysical Research: Earth Surface*, 117(1):n/a–n/a.

Maupin, V., Agostini, A., Artemieva, I., Balling, N., Beekman, F., Ebbing, J., England, R. W., Frassetto, A., Gradmann, S., Jacobsen, B. H., Köhler, A., Kvarven,

T., Medhus, A. B., Mjelde, R., Ritter, J., Sokoutis, D., Stratford, W., Thybo, H., Wawerzinek, B., and Weidle, C. (2013). The deep structure of the Scandes and its relation to tectonic history and present-day topography. *Tectonophysics*, 602:15–37.

McClellan, J. H., Schafer, R. W., and Yoder, M. A. (2007). *DSP First (2Nd Edition)*. Prentice-Hall, Inc., Upper Saddle River, NJ, USA.

Meier, U., Shapiro, N. M., and Brenguier, F. (2010). Detecting seasonal variations in seismic velocities within Los Angeles basin from correlations of ambient seismic noise. *Geophysical Journal International*, 181(2):985–996.

Michálek, J., Tjåland, N., Drottning, A., Strømme, M. L., Storheim, B. M., Rondenay, S., and Ottemöller, L. (2018). Report on seismic observations within the NEONOR2 project in the Nordland region, Norway. Technical report, University of Bergen, Bergen.

Mordret, A., Landés, M., Shapiro, N. M., Singh, S. C., Roux, P., and Barkved, O. I. (2013). Near-surface study at the valhall oil field from ambient noise surface wave tomography. *Geophysical Journal International*, 193(3):1627–1643.

Moschetti, M. P., Ritzwoller, M. H., and Shapiro, N. M. (2007). Surface wave tomography of the western United States from ambient seismic noise: Rayleigh wave group velocity maps. *Geochemistry, Geophysics, Geosystems*, 8(8):n/a–n/a.

Nishida, K. (2013). Global propagation of body waves revealed by cross-correlation analysis of seismic hum. *Geophysical Research Letters*, 40(9):1691–1696.

Oxford English Dictionary (2018). equipartition, n. : Oxford English Dictionary.

Poli, P., Campillo, M., and Pedersen, H. (2012a). Body-wave imaging of Earth's mantle discontinuities from ambient seismic noise. *Science*, 338(6110):1063–1065.

Poli, P., Pedersen, H. A., and Campillo, M. (2012b). Emergence of body waves from cross-correlation of short period seismic noise. *Geophysical Journal International*, 188(2):549–558.

Rhie, J. and Romanowicz, B. (2004). Excitation of Earth's continuous free oscillations by atmosphere-ocean- seafloor coupling. *Nature*, 431(7008):552–556.

Ritzwoller, M. H., Lin, F. C., and Shen, W. (2011). Ambient noise tomography with a large seismic array. *Comptes Rendus - Geoscience*, 343(8-9):558–570.

Rivet, D., Campillo, M., Shapiro, N. M., Cruz-Atienza, V., Radiguet, M., Cotte, N., and Kostoglodov, V. (2011). Seismic evidence of nonlinear crustal deformation during a large slow slip event in Mexico. *Geophysical Research Letters*, 38(8):n/a–n/a.

Roux, P., Sabra, K. G., Gerstoft, P., Kuperman, W. A., and Fehler, M. C. (2005a). P-waves from cross-correlation of seismic noise. *Geophysical Research Letters*, 32(19):1–4.

Roux, P., Sabra, K. G., Kuperman, W. A., and Roux, A. (2005b). Ambient noise cross correlation in free space: Theoretical approach. *The Journal of the Acoustical Society of America*, 117(1):79–84.

Sabra, K. G., Gerstoft, P., Roux, P., Kuperman, W. A., and Fehler, M. C. (2005a). Extracting time-domain Green's function estimates from ambient seismic noise. *Geophysical Research Letters*, 32(3):1–5.

Sabra, K. G., Gerstoft, P., Roux, P., Kuperman, W. A., and Fehler, M. C. (2005b). Surface wave tomography from microseisms in Southern California. *Geophysical Research Letters*, 32(14):1–4.

Sánchez-Sesma, F. J. and Campillo, M. (2006). Retrieval of the Green's function from cross correlation: The canonical elastic problem. *Bulletin of the Seismological Society of America*, 96(3):1182–1191.

Sens-Schönfelder, C. (2008). Synchronizing seismic networks with ambient noise. *Geophysical Journal International*, 174(3):966–970.

Sens-Schönfelder, C. and Wegler, U. (2006). Passive image interferemetry and seasonal variations of seismic velocities at Merapi Volcano, Indonesia. *Geophysical Research Letters*, 33(21):L21302.

Shapiro, N. M. and Campillo, M. (2004). Emergence of broadband Rayleigh waves from correlations of the ambient seismic noise. *Geophysical Research Letters*, 31(7):n/a–n/a.

Shapiro, N. M., Campillo, M., Stehly, L., and Ritzwoller, M. H. (2005). High-resolution surface-wave tomography from ambient seismic noise. *Science (New York, N.Y.)*, 307(5715):1615–8.

Shapiro, N. M., Ritzwoller, M. H., and Bensen, G. D. (2006). Surce location of the 26 sec microseism from cross-correlations of ambient seismic noise. *Geophysical Research Letters*, 33(18):n/a–n/a.

Snieder, R. (2004). Extracting the Green's function from the correlation of coda waves: A derivation based on stationary phase. *Physical Review E - Statistical Physics, Plasmas, Fluids, and Related Interdisciplinary Topics*, 69(4):8.

Stehly, L., Campillo, M., and Shapiro, N. M. (2006). A study of the seismic noise from its long-range correlation properties. *Journal of Geophysical Research: Solid Earth*, 111(10):B10306.

Stehly, L., Campillo, M., and Shapiro, N. M. (2007). Traveltime measurements from noise correlation: Stability and detection of instrumental time-shifts. *Geophysical Journal International*, 171(1):223–230.

Stein and Wysession, . (2003). *STEIN, S. WYSESSION, M. 2003. An Introduction to Seismology, Earthquakes, and Earth Structure.*, volume 140.

Thybo, H., Balling, N., Maupin, V., Ritter, J., and Tilmann, F. (2012). ScanArray Core (1G 2012-2017).

Tibuleac, I. M. and von Seggern, D. (2012). Crust-mantle boundary reflectors in Nevada from ambient seismic noise autocorrelations. *Geophysical Journal International*, 189(1):493–500.

Verbeke, J., Boschi, L., Stehly, L., Kissling, E., and Michelini, A. (2012). High-resolution Rayleigh-wave velocity maps of central Europe from a dense ambient-noise data set. *Geophysical Journal International*, 188(3):1173–1187.

Wapenaar, K. (2004). Retrieving the elastodynamic Green's function of an arbitrary inhomogeneous medium by cross correlation. *Physical Review Letters*, 93(25):254301.

Wapenaar, K., Draganov, D., Snieder, R., Campman, X., and Verdel, A. (2010). Tutorial on seismic interferometry: Part 1 — Basic principles and applications. *GEOPHYSICS*, 75(5):75A195–75A209.

Weaver, R. L. and Lobkis, O. I. (2004). Diffuse fields in open systems and the emergence of the Green's function (L). *The Journal of the Acoustical Society of America*, 116(5):2731–2734.

Wegler, U., Nakahara, H., Sens-Schönfelder, C., Korn, M., and Shiomi, K. (2009). Sudden drop of seismic velocity after the 2004 Mw6.6 mid-Niigata earthquake, Japan, observed with Passive Image Interferometry B06305. *Journal of Geophysical Research: Solid Earth*, 114(6):B06305.

Wegler, U. and Sens-Schönfelder, C. (2007). Fault zone monitoring with passive image interferometry. *Geophysical Journal International*, 168(3):1029–1033.

Weidle, C., Maupin, V., Ritter, J., Kvaerna, T., Schweitzer, J., Balling, N., Thybo, H., Faleide, J. I., and Wenzel, F. (2010). MAGNUS–A Seismological Broadband Experiment to Resolve Crustal and Upper Mantle Structure beneath the Southern Scandes Mountains in Norway. *Seismological Research Letters*, 81(1):76–84.

Yang, Y., Ritzwoller, M. H., Levshin, A. L., and Shapiro, N. M. (2007). Ambient noise Rayleigh wave tomography across Europe. *Geophysical Journal International*, 168(1):259–274.

Yao, H., Beghein, C., and Van Der Hilst, R. D. (2008). Surface wave array tomography in SE Tibet from ambient seismic noise and two-station analysis - II. Crustal and upper-mantle structure. *Geophysical Journal International*, 173(1):205–219.

Zhan, Z., Ni, S., Helmberger, D. V., and Clayton, R. W. (2010). Retrieval of Moho-reflected shear wave arrivals from ambient seismic noise. *Geophysical Journal International*, 182(1):408–420.

Zheng, S., Sun, X., Song, X., Yang, Y., and Ritzwoller, M. H. (2008). Surface wave tomography of China from ambient seismic noise correlation. *Geochemistry, Geophysics, Geosystems*, 9(5):n/a–n/a.

Appendices

Appendix A

Source code

Contents

Load stationdata and set station pair combinations

```
% Station name, first and last date and location [lat long]:
statN=['N2AN ';'N2BR ';'N2DI ';'N2HA ';'N2HS ';'N2IH ';'N2LO ';'N2NF ';...
    'N2RO ';'N2SO ';'N2ST ';'N2SV ';'N2TV ';'N2VA ';'N2VG ';'N2VI ';'NBB03';...
    'NBB05';'NBB08';'NBB12';'NBB13';'NBB14';'NBB15';'NBB17';'NBB28';'NBB29';'NBB30';'NBB
40'];
statDf={'19.08.2013','21.08.2013','22.11.2013','20.11.2013','23.10.2013',...
    '23.10.2013','19.08.2013','24.10.2013','01.11.2013','23.08.2013','22.10.2013',...
    '21.11.2013','25.10.2013','29.10.2013','27.04.2015','21.11.2013','13.03.2014',...
    '12.03.2014','11.03.2014','01.10.2013','03.10.2013','02.03.2013','04.10.2013',...
    '04.10.2013','12.03.2014','13.03.2014','14.03.2014','15.06.2014'};
statDl={'19.05.2016','21.05.2016','21.05.2016','20.05.2016','19.05.2016',...
    '09.01.2016','20.05.2016','19.05.2016','19.05.2016','20.05.2016','18.05.2016',...
    '21.05.2016','19.05.2016','28.03.2016','21.05.2016','21.05.2016','11.05.2016',...
    '10.05.2016','11.05.2016','14.06.2014','09.05.2016','08.05.2016','09.05.2016',...
    '09.05.2016','09.05.2016','29.02.2016','10.05.2016','08.05.2016'};
statL=[69.2371 16.0353; 68.5788 14.7075; 68.3134 14.9863; 68.7839 16.5611; ..
    68.1033 15.5136; 67.9662 15.9367; 68.4004 15.9533; 67.7610 15.2277; ...
    67.5173 12.1158; 68.7139 15.4380; 67.3487 15.5959; 67.8914 13.0098; ...
    67.5675 15.1252; 67.6639 12.6935; 66.7090 13.2690; 68.3212 14.1976; ...
    67.1031 14.9681; 67.0368 14.0306; 67.3871 14.6364; 66.3870 13.1199; ...
    66.6275 13.3272; 66.3030 13.5586; 66.7435 13.5776; 66.8161 13.9581; ...
    67.1909 14.4622; 66.9919 15.3292; 66.9732 13.7354; 66.5130 13.0097];

statcell=cellstr(statN);
nost=length(statN);
statnum=1:nost;

% Connect the names, dates and coordinates
for i=1:nost
    stations(i)=struct('station',statN(i,:),'first_day',statDf(i),...
        'last_day',statDl(i),'location',statL(i,:));
end

% Rearrange the order of the stations:
statcomb=[3,2,10,1,8,5,7,4,17,11,19,6,9,14,12,16,23,25,11,13,20,22,24,26,28,27,17,21]; %
 2try
nost=length(statcomb);
for j=1:nost
    statR(j)=stations(statcomb(j));
end

% Every station is cross correlated with at least 3 other stations
j=0;
for i=1:4:nost
    statp(i,:)=[j+2;j+3;j+4];
    statp(i+1,:)=[j+3;j+4; 0];
    statp(i+2,:)=[j+4;0;0];
```

```
    statp(i+3,:)=[0;0;0];
    j=j+4;
end

% Filter values
bpf=[0.01 1.25]; % bandpass filter
Fq=10; % Hz
tspd=(Fq*60*60*24); L=tspd; % total number of seconds
% Pre-processing filter:
df1= designfilt('bandpassiir','FilterOrder',4, ...
    'HalfPowerFrequency1',bpf(1),'HalfPowerFrequency2',bpf(2), ...
    'SampleRate',Fq,'DesignMethod','butter');
fvtool(df1)
legend(['Bandpass ' num2str(bpf(1)) '-' num2str(bpf(2)) ''])

% Filter for measuring time delays
df3= designfilt('bandpassiir','FilterOrder',4, ...
                    'HalfPowerFrequency1',1/7,'HalfPowerFrequency2',0.5, ...
                    'SampleRate',Fq,'DesignMethod','butter');

% Divide into segments:
wll=6;
nwll=wll*60*60*10;
for i=1:(24/wll)
    fpp(i)=(nwll*(i-1))+1;
    lpp(i)=(nwll*i);
end
```

Calculate Green's function and measure time delay

Loop over all the stations:

```
nsp=nost*2-(nost/2); % Number of station pairs
sp=0; % Stationpair

timedelay=zeros(nsp,1010);
iterations=3;
for i=1:nost
    As=char(cellstr(statR(i).station));
    stationA=load([As '_Z.mat']);
    pz_file_A=[As '-Z.pz'];
    statA1=stationA.station.channel.days;

    fda=datetime(statR(i).first_day,'InputFormat','dd.MM.yyyy');
    lda=datetime(statR(i).last_day,'InputFormat','dd.MM.yyyy');
    for ll=1:3
        numst=statp(i,ll);
        if numst>0
            sp=sp+1;

            Bs=char(cellstr(statR(numst).station));
            stationB=load([Bs '_Z.mat']);
            pz_file_B=[Bs '-Z.pz'];
            statB1=stationB.station.channel.days;

            % Make sure the stations are correlated over the same dates
            fdb=datetime(statR(numst).first_day,'InputFormat','dd.MM.yyyy');
            ldb=datetime(statR(numst).last_day,'InputFormat','dd.MM.yyyy');
            dF=caldays(between(fda,fdb,'Days'));
```

```
            dL=caldays(between(lda,ldb,'Days'));

            if dF>=0 && dL<=0
                % Station A starts before, but ends afterB
                statA=statA1(1+dF:end+dL);
                statB=statB1;
            elseif dF>=0 && dL>=0
                % Station A both starts and ends before B
                statA=statA1(1+dF:end);
                statB=statB1(1:end-dL);
            elseif dF<=0 && dL>=0
                % Station B starts before, but ends after A
                statA=statA1;
                statB=statB1(1-dF:end-dL);
            elseif dF<=0 && dL<=0
                % Station B both starts and ends before A
                statA=statA1(1:end+dL);
                statB=statB1(1-dF:end);
            end

            num_days=length(statA);
            L=length(statA(1).data);

            crconvw0=[];
            crconvf=[];
            faulty=[];
            % Loop over the days
            for d=1:num_days
                % Extract data of each station:
                SAdata=(statA(d).data)';
                SBdata=(statB(d).data)';

                % Remove mean and trend:
                SAdtrnd=detrend(SAdata);
                SBdtrnd=detrend(SBdata);

                % Taper:
                SAtap=costap_filter(SAdtrnd,0.05);
                SBtap=costap_filter(SBdtrnd,0.05);

                % Bandpass filter
                SAfilt1=filtfilt(df1,SAtap);
                SBfilt1=filtfilt(df1,SBtap);

                % Remove instrument response
                SAtrans=transfer(SAfilt1,L,Fq,pz_file_A);
                SBtrans=transfer(SBfilt1,L,Fq,pz_file_B);

                % Bandpass filter
                SAfilt2=filtfilt(df1,SAtrans);
                SBfilt2=filtfilt(df1,SBtrans);

                % Onebit normalize
                SAonebit=SAfilt2./abs(SAfilt2);
                SBonebit=SBfilt2./abs(SBfilt2);

                % Whitening
                SAwhite=mywhitening(SAonebit,Fq);
                SBwhite=mywhitening(SBonebit,Fq);

                % Cross correlate over smaller time windows to save time:
```

```
                for hh=1:length(fpp)
                    SAseg=SAwhite(1,fpp(hh):lpp(hh));
                    SBseg=SBwhite(1,fpp(hh):lpp(hh));

                    % Cross correlation:
                    [crconvwseg(hh,:) lag]=Cross_conv(SAseg,SBseg); % Using my flip and
conv:
                end
                crconvw0(d,:)=sum(crconvwseg);

                % If the mean of the cross correlation is NaN:
                if isnan(mean(crconvw0(d,:)))==1
                    crconvw0(d,:)=zeros(1,length(crconvw0(d,:)));
                    faulty=[faulty d];
                end
            end
            crosscorrs=struct('crconvw',crconvw0,'lag',lag);
            save([As '_' Bs '_' num2str(bpf(1)) '_' num2str(bpf(2)) '_days.mat'],'crossc
orrs','-v7.3')

            % I only use +-2000 lag to reduce computional effort
            zerolag=find(lag==0);
            crconvw=crconvw0(:,zerolag-2000:zerolag+2000);
            cl=lag(zerolag-2000:zerolag+2000);

            % Stack and filter
            stack_totw=sum(crconvw);
            stack_totf=filtfilt(df3,stack_totw);

            % Normalize the stacked
            stack_totnw(sp,:)=stack_totw/max(abs(stack_totw));
            stack_totfn=stack_totf/max(abs(stack_totf));

            % Calculate timing differnce
            delay_neg=[];
            delay_pos=[];
            delay_dyn=[];
            maxtdn=[];
            maxtdp=[];

            yearshift=stack_totf;

            Lc=length(cl);
            % Separate the time lags:
            zero_lag=find(cl==0);

            for it=1:iterations
                % Separte the negative and positive side of the signal:
                r_neg1=flip(yearshift(it,1:zero_lag));
                r_pos1=yearshift(it,zero_lag:end);
                % Normalize
                r_neg=r_neg1/max(abs(r_neg1));
                r_pos=r_pos1/max(abs(r_pos1));

                for j=1:num_days
                    crconvf(j,:)=filtfilt(df3,crconvw(j,:));

                    % Daily trace
                    s_neg1=flip(crconvf(j,1:zero_lag));
                    s_pos1=crconvf(j,zero_lag:end);
                    % Normalize
```

```
                    s_neg=s_neg1/max(abs(s_neg1));
                    s_pos=s_pos1/max(abs(s_pos1));

                    % Compare the daily traces with the refernce trace:
                    [td_neg1 lag_neg]=Cross_conv(r_neg,s_neg);
                    [td_pos1 lag_pos]=Cross_conv(r_pos,s_pos);

                    % Normalize the correlations using the autocorrelations:
                    [au_nr alag_n]=Cross_conv(r_neg,r_neg);
                    [au_pr alag_p]=Cross_conv(r_pos,r_pos);
                    [au_ns alag_n]=Cross_conv(s_neg,s_neg);
                    [au_ps alag_p]=Cross_conv(s_pos,s_pos);

                    td_neg=td_neg1/max(abs(sqrt(au_nr.*au_ns)));
                    td_pos=td_pos1/max(abs(sqrt(au_pr.*au_ps)));

                    % Find the correlation coeffisient
                    maxtdn(j)=max(td_neg);
                    maxtdp(j)=max(td_pos);

                    if maxtdn(j)>0.4 && maxtdp(j)>0.4
                        % Only use cross correlations with coeffisient above 0.4 to find
 the delay

                        delay_neg(j)=lag_neg(find(td_neg==max(td_neg)));
                        delay_pos(j)=lag_pos(find(td_pos==max(td_pos)));

                        if (-(delay_neg(j)+2))<=delay_pos(j) && delay_pos(j)<=(-(delay_n
eg(j)-2))

                            % Only use the shifts that occur at both sides with opposite
 sign

                            delay_dyn(j)=(delay_pos(j)-delay_neg(j))/2;
                        else
                            delay_neg(j)=0;
                            delay_pos(j)=0;

                            delay_dyn(j)=0;
                        end
                    else
                        delay_neg(j)=0;
                        delay_pos(j)=0;

                        delay_dyn(j)=0;
                    end
                end
                % Correct for found timing errors
                dayshift=zeros(num_days,Lc);
                for d=1:num_days
                    day1=crconvf(d,:);
                    if delay_dyn(d)==0
                        dayshift(d,:)=day1;
                    else
                        t01=-(delay_dyn(d)/10);
                        omgc=exp([0:Lc-1]*Fq/Lc*-1i*2*pi*t01);
                        shift1=fft(day1).*omgc;
                        shift2=ifft(shift1,'symmetric');
                        dayshift(d,:)=shift2;
                    end
                end
                yearshift(it+1,:)=sum(dayshift);
            end
```

```
            % Save the found time delays
            timedelay(sp,1:num_days)=delay_dyn(1,1:num_days);
            pair(sp,:)=[char(statR(i).station) '-' char(statR(numst).station)]
            stationpair=struct('stationpair',pair(sp,:),'stack_totw',stack_totw,'time_de
lay',delay_dyn,'maxtdp',maxtdp,'maxtdn',maxtdn,'faulty',faulty,'distance',d1km(sp));
            save(['/home/karina/Matlab_files/Cross_correlation/' As '_' Bs '_filt_' num2
str(bpf(1)) '_' num2str(bpf(2)) '_ref_10d.mat'],'stationpair')
        end
    end
end
```

Plot the noise correlations and invert to find the time delay of each station

Matrix for inversion

```
G=zeros(6,4);
G(1,1)=1; G(1,2)=-1;
G(2,1)=1; G(2,3)=-1;
G(3,1)=1; G(3,4)=-1;
G(4,2)=1; G(4,3)=-1;
G(5,2)=1; G(5,4)=-1;
G(6,3)=1; G(6,4)=-1;

lagd=[lag/10:0.1:lag/10]; % I divide lag with 10 to plot the correlations in s
sp=0; % stationpair number
ii=0; % station number
ww=0; % Station number after inversion
for rr=1:nost/4
    ki=0; % Staionpair number in this group
    pp0=1; % Subplot number
    figure
    for kk=1:4
        ii=ii+1;
        for jj=1:3
            numst=statp(ii,jj);
            if numst>0
                ki=ki+1;
                sp=sp+1;

                maxy=max(time_delay(sp,:)/10)+1; % Find maximum timde delay for plotting

                subplot(6,2,pp0)
                plot(lagd,stack_totnw(sp,:))
                title(['Stacked Cross correlation of ' pair(sp,:)],'FontSize', 12)
                axis([-50 50 -1 1])
                xlabel('Time (s)','FontSize', 10)
                subplot(6,2,pp0+1)
                plot(time_delay(sp,1:num_days(sp))/10)
                axis([1 num_days(sp) -maxy maxy])
                title(['Relative timedelay for ' pair(sp,:)],'FontSize', 12)
                xlabel('days','FontSize', 10), ylabel('Delay (s)','FontSize', 6)
                %datetick('x','mm.yyyy','keeplimits')
                hold on

                pp0=pp0+2;

                timedelay(ki,:)=time_delay(sp,:);
            end
        end
```

```
    end
    hold off

    % Invert to find time delay of each station
    m=pinv(G)*timedelay;

    % Set the most realiable station to zero:
for i=1:length(m(:,1))
    sum_m(i,:)=sum(abs(m(i,:)));
end

realm=find(sum_m==min(sum_m))

for i=1:length(m(:,1))
    mc(i,:)=m(i,:)-(m(realm,:));
end

    figure
    for ff=1:4
        ww=ww+1;

        subplot(4,1,ff)
        plot(mc(ff,:)/10,'')
        axis([0 num_days(sp) -1 1])
        title(['Time delays for ' char(cellstr(statR(ww).station)) ' between ' char(fd(s
p)) '-' char(ld(sp))],'FontSize', 14)
        xlabel('Days','FontSize', 10), ylabel('Time delay (s)','FontSize', 10)
        hold on
    end
end
hold off
```

Calculate distance and azimuth

```
rad=6371; % km
sp=0;
for kk=1:nost
    for jj=1:3
        numst=statp(kk,jj);
        if numst>0
            sp=sp+1;

            % Station pair coordinates
            lati1(sp)=statR(kk).location(1);
            long1(sp)=statR(kk).location(2);
            lati2(sp)=statR(numst).location(1);
            long2(sp)=statR(numst).location(2);

            % Calculate distance and azimuth:
            delta=acosd(cosd(90-lati1(sp))*cosd(90-lati2(sp))+sind(90-lati1(sp))*sind(90
-lati2(sp))*cosd(long2(sp)-long1(sp)))
            dist=rad*delta;
            az(sp)=asind((1/sind(delta))*sind(90-lati2(sp))*sind(long2(sp)-long1(sp)));

            % Calculate the ratio of the causal and acausal signal:
            ratio(sp)=log10(max(abs(stationpair(sp,zero_lag:end)))/max(abs(stationpair(s
p,1:zero_lag))));

        end
    end
```

```
end

% PLot azimth as colorcoded lines
im=imread('map_for_matlab.JPG');

M=size(im,1);
N=size(im,2);
xx=linspace(10,18.02,N);
yy=linspace(66,70.15,M);
xxx=linspace(10,18,sp);
yyy=linspace(66,70,sp);

figure
plot(xxx,yyy,'w')
hold on
image(xx,yy,flip(im))
hold on
view(2);   % Default 2-D view
for i=1:sp
    surf([long1(i) long2(i); long1(i) long2(i)], [lati1(i) lati2(i); lati1(i) lati2(i)],
 [ratio(i) ratio(i); ratio(i) ratio(i)], ...
         'FaceColor', 'none', ...
         'EdgeColor', 'flat', ...
         'LineWidth', 2);
     hold on
end
view(2);   % Default 2-D view
colorbar
title('Azimuth of noise')
xlabel('Longitude ¤'), ylabel('Latitude ¤')
axis([10 18 66 70])
caxis([-0.9 0.9])
hold off
```

Functions:

```
function xnew = mywhitening(x,Fs)
    %   Spectral whitening

    % Magnitude vector
    xf=fft(x);
    mag=abs(xf);

    % Running average filter
    b=(1/3)*ones(1,3);
    magm=filtfilt(b,1,mag);

    % Water level
    prosent=0.1;
    alfa=prosent*(max(magm))/100;

    xfnew=xf./(alfa+magm);
    xnew = ifft(xfnew,L,'symmetric');
end

function [cross lag]=Cross_conv(seq1,seq2)
  % Cross correlation function using flip and conv
  m=length(seq1);
  n=length(seq2);
  k=max(m,n);
```

```
  for i=1:(m+n)-1
     % I make the lag vector start from negative and have the length
     % 2*max(m,n)-1:
     lag(i)=-k+i;
  end

  s1=flip(seq1);
  s2=seq2;

  cross=conv(s1,s2);
end

function seis_tap=costap_filter(seis,perc)
% Costapfunction
m=length(seis); % length of the seismogram

tap=round(perc*m); % I taper off perc % of the signal

theta=linspace(0,pi,tap);

% The first part of the costap(t) function:
costap1=0.5*(-cos(theta)+1);

% The middle part of the costap(t) function:
costap2=ones(1,m-2*tap);

% The last part of the costap(t) function:
costap3=0.5*(cos(theta)+1);

costap=[costap1 costap2 costap3];

seis_tap=seis.*costap;

end
```

Published with MATLAB® R2018b